

A NOVEL INDOOR POSITIONING SYSTEM BASED ON GPS  
REPEATERS IN 433 MHZ ISM BAND

by

ABDULKADİR UZUN

Submitted to the Graduate School of Engineering and Natural Sciences

in partial fulfillment of the requirements

for the degree of

Master of Science

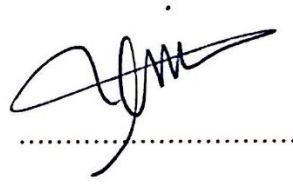
SABANCI UNIVERSITY

AUGUST 2020

A NOVEL INDOOR POSITIONING SYSTEM BASED ON GPS REPEATERS IN  
433 MHZ ISM BAND

APPROVED BY:

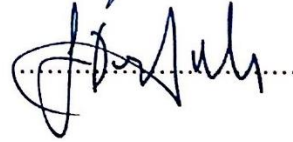
Prof. Ibrahim Tekin  
(Thesis Supervisor)



Assoc. Prof. Hüsni Yenigün



Asst. Prof. Sema Dumanlı Oktar



DATE OF APPROVAL:

..19/08/2020.....

© Abdulkadir Uzun - 2020

All Rights Reserved

## ABSTRACT

### A NOVEL INDOOR POSITIONING SYSTEM BASED ON GPS REPEATERS IN 433 MHZ ISM BAND

ABDULKADİR UZUN

M.Sc. Thesis, August 2020

Thesis Supervisor: Prof. İbrahim Tekin

**Keywords:** GPS, Indoor Positioning, RF Repeaters, Down-Conversion, Up-Conversion

Civil Global Positioning System (GPS) based indoor positioning has become a challenging subject owing to the restrictions on the use of GNSS repeaters. The indoor environment is another challenge for positioning due to signal loss from walls and building materials and multipath effect. For these reasons, indoor positioning is still a problem to be solved. A novel GPS repeater and receiver front end are proposed in this thesis to overcome signal coverage and restrictions on the use of GNSS repeaters. The GPS repeater and receiver front ends are designed, implemented, and tested in a real-life scenario. The designed indoor positioning system is based on down-conversion of GPS signals to 433 MHz ISM band on the repeaters. Repeaters amplify and retransmit the down-converted positioning signals indoors in that the allowable output power is increased and the restrictions on the use of GNSS repeaters are circumvented. The increased allowable output power and less path loss at 433 MHz solve the coverage problem extensively. The receiver front end amplifies the positioning signals at 433 MHz, up-converts back to GPS frequency and feeds to an off-the-shelf GPS receiver for decoding the positioning signals. The results of the experiments show that the proposed indoor positioning system may be used to provide indoor positioning by expanding the GPS coverage area indoors. This MSc. thesis is partly supported by The Scientific and Technological Research Council of Turkey (TÜBİTAK) under the grant agreement number 116E752.

## ÖZET

### 433 MHz ISM BANDINI KULLANAN GPS TEKRARLAYICI TEMELLİ KAPALI ALANDA KONUM BULMA SİSTEMİ

ABDULKADİR UZUN

Yüksek Lisans Tezi, Ağustos 2020

Tez Danışmanı: Prof. Dr. İbrahim Tekin

**Anahtar Kelimeler:** GPS, Kapalı Alanda Konumlandırma, RF Tekrarlayıcı, Frekans Aşağı Dönüştürme, Frekans Yukarı Dönüştürme

Sivil Küresel Konumlandırma Sistemi (GPS) tabanlı kapalı alanda konum bulma sistemi tasarımı, GNSS tekrarlayıcıların kullanımı üzerindeki kısıtlamalar nedeniyle ilgi çekici hale gelmiştir. Kapalı alanlarda duvar ve yapı materyalleri nedeniyle sinyal kayıpları ve çok yollu yansımalar meydana gelmesi nedeniyle konumlandırma zorlu bir problemdir. Bu çalışmada, kapalı alanda GPS kapsama probleminin ve GNSS tekrarlayıcıları üzerindeki kısıtlamaların üstesinden gelmek için yeni bir GPS tekrarlayıcı ve alıcı önkat devreleri tasarlanmış, modüller ile gerçekleştirilmiş ve kapalı alanda test edilmiştir. Önerilen sistem, GPS sinyallerinin frekansının, tekrarlayıcılarda 433 MHz ISM bandına düşürülmesine ve alıcı önkatında 1575.42 MHz GPS frekansına yeniden yukarı dönüştürülmesine dayanmaktadır. GPS tekrarlayıcıları, frekansı aşağı dönüştürülmüş GPS sinyallerinin gücünü yükseltip kapalı ortamda yaymaktadır. Alıcı önkatında ise, 433 MHz frekansındaki konumlandırma sinyalleri önce güçlendirilir sonra GPS frekansına dönüştürülerek hazır bir GPS alıcısına gönderilir. Frekans dönüştürme işlemleri sayesinde sistem, GNSS tekrarlayıcılar ile ilgili kısıtlamalardan bağımsız hale gelmiştir. Tekrarlayıcı çıkışlarındaki daha yüksek çıkış gücü sayesinde kapalı alandaki kapsama alanı problemi önlenmiş olur. Bu çalışmanın sonuçlarına göre önerilen sistem, GPS kapsama alanını artırarak kapalı alanlarda konumlandırma sağlayabilir. Bu tez çalışması Türkiye Bilimsel ve Teknolojik Araştırma Kurumu (TÜBİTAK) tarafından 116E752 hibe numarası altında desteklenmektedir.

*To those who walk with me, my friends, and my family*

## ACKNOWLEDGEMENTS

It is now time to write down some acknowledgments after 3 years of study full of happiness and excitement with the great support of my family, friends, and mentors. I wish to thank all those people from whom I had the strength to continue walking on this road. I am so blessed to have known these warm-hearted people who have contributed to me personally, and to this thesis, each in their own way.

Prof. İbrahim Tekin is the greatest mentor, advisor, and supervisor ever. It has been such an honor to be one of his students as he is always there whenever I need help with anything I come across in my life. He is never too busy to hear my ideas, problems, jokes, or questions. He always provided me with the best guidance I can wish for throughout my study, but most importantly, he did that by allowing me to have the freedom to search for my path. I cannot thank him enough for being so gentle, understanding, and kind to me in any subject in my academic and personal life. Without his efforts, encouragement, support, and guidance, this thesis would not exist.

I wish to thank Prof. Hüsnü Yenigün as he always has welcomed me with a great smile even if I have many problems in my study. He deserves my sincerest gratitude for helping me with this thesis study during the pandemic whenever I need any advice or help on the test setups. I can never forget how he helped me during the difficult times we had. He is the kind of person who is there if his students need him on anything.

I thank Prof. Ayhan Bozkurt for his kindness and having welcomed me whenever I dropped by his office with a new question. With his many contributions, this thesis has reached a conclusion. I would also like to thank Prof. Sema Dumanlı Oktar for taking the time to review my work, giving me useful feedback.

Our lab group has always provided me with many different ways. When I was not able to enter the lab, they helped me to continue my work and helped this thesis to be completed. My dear friend Firas has always taken his time to solve some of the problems I have to face. Without his contribution, this thesis would not be possible. I thank him for being so gentle and helpful through these years we spent together in the lab. I also thank Doruk for

his contributions to this thesis. Kerem Özsoy, a former member of our lab group, and his company Antsis Elektronik have given me many opportunities. They provided me an office and many kind friends to work together. They have answered all my questions with patience and kindness. I cannot thank enough to Kerem Özsoy and his team in Antsis Elektronik. I did not work in the lab with only our group members, but also with our laboratory specialists Ali Kasal and Sercan Tanyeli. I thank Ali “Abi” and Sercan for being more than people in the lab. They have been really good friends and my problem solvers. They have never left my questions without any answer. I like our quick talks in FENS corridors with a cup of coffee. I am so happy to have worked with all these amazing people! I am sure of one thing: I will never forget how I like working among them.

My loving mother, Ayşe, has always tried hard to support my passion in my education life and always put my education first. I know I cannot thank her in these lines as it would not be sufficient. She endured my absence, laziness, crankiness, and never asked me to be different than who I am. She has made all my dreams come true. I love her so much! She is a hero to me with her courage, honor, and love. My loving father has worked hard to create the opportunities that I have considered as priveledges in my life. He has never rejected my requests and tried his best to be a good and gentle father. I appreciate him. I cannot be who I am today without my dear mother and father. I am proud of being their son.

As once said, a family is not only formed with blood-linked people. People I list here are the ones who are always by my side, and without whom I am incomplete. They are the ones who made my life worthy. They are my “adopted family” as Ebru called in her thesis’ acknowledgments. I, hereby, thank my first friend with a PhD: Ebru Demir. She has been more than a friend to me. She is the sister I have never had. I cannot express how I like her, our talks, her love for tea, her keyboard skills, amazing talent in catching up with the deadlines, and many other things I cannot fit into any sentence. I am happy to know that no distance can separate us. My adopted family continues with the next family member: Şahin. I thank him for being such a good companion on this journey. He is one of the most supportive and caring person that I have ever known. I cannot imagine how life would be without his encouragement. My family gets larger with these girls:

Yağmur, Belen, and Melisa. It has been much more than 12 years since we know each other. They are my childhood, my youth, and my today. They have provided me a place to run away when I feel tired: Ankara. I thank them for being so understanding for more than 12 years.

All the people I listed in this part should always know one thing: we have to be together forever! I cannot think how I can complete this work without them. Moreover, I cannot imagine how incomplete I would be without them.

Lastly, I thank TÜBİTAK as this MSc. thesis is partly supported by The Scientific and Technological Research Council of Turkey (TÜBİTAK) under the grant agreement number 116E752.

## TABLE OF CONTENTS

Chapter 1 Introduction .....	1
1.1 Literature Review .....	4
1.2 Motivation .....	16
Chapter 2 GPS Overview .....	19
2.1 GPS Segments .....	20
2.1.1 Space Segment .....	20
2.1.2 Control Segment .....	21
2.1.3 User Segment .....	22
2.2 Principles of Operation .....	22
2.3 GPS Based Indoor Positioning .....	26
Chapter 3 Repeater Hardware of the Indoor Positioning System .....	30
3.1 Directional Outdoor GPS Antenna .....	34
3.1.1 Directional Antenna Design .....	35
3.1.2 Directional Antenna Measurement Results .....	39
3.2 Down-converter .....	41
3.2.1 Down-converter Modules and Design .....	42
3.2.2 Down-Converter Optimization, Simulations and Measurements .....	44
3.2.3 Down-Converter Measurement Results .....	55
3.3 Signal Power Conditioner and Filter .....	57
3.3.1 Signal Power Conditioner and Filter Design .....	60
3.3.2 Signal Power Conditioner S-Parameter Measurements and Results .....	61
3.4 433 MHz Directional Indoor Antenna .....	68
3.4.1 433 MHz Directional Indoor Antenna Design .....	69
3.4.2 433 MHz Directional Indoor Antenna Measurement Results .....	76
3.5 Voltage Regulator for Repeater Hardware .....	81
3.6 Programmer and Controller over the Wi-Fi .....	83
Chapter 4 Receiver Hardware of the Indoor Positioning System .....	85
4.1 433 MHz Receiver Antenna .....	89
4.2 Signal Power Conditioner and Filter .....	91

4.2.1 Signal Power Conditioner and Filter Design and S-Parameter Measurement .....	93
4.3 Up-converter.....	95
4.3.1 Up-Converter Modules and Design .....	96
4.3.2 Up-Converter Optimizations.....	100
4.3.3 Up-Converter Measurement Results.....	105
4.4 Off-the-shelf GPS Receiver .....	108
4.5 Voltage Regulator for Receiver Hardware.....	109
4.6 Programmer and Controller over Wi-Fi.....	111
4.6.1 Programmer and Controller Design and Fabrication .....	111
4.6.2 Programmer and Controller Block Tests .....	115
Chapter 5 Measurement of Indoor Positioning System .....	119
5.1 End-to-end loss measurements in Repeater and Receiver Boards .....	120
5.2 Evaluating the Effect of Down and Up-Conversion Method on GPS Signals.....	128
5.3 1D Positioning.....	132
5.3.1 1D Positioning Algorithm.....	132
5.3.2 1D Positioning Test Setup .....	137
5.3.3 1D Positioning Test Results.....	139
Chapter 6 Conclusion and Future Work .....	148
APPENDIX A.....	151
APPENDIX B .....	156
APPENDIX C .....	160
REFERENCES .....	162

## LIST OF FIGURES

Figure 1.1 The proposed three-repeater system for 2D indoor positioning.....	1
Figure 2.1 GPS Segments .....	20
Figure 2.2 GPS Satellite Constellation [68].....	21
Figure 2.3 Basic principle of GPS positioning .....	24
Figure 2.4 GPS Errors [72] .....	25
Figure 2.5 Overview of 2D Indoor Positioning Based on GPS .....	27
Figure 3.1 Repeater hardware and its building blocks.....	31
Figure 3.2 Repeater hardware excluding the 433 MHz directional antenna .....	34
Figure 3.3 Antenna design in HFSS .....	36
Figure 3.4 Total directivity with and without the conic reflector .....	36
Figure 3.5 2D Polar gain and total realized gain plots with and without the conic reflector .....	37
Figure 3.6 Active GPS antenna.....	38
Figure 3.7 Active antenna on the large ground plane .....	38
Figure 3.8 Directional outdoor GPS active antenna .....	38
Figure 3.9 Directional antenna and the semi-anechoic chamber .....	39
Figure 3.10 Measured 2D Patterns with and without the reflector, and the original antenna .....	40
Figure 3.11 Modules in the down-converter block.....	42
Figure 3.12 Modules used in the down-converter block .....	43
Figure 3.13 Down-converter block formed with the modules presented .....	44
Figure 3.14 L-section matching network and 1:1 transformers.....	46
Figure 3.15 L-section matching and ADS S-parameter Simulation .....	46
Figure 3.16 Insertion Loss of L-section matching network.....	47
Figure 3.17 ADRF6820-EVALZ loss measurement setup.....	47
Figure 3.18 Power level at the outputs of I+ and Q+ channels, respectively in (a) and (b) .....	48
Figure 3.19 Power level at the output of the 90-degree hybrid combiner .....	48

Figure 3.20 Measurement setup in (a) and the modified ADRF6820 combined with the 90-degree power combiner in (b).....	49
Figure 3.21 Signal power at the output for the fully modified ADRF6820-EVALZ combined with the 90-degree power combiner.....	49
Figure 3.22 ADRF6820 Customer Evaluation Software Interface and The Optimized Values .....	51
Figure 3.23 Q channel leading I channel by 90 degrees if $f_{LO} > f_{GPS}$ [83] .....	52
Figure 3.24 Suggested BAL_CIN, BAL_COUT, MIX_BIAS, DEMOD_RDAC, and DEMOD_CDAC values emphasized in red rectangle.....	53
Figure 3.25 Gain vs Frequency of RF signal at the input of ADRF6820 for several BAL_CIN and BAL_COUT codes [83] .....	53
Figure 3.26 Setting ILO and QLO and for improved image rejection [83].....	54
Figure 3.27 The power level of the signal formed at the frequency of 433 MHz and 3583.84, respectively in (a) and (b) .....	54
Figure 3.28 Signal levels at the output of I+ in (a) and Q+ in (b) after optimizations ..	56
Figure 3.29 Signal level at the output of down-converter block after optimizations .....	56
Figure 3.30 Modules in the signal power conditioner and filter block.....	58
Figure 3.31 Realized signal power conditioner and filter block.....	59
Figure 3.32 Modules in signal power conditioner and filter block.....	60
Figure 3.33 (a) Reflection coefficient of the input port (S11) and output port (S22), (b) Gain (S21) Measurement Results .....	62
Figure 3.34 BPF as module.....	63
Figure 3.35 (a) Reflection coefficient of the input port (S11) and output port (S22), (b) Insertion loss (S12) measurement results .....	63
Figure 3.36 Cascaded LNA, BPF, and LNA .....	64
Figure 3.37 S11 and S22 of Cascaded LNA, BPF, and LNA in (a) and S21 of the overall cascaded topology in (b) .....	65
Figure 3.38 Cascaded LNA, BPF, Attenuator and LNA .....	66
Figure 3.39 S11 and S22 of Cascaded LNA, Attenuator, BPF, and LNA in (a) and S21 of the overall cascaded topology in (b) .....	67
Figure 3.40 Designed 433 MHz Patch Antenna 1 with the optimized dimensions .....	70

Figure 3.41 S11 simulation result for 433 MHz patch antenna 1 .....	71
Figure 3.42 Realized gain (a) and radiation pattern (b) simulation results for 433 MHz patch antenna 1 .....	71
Figure 3.43 Designed 433 MHz Patch Antenna 2 with optimized dimensions and via locations .....	72
Figure 3.44 S11 simulation result for 433 MHz patch antenna 2 .....	73
Figure 3.45 Realized gain (a) and radiation pattern (b) simulation results for 433 MHz patch antenna 2 .....	73
Figure 3.46 Designed 433 MHz Patch Antenna 3 with optimized dimensions and short-circuit layer .....	74
Figure 3.47 S11 simulation result for 433 MHz patch antenna 3 .....	75
Figure 3.48 Realized gain (a) and radiation pattern (b) simulation results for 433 MHz patch antenna 3 .....	75
Figure 3.49 50-ohm SMA connector for pin-fed antennas and 3D printed spacers, in (a) and (b), respectively .....	77
Figure 3.50 Antenna top, bottom, side, and cross-sectional views in (a), (b), (c)-(d), respectively .....	78
Figure 3.51 Antenna 1 with the dimensions determined in simulations .....	78
Figure 3.52 Antenna 1 with the copper tape to improve S11 at 433 MHz value by extending the width of the antenna .....	79
Figure 3.53 Fabricated patch antenna 3 .....	80
Figure 3.54 Simulated and Measured reflection coefficient for patch antenna 3 .....	80
Figure 3.55 Voltage regulator for repeater hardware .....	82
Figure 4.1 Receiver Hardware and Its Building Blocks .....	86
Figure 4.2 Repeater hardware excluding the 433 MHz directional antenna .....	89
Figure 4.3 433 MHz receiver antenna .....	90
Figure 4.4 Modules in the signal power conditioner and filter block .....	91
Figure 4.5 Realized signal power conditioner and filter block .....	92
Figure 4.6 Cascaded BPF, LNA, attenuator, and LNA .....	93
Figure 4.7 (a) Reflection coefficient of the input port (S11) and output port (S22), (b) Gain (S21) Measurement Results .....	94

Figure 4.8 Modules in the up-converter block.....	95
Figure 4.9 Modules used in the up-converter block .....	97
Figure 4.10 Up-converter block formed with the modules presented .....	98
Figure 4.11 Layout in Altium (a), EM (b) & post-layout (b) simulations of bias tee in AWR .....	99
Figure 4.12 Post Layout Simulation Results for S-parameters.....	99
Figure 4.13 ADRF6720-27 customer evaluation software interface and the optimized values .....	101
Figure 4.14 Output signal level at 1575.42 MHz and 2441.42 MHz, respectively, in (a) and (b).....	103
Figure 4.15 DCOFFI and DCOFFQ settings for carrier feedthrough nulling .....	103
Figure 4.16 Optimum balun setting for the desired frequency of 1575.42 MHz is highlighted in red rectangle .....	104
Figure 4.17 I_LO and Q_LO setting for sideband suppression [84] .....	104
Figure 4.18 Phase difference between input and quadrature outputs on I/Q power divider board .....	106
Figure 4.19 Magnitude of S-parameters from input to each quadrature outputs on I/Q power divider .....	106
Figure 4.20 Complete up-converter block with I/Q power combiner, bias tees and ADRF6720-27 from left to right.....	107
Figure 4.21 Signal power measured at the output of the up-converter block when the input signal is -21.1 dBm .....	108
Figure 4.22 EVK-M8T evaluation kit and u-Center 8.29 interface.....	109
Figure 4.23 Voltage regulator for receiver hardware .....	110
Figure 4.24 Architecture of the programmer and controller block.....	112
Figure 4.25 Experimental setup of Programmer and Controller Block.....	112
Figure 4.26 The schematic design of the programmer and controller block .....	113
Figure 4.27 The layout of the programmer and controller block.....	114
Figure 4.28 Fabricated programmer and control block .....	114
Figure 4.29 USB-ADRF6820 communication viewed by a logic analyzer .....	116

Figure 4.30 Register sets for the optimized settings are read from ADRF6820 after programming with realized programmer and controller block.....	117
Figure 4.31 Testing written software code on the attenuator .....	118
Figure 4.32 (a) Measurement with 0 dB attenuation and (b) Measurement with 8 dB attenuation after setting with programmer and controller block.....	118
Figure 5.1 Signal power levels between modules of the repeater .....	121
Figure 5.2 Signal power levels between modules of the receiver .....	123
Figure 5.3 End-to-end power measurement of GPS signals in the designed system....	125
Figure 5.4 One of the repeaters and the receiver hardware for indoor positioning system based on down and up-conversion of GPS signals .....	126
Figure 5.5 GPS signal supplied to the system input from the GPS signal generator....	127
Figure 5.6 Power of the down-converted GPS signal at the output of the repeater.....	127
Figure 5.7 Power of the GPS signal after up-conversion at the output of the receiver hardware.....	128
Figure 5.8 Performance of the proposed repeater and receiver hardwares along with the positioning algorithms on GPS signals.....	129
Figure 5.9 Distance of each sample to the average estimated position when the receiver and repeater hardware are inserted between the GPS signal generator and off-the-shelf receiver.....	130
Figure 5.10 Distance of each sample to the reference position provided by the GPS signal generator when the receiver and repeater hardware are inserted between the GPS signal generator and off-the-shelf receiver.....	130
Figure 5.11 Estimated position with and without the repeater-receiver hardware .....	131
Figure 5.12 Satellites represented within the directional antenna's angle of view.....	133
Figure 5.13 Satellite represented with the highest CNO in the directional antenna's angle of view .....	134
Figure 5.14 Terms contributing to measured pseudorange.....	134
Figure 5.15 2 <sup>nd</sup> repeater position and pseudorange.....	135
Figure 5.16 Solution to the system of two equations for 1D positioning .....	137
Figure 5.17 Test setup for 1D Positioning.....	138

Figure 5.18 The region surrounded by the blue curve corresponds to the visible region by repeater 1 while the green curve surrounds the region visible to repeater 2.....	138
Figure 5.19 Satellite constellation within the directional antenna's angle of view .....	140
Figure 5.20 PR1, clkb, dst, and d1+clkb terms when G4 is selected from repeater 1 ..	141
Figure 5.21 PR2, clkb, dst, and d2+clkb terms when G14 is selected from repeater 2	141
Figure 5.22 d1 distance, d1+clkb and d2+clkb and CNO ratios for G4 and G14 .....	142
Figure 5.23 PR1, clkb, dst, and d1+clkb terms when G17 is selected from repeater 1	144
Figure 5.24 PR2, clkb, dst, and d2+clkb terms when G31 is selected from repeater 2	144
Figure 5.25 d1 distance, d1+clkb and d2+clkb and CNO ratios for G17 and G31 .....	145
Figure 5.26 d1 distance, d1+clkb and d2+clkb and CNO ratios for G4 and G31 .....	146

## LIST OF TABLES

Table 3.1 Overview of Repeater Hardware Modules .....	32
Table 3.2 Off-the-shelf GPS Active Antenna Specifications [79].....	37
Table 3.3 Received Power and Calculated Gain of GPS Active Antenna.....	40
Table 3.4 Summary of Designed 433 MHz Patch Antennas .....	76
Table 3.5 Circuit boards and Linear voltage regulator chips used to supply them with the required input voltage .....	82
Table 4.1 Overview of Receiver Hardware Modules .....	87
Table 4.2 Some features of AEACAC053010-S433 [93].....	90
Table 4.3 LO polarity settings [84].....	102
Table 4.4 Circuit boards and Linear voltage regulator chips used to supply them with the required input voltage .....	110
Table 5.1 End-to-end measurement results with GPS signal generator .....	128
Table 5.2 Comparison of the estimated and reference points.....	131
Table 5.3 1D Positioning Tests and Selected Satellites.....	139
Table 5.4 Calculated distances from receiver to repeaters 1 and 2 in test 1 .....	143
Table 5.5 Calculated distances from receiver to repeaters 1 and 2 in test 2.....	146
Table 5.6 Calculated distances from receiver to repeaters 1 and 2 in test 3.....	147
Table A.6.1 Thermal analysis of the linear voltage regulators used for repeater .....	153
Table B.6.2 Thermal analysis of the linear voltage regulators used for receiver .....	157

## LIST OF SYMBOLS

$PR_u^i(\text{corr})$	Corrected pseudorange measurement to satellite $i$
$X^i, Y^i, \text{ and } Z^i$	Geocentric coordinates of the $i^{\text{th}}$ satellite position
$X_u, Y_u, \text{ and } Z_u$	Geocentric coordinates of the receiver position
$C_u$	Receiver clock offset in meters
$PR_u^i(\text{measured})$	Measured pseudorange to satellite $i$
$C^i$	$i^{\text{th}}$ satellite's clock offset
$I_u^i$	Ionospheric
$T_u^i$	Tropospheric delays
$NF$	Noise Figure of a cascaded system
$F_i$	Noise Figure of the $i^{\text{th}}$ element in a cascaded system
$G_i$	Gain of the $i^{\text{th}}$ element in a cascaded system
$\epsilon_r$	Dielectric constant
$\tan\delta$	Tangent loss
$f_{RF}$	RF signal frequency
$f_{LO}$	LO frequency
$\theta_{JA}$	Thermal resistance
$\Delta T$	Temperature change
$^{\circ}C$	Celcius degree

## LIST OF ABBREVIATIONS

GPS	Global Positioning System
RF	Radio Frequency
1D	One Dimensional
2D	Two Dimensional
ECC	The Electronic Communications Committee's
ETSI	European Telecommunication Standards Institute's
NTIA	National Telecommunications and Information Administration
ISM	Industrial Scientific Medical
RSS	Received Signal Strength (RSS)
CSI	Channel State Information (CSI)
AoA	Angle of Arrival (AoA)
ToA	Time of Arrival (ToA)
TDoA	Time Difference of Arrival (TDoA)
RToF	Return Time of Flight (RToF)
PoA	Phase of Arrival (PoA).
RFID	Radio Frequency Identification Device (RFID)
UWB	Ultra-Wideband (UWB)
IoT	Internet-of-Things (IoT)
GNSS	Global Navigation Satellite System (GNSS)

SVM	Support Vector Machine (SVM )
kNN	k-Nearest Neighbor (kNN)
BLE	Bluetooth Low Energy (BLE)
MAC	Medium Access Control (MAC)
LANDMARC	Location Identification based on Dynamic Active RFID Calibration
WiMAX	Worldwide Interoperability for Microwave Access (WiMAX)
3G	Third-Generation (3G)
VLC	Visible Light Communication (VLC)
LED	Light Emitting Diode (LEDs)
HS-GNSS	High Sensitivity GNSS (HS-GNSS)
A-GNSS	Assisted GNSS (A-GNSS)
PRN	Pseudorandom Noise (PRN)
FDMA	Frequency Division Multiple Access (FDMA)
Rx/Tx	Receiver-and-Transmitter (Rx/Tx)
M-LMS	Multilateral Location and Monitoring Service (M-LMS)
WLAN	Wireless Local-Area Network (WLAN)
MEO	Medium Earth Orbit (MEO)
TT&C	Telemetry, Tracking, and Command (TT&C)
WGS84	World Geodetic System 1984 (WGS84)

NLOS	Non-Line-Of-Sight Conditions (NLOS)
LO	Local Oscillator (LO)
LNA	Low Noise Amplifier (LNA)
BPF	Band Pass Filter (BPF)
CNO	Carrier to Noise
CNR	Carrier to Noise Ratio

## CHAPTER 1 INTRODUCTION

It was thought that locating the people and the objects on the surface of the Earth would have been no longer a problem as of 1993 when Global Positioning System (GPS) became fully operational with 24 satellites on the orbits around the Planet Earth, yet it remained unsolved when it comes to locating the people not on the surface of the Earth, but within the buildings.

Firstly, introduced for military purposes, GPS has become an available technology for civilian usage as the prices of GPS receivers dropped through time. Its reliability, openness, and being free of charge make GPS one of the essentials of modern life with its applications in areas such as aviation (next-generation flight safety systems), maritime, road transportation (fleet tracking, route inspection, speed control), urban transportation (access to the address, route finding), sports (mountaineering, hiking, cycling), communication networks, weather forecasting, and so many others. Besides GPS receivers offered by companies, different maps and databases for the above applications are also offered.

Although GPS applications are wide-spread outdoors, they are not fully available indoors since the power level of GPS signals has already decreased to the level of  $-158.5$  dBW ( $-128.5$  dBm) when it reaches to the Earth [1]. In addition to the very low signal level attributed to the GPS signals, the materials of the building structures attenuate the signal

further by 20-30 dB [2]. Therefore, a conventional GPS receiver may not be located indoors easily.

A method to enhance the coverage of GPS systems indoors is to deploy so-called GPS repeaters. Deploying at least three repeaters that do not interfere with each other and amplifying the GPS signals picked by directional antennas, 2D positioning is possible indoors [3], [4]. However, the usage of this method is restricted by regulations and standardizations such as The Electronic Communications Committee's (ECC) Reports 129 and 145, European Telecommunication Standards Institute's (ETSI) standard EN 302 645, NTIA's Manual of Regulations and Procedures for Federal Radio Frequency Management (sections 8.3.28 to 8.3.30).

In this thesis, a novel GPS repeater architecture operating in 433 MHz ISM band, which is independent of the restrictions forced by the regulations listed above, is proposed. Picking up the GPS signals with directional active GPS antennas at three different locations and directions, the GPS signal at 1575.42 MHz is down-converted to 433 MHz ISM band and then amplified and filtered for indoor transmission. The GPS signal down-converted to 433 MHz ISM band is transmitted indoors to be received by an indoor mobile receiver. Prior to signal processing in a conventional GPS receiver, the receiver at 433 MHz filters, amplifies and then up-converts the signal to 1575.42 MHz GPS frequency in that a conventional GPS receiver can process the received signal indoors.

The novel repeater architecture consisting of a transmitter side that down-converts the GPS signal to 433 MHz ISM band and a receiver side that up-converts the 433 MHz signal to 1575.42 MHz GPS frequency (Figure 1.1).

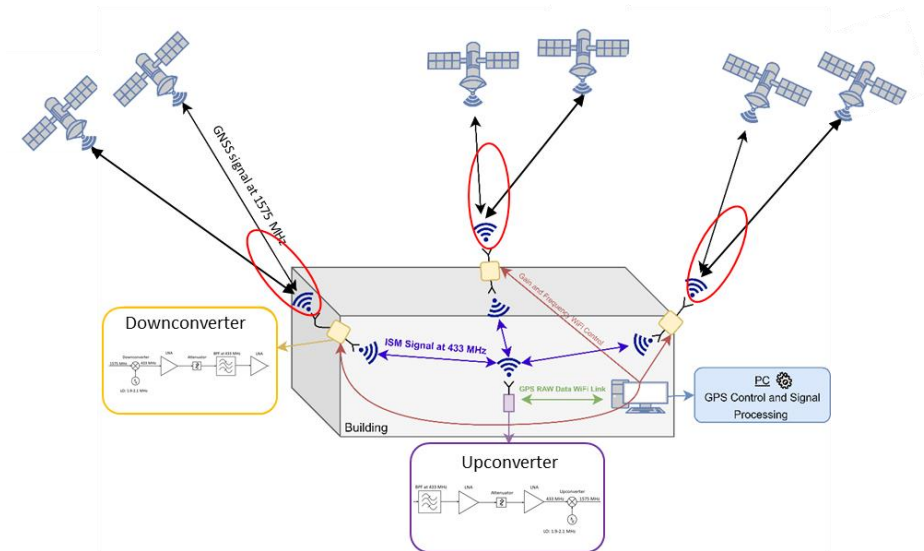


Figure 1.1 The proposed three-repeater system for 2D indoor positioning

The indoor positioning system uses the triangulation method to find the position of the receiver. This method uses line-of-sight distance from several reference points. Finding this distance with reference points is done with simple geometric operations. Then, positioning is done by using intersecting the three circles each of which has a radius of calculated distances.

In the proposed architecture, the down-converters are used as reference points in the proposed indoor positioning system. The triangulation method is applied over the distance between the down-converters and the receiver. Ordinary GPS algorithms take GPS satellites as the reference and cannot position correctly because the line-of-sight is not straight. Calculating the distance between the receiver and the down-converter by taking the down-converters as a reference is done in a few steps.

First, pseudo range measurements, ephemeris data of each satellite, the timing solution, and finally the ionosphere parameters are taken from the GPS receiver. Pseudo range measurements are the distance measurements of the receiver. This measurement includes the distance from the satellite to the down-converter and the distance from the down-converter to the receiver. The ephemeris data is used to calculate the satellite's position. Since the locations of the down-converters are already known, the distance between the

satellite and the down-converter can be calculated. In this way, the distance between the repeater and the receiver is measured. The timing solution of the receiver is found with the offset solution when the receiver itself is located. Finally, the effects of ionosphere, troposphere effects, satellite clock offset, satellite orbital errors, errors caused by Earth-orbital movements, and satellite movements are excluded to calculate the position indoors.

## **1.1 Literature Review**

The global indoor positioning market is an expanding market that was forecasted to expand by a 42% compound annual growth rate from 2017 to 2023 in the latest researches [5], [6]. The forecasted growth promises the requirement for new techniques, technologies, and approaches in the field.

There are several techniques proposed in the literature. These techniques include Received Signal Strength (RSS), Channel State Information (CSI), fingerprinting, Angle of Arrival (AoA), Time of Arrival (ToA), Time Difference of Arrival (TDoA), Return Time of Flight (RToF), and Phase of Arrival. Aforementioned techniques underlie the technologies such as IEEE 802.11, Bluetooth, Zigbee, Radio Frequency Identification Device (RFID), Ultra-Wideband (UWB), Visible Light, Acoustic, Ultra-Sound, emerging Internet-of-Things (IoT) technologies including LoRa, IEEE 802.11ah, weightless [7], [8]; and GNSS based solutions for indoor positioning [2].

In the RSS method, the distance between a transmitter and a receiver is calculated by the signal power loss with a path loss model [9]. Although RSS is a low cost and easily deployable technique, the accuracy of the technique is low indoors because RSS is not immune to multipath effect and signal attenuation caused by building structure and indoor environment [10]. Unlike the RSS, which captures only the average power over the

bandwidth, CSI provides both amplitude and phase responses of the channel [10]. However, CSI is not an available technology in many devices which restricts the use of the technique.

Another RSS/CSI based technique is fingerprinting. At different positions on a grid structure, the RSS or CSI measurements are taken and stored. Then, these data are compared with online RSS or CSI measurements to locate the device. However, this technique also suffers from negative features attributed to RSS and CSI. There are many algorithms to compare stored and online measurements such as probabilistic methods [11], artificial neural networks, Support Vector Machine (SVM), and k-Nearest Neighbor (kNN) [12]. As the distance between two points where the offline measurements are taken is reduced, the RSS levels of the closer points reach the same level. Then, the location cannot be found successfully.

The angle of arrival technique estimates the location using an array of antennas at the receiver for determining the angle of the incident wave [13]. Other than the antenna arrays, this technique requires sophisticated algorithms to be implemented along with complex hardware. The AoA method is prone to produce high errors in location calculation when the transmitter and receiver are removed further from each other. The small errors in the calculation of arrival angle cause a greater error in estimating the location [14]. An indoor positioning system called UbiCarse uses the AoA technique was proposed by Kumar et al. [14]. Although it provides high accuracy, the system needs at least two antennae on the receiver side and twisting motion to receive signal as it does not deploy more than 2 antennas. Therefore, practically it could be a problem for the users especially when the device is in an unreachable area[7].

Time of Arrival (ToA) is another technique used for indoor positioning applications. In this method, knowing the speed of propagation in the environment, one can measure the distance from the transmitter to the receiver [8]. For this technique, the transmitter and receiver must be synchronized. Another solution technique the Time Difference of Arrival (TDoA) also requires synchronization. TDoA uses the difference of propagation of the signals from different transmitters. Therefore, all the transmitters must be

synchronized. There must be at least three transmitters to be able to locate the receiver with triangulation [12]. Yet another system based on propagation time calculation is the Return Time of Flight (RToF) technique. Similar to ToF, this technique exploits the propagation time of the signal from transmitter to receiver. On top of that, it also exploits the propagation time of the signal from the receiver back to the transmitter [15]. The synchronization requirement between transmitter and receiver is required but less strict compared to ToA. However, when non-line-of-sight conditions that generally exist in an indoor environment occur, synchronization errors arise leading to techniques that require synchronization to estimate incorrect locations.

The phase of Arrival technique calculates the distance between a transmitter and receiver by exploiting the phase of the received signal [16]. For this technique to perform with high accuracy, it requires non-line-of-sight conditions. Therefore, PoA may not result in high accuracy systems for indoor positioning systems.

Among some of the technologies that provide indoor positioning services, IEEE 802.11 (a.k.a Wi-Fi) is one of the most researched technologies as most of the devices such as smart-phones and laptops have Wi-Fi technology [17],[18], [19],[20],[21]. On top of the availability of Wi-Fi in those devices, the existing Wi-Fi access points in indoor environments can serve as reference points eliminating the need for additional infrastructure costs [14]. Previously described techniques are deployed for Wi-Fi oriented indoor positioning systems. However, there exist many other applications at 2.4 GHz ISM band that would cause interference. The interference caused by other devices is shown to deteriorate the system performance in [22]. In addition to the interference, Wi-Fi access points are designed indoors such that they generally do not overlap with each other. Hence, the assumption to use existing Wi-Fi access points may result in poor signal coverage using the aforementioned techniques as they may require methods such as triangulation to estimate the location.

Indoor positioning services are also implemented using Bluetooth technology after Bluetooth Low Energy (BLE) is introduced as the older versions of Bluetooth are not adequate for fine-grained low latency positioning applications [23]. BLE is capable of

covering up to 100 meters [24]. Since the RSS technique provides simpler solutions indoor positioning with BLE services rely on the RSS technique [7]. However, Faragher and Harle in [11] note that fast-fading interference affects the BLE more than the Wi-Fi. Another difficulty in BLE deployment is to decide where beacons should be located. Faragher and Harle [11] show also that determining beacon locations may require a detailed search and a lot of effort. Indoor positioning with beacons, therefore, requires many beacons to be placed in an indoor environment, for instance, Castillo-Cara et al. suggest deploying beacons with at least 6 meters of separation [25].

Zigbee technology is another research area for indoor positioning. Zigbee is based on the IEEE 802.15.4 standard with the physical and MAC layers [26]. In their work, Aykaç et al. [27] show that a Zigbee-based indoor positioning system could reach an accuracy of 2 meters by using reference points whose coordinates are known. However, this system is based on RSS measurements and suffers from the negative features attributed to said technique. Determining the reference points for offline RSS measurement and knowing their coordinates globally may require GPS based solutions [26], yet building structure and walls will not let GPS signals to pass through and even a receiver cannot detect the signal, the system may fail. There are also systems where connectivity between nodes and positioning algorithms are used to decide reference points' coordinates globally by utilizing a few GPS receiving nodes as reference points, but still, there is a need for GPS signals indoors.

RFID technology is yet another basis for indoor positioning systems based on proximity or RSS lateration technique. Primarily, RFID technology is developed to store data such as the ID of a tag, and transfer data with RF signals from the tags to an RF reader. The systems based on RFID for localization are designed such that the location information is not given globally, but rather the location is estimated concerning an existing checkpoint such as a gate, an object within the room, etc [28]. Location Identification based on Dynamic Active RFID Calibration (LANDMARC) is a well-known RFID based indoor positioning system where the median accuracy of 1 meter is achieved by using 4 RF reader and 1 reference tag for calibration per square meter [29]. As the signal strength cannot be sent directly in this system, LANDMARC scans various power levels. Scanning

various power levels, and the required time duration of 7.5 seconds between two successive ID emitted by an active tag leads to a long latency for the system. Moreover, for RFID based systems, the accuracy is highly dependent on how close the tags have been placed to each other in an indoor environment.

Indoor positioning is handled using UWB techniques as well. Federal Communications Commission defines a UWB system or device with a bandwidth of 500 MHz or more in the frequency from 3.1 GHz to 10.6 GHz in the USA [30]. In UWB-based indoor positioning systems, the pulse duration of a transmitted signal is on the order of nanoseconds. As a result of a very short pulse duration, the multipath fading is alleviated by UWB systems even for indoor environments. Common techniques for UWB systems are ToA and TDoA. UWB based systems require the tags to be placed as in the case of ZigBee and RFID technology. On top of that, the costs for tags and application requirements are high to meet [8]. Another concern regarding UWB-based systems is that UWB is still susceptible to interferences from metallic liquid materials although it alleviates the multipath-fading [12]. Moreover, UWB-based systems may be affected by systems that operate in the UWB spectrum such as Worldwide Interoperability for Microwave Access (WiMAX) and digital TV in USA or third-generation (3G) communication devices in some countries due to improper design of UWB systems [31]. Besides, there are some other concerns such as UWB interference to existing GPS and aircraft navigation systems from UWB [32]. Yet, among the aforementioned technologies, UWB stands out with the features of high accuracy (even in the existence of multipath), low power and license-free operation, and effectively passing through walls [33].

Indoor positioning with Visible Light Communication (VLC) is another growing research area for applications requiring high-speed data acquisition and transmission [34], [35]. The fast switching Light Emitting Diodes (LEDs) modulates and emits the optical pulses at a frequency range from 400 THz to 800 THz [7]. The main disadvantage of VLC is the requirement of the line of sight between the LED and the sensors for positioning, but the line of sight is a limitation for indoor positioning applications due to the walls and building structure.

Modulated acoustic signals are also used for positioning systems. ToF technique is used for estimating the position using the microphone sensors that sense the acoustic signals modulated and including a timestamp [36]. Some other acoustic-based systems use the frequency and time shift due to the Doppler effect to figure out relative distance and velocity from the smartphone to acoustic signal sources [37]. As these systems use smartphone microphones to sense the acoustic waves, only those signals within the audible band can be received properly, which means that signals below 20 kHz frequency can be sensed for high accuracy indoor positioning. Therefore, in order not to disturb people and not to cause sound pollution in an indoor environment, the power level of audible signals must be kept low. This technology also requires the deployment of anchor points and hardware installation [7].

The sound waves with frequency higher than 20 kHz are out of the audible band and called Ultrasound. Some systems are built upon ultrasound technology and ToA calculations to estimate the location such as The Cricket Location System in [38] that finds the nearest beacon and takes the reflection of sound waves from the walls. Hazas M. and Hopper A. note that centimeter-level accuracy can be achieved by using ultrasound technology [39]. However, ultrasound signals are affected by the transmission medium's humidity and temperature [40]. In the scope of indoor positioning systems, it is the humidity in the air and the temperature of the indoor environment that affect the performance of the ultrasound-based systems.

Some systems are based on infrared technology. Infrared based positioning system can estimate the location with high accuracy. However, infrared-based indoor positioning systems require a line of sight between the transceiver and receiver; and infrared-based systems can be damaged by a strong obstacle such as the sun [41]. Therefore, the usage of infrared systems for indoor positioning is not promising.

Internet-of-Things (IoT) technologies including LoRa, IEEE 802.11ah, weightless are also emerging research areas for positioning systems. There are still some issues regarding these technologies from the positioning system point of view. These issues arise from the long-range from a base station to user/device, multipath effect in between, and

walls of a building. These issues prevent these technologies to be applied for accurate position finding both indoors and outdoors [7].

Indoor positioning systems using Radio Frequency signals are not only limited to RFID, Bluetooth, WLAN, and UWB. Indoor positioning systems summarized above have yet another RF-based technology that tries to bring together indoor and outdoor positioning solutions together. This joint solution could only be possible using Global Navigational Satellite Systems (GNSS) and especially the US Global Positioning System (GPS). It has become possible to travel door-to-door using online maps and GPS services since GPS became fully operational for civilian usage. To carry GPS solutions indoors, many systems and techniques are proposed in the literature to solve the so-called “the last kilometer” problem, which is the term used for indoor positioning from the global navigational point of view. The technologies using GNSS are GNSS based technologies such as indoor positioning with pseudolites, High Sensitivity GNSS (HS-GNSS), Assisted GNSS (A-GNSS), and GNSS-repeaters. These techniques are important for the continuity of the outdoor and indoor positioning applications for personal digital assistant location, asset tracking, vehicular navigation, and emergency services [42]. Among the GNSS-based techniques, HS-GNSS and A-GNSS technologies require no infrastructure within the indoor environment while pseudolite and repeater-based approaches require infrastructure.

In the late 90s, the assisted methods with GPS have been shown to reach encouraging results for indoor environments as they increase the integration time for position estimation [43], [44], [45]. Recent studies show that HS-GNSS and A-GNSS technologies may be viewed as complementary methods [46] for better accuracy positioning in harsh environments such as indoors. HS-GNSS receivers are developed to acquire weak satellite signals in complex environments by longer correlation [47]. Similar to HS-GNSS receivers, A-GNSS aids the receiver to acquire satellite signals in complex environments and aims to estimate the indoor location. In this method, the navigation message is sent through the existing telecommunication network (for instance, using GSM services) [48]. By using a high sensitivity receiver and A-GNSS technology, a mobile phone’s location can be estimated in complex environments. Although high sensitivity-based solutions

receive very low signal levels in harsh environments, the higher sensitivity receivers suffer from reflected signals and interference in indoor environments. HS-GNSS based solutions to indoor positioning do not guarantee to work in every indoor environment as it is difficult to decode signals at such low power levels even though the receivers have been very capable [49]. Some systems use GPS in indoor environments by using high-gain antennas [50], however, such systems also do not guarantee to work in different indoor environments as in the case of HS-GNSS based systems. Therefore, the aforementioned GNSS-based techniques that require infrastructure are proposed. These pseudolite architectures are grouped into 3 categories: pseudolite, repeater, and repealite [46].

Pseudolite approach is built on the idea to mimic and recreate the GPS satellites for the places where the number of visible GPS satellites is not adequate for location estimation [51]. Pseudolite is deployed to simulate the satellite constellation. Pseudolites are ground transmitters that receive GPS signals, compute pseudo-range, and transmit a GPS-like signal. GPS-like signal has a PN code to allow a local user to obtain an additional pseudo-range measurement to the transmitting antenna [51]. The generated GPS-like signals are in the same signal structure as GPS signals. However, the generated GPS-like signals have different navigation data, PRN code, or carrier frequency from the GPS signals [52], [53]. The effort to make use of off-the-shelf receivers without modifying the firmware to read modified navigation data is made by Rapinski et al. (2012) [52] while Rizos C. et al (2010) proposes Locatalite design in 2.4 GHz ISM frequency and spatially-diverse PRN codes to transmit the GPS-like signals [53].

Pseudolites are used for a variety of applications. For instance, to increase the vertical accuracy for landing planes, Bartone and Graas offered to use pseudolites in that the need for a satellite-like structure beneath the plane was met to enhance the vertical accuracy [54].

A recent study was conducted by Chuanzhen Sheng et al. (2020) to enhance the accuracy of positioning in urban canyons and complex environments using pseudolites [55]. However, the pseudolite-based positioning method is not only limited to augmentation of

GNSS for outdoors, but it is also used for indoor positioning. Kee C. et al. presented in their work in 2003 that an accuracy of 1 meter can be reached by locating pseudolites at the corner of the building for satellite simulation [56].

Gan et al. (2019) proposed a new array of indoor pseudolites and Z-axis fixed Known Point Initialization for Doppler positioning for centimeter-level accuracy [57]. However, the study is conducted in a high ceiling indoor environment with no walls and obstacles which is not as complex as an indoor environment generally is. Other than the continuity of outdoor positioning in a building, one of the advantages of some of the pseudolite based approach is that there is no need for synchronization between the transmitters as explained in [57].

However, some other pseudolite based systems suffer from the need for synchronization between transmitters. The pseudolite systems, in general, need to deal with the near-far effect [46]. The GPS-like signals may also require some modifications in the hardware level for the user receiver. Repeater and repealite architectures are proposed as an effort to cope with these problems.

GPS repeaters are units that pick up the GPS signals with an antenna located outside the building and retransmit those signals indoors in a sequential way in order not to cause one satellite to be transmitted from more than 1 repeater at different locations. Otherwise, when the signals from one satellite are transmitted from different repeaters at different positions, they are perceived as reflected paths [46]. Repeaters consist of an outdoor GPS antenna and switching modules that pass on the GPS signals. In their work Fluerasu et al. (2009) Highlights that the GPS signal is simply picked up with outdoor GPS antennas, amplified, and transmitted indoors by repeaters [58]. Only one repeater is active at a time while the rest of the repeaters are off. The active repeater transmits the signal over a certain period. By switching each repeater on and off in a sequence, the receiver calculates the TDoA between two consecutive repeaters as it receives the signals. In this method, estimation is done after four TDoA measurements [58].

Petrovski et al. from the company GNSS Technologies Inc. and Hitachi Ltd. present another pseudolite implementation for seamless indoor positioning [59]. The indoor

positioning problem is addressed from an algorithm point of view. An algorithm that operates with decimeter-level accuracy for indoor positioning is proposed in the related work. The algorithm achieves decimeter-level accuracy in a low multipath environment. It is not required to restrict the rover receiver movement or to know the starting position. The initial point estimation is achieved based on pseudo range measurements. For this purpose, multiple free reference stations are utilized. The code-based algorithm taking the changes in the behavior of the estimated locations with and without considering the existence of an error in the starting point. The search algorithm handles the correction of starting position through the changes mentioned. Petrovski et al. report that although it is possible to use only one GPS satellite as single signal source indoors among the all outdoor GPS signals that have been retransmitted indoors, their system, which is based on multiple GPS repeaters, does more and manages to estimate indoor position using multiple antennas with restraint view and FDMA method [59].

Another method based on multiple GPS repeaters and a modified positioning algorithm is presented in the study “Indoor Positioning Based on Global Positioning System Signals” published in *Microwave and Optical Technology Letters* 55.5 ((2013): 1091-1097) by Ozsoy et al. The proposed system process the actual GPS data live while using an off-the-shelf GPS receiver [4]. The modified algorithms in [4] can estimate indoor position with an accuracy that outdoor positioning can achieve under line-of-sight conditions. This system uses two or three sets of GPS repeaters with directional outdoor GPS antennas for satellite selection and retransmits amplified GPS signals indoors by indoor GPS antennas to increase the coverage area of GPS within a building structure where outdoor GPS signals cannot reach. Using 2 repeaters, one can achieve 1D positioning while it is required to use 3 repeaters for 2D positioning. This system does not require any change in the existing receiver hardware. All the repeaters operate individually and there is no need for synchronization [4].

Repealites are defined somewhere between a pseudolite and a repeater to cope with synchronization and multipath effect issues. Similar to repeaters, a repealite transmits picks up a GPS signal and transmit the signal indoors continuously, yet delays are induced on the transmitted signal such that the repealites can be distinguishable without any

interference [60], [61]. The user receiver measures the continuously transmitted signals which are also delayed by different periods. The reported repeater based systems in the literature [60], [61] have an accuracy of 10 cm to 70 cm. These systems are based on carrier phase measurements which are less susceptible to multipath than code-based approaches [46]. In their work, Selmi et al. [61] showed that their repeater system based on carrier phase measurement also suffers from an ambiguity resolution problem.

Other pseudolite-based indoor positioning systems have also been proposed in the literature. Xu et al. (2015) propose to receive real-world GPS signals, repeat each of the satellite signals, and transmit these signals indoors [62]. Propose Rx/Tx demodulates the real-world GPS signals coming from GPS satellites, then separates these signals and repeats them, respectively. The novelty of this system lies beneath the architecture that is composed of a Receiver-and-Transmitter (Rx/Tx), a server, and a user terminal. The clock synchronization in this system is simple. All Tx can be synchronized with each other as one single clock exists in Tx/Rx. The system also does not require major modifications for an off-the-shelf GPS receiver.

Ma et al. (2018) propose a new scheme that adopts pseudolite technology and a navigation signal simulator [63]. This method also requires a map matching to prevent pseudo range errors that are calculated from the actual satellite ephemeris stored in the pseudolites.

In their study [64], Lymberopoulos et al. report their findings on the indoor positioning accuracy and overhead of 22 approaches through competition of indoor location technologies, whether they are infrastructure free or infrastructure-based. The competition takes place on a 300 meter-square evaluation space. Lymberopoulos et al. conclude that the deployment overhead is high for many systems, the system stability and reliability is questionable due to the variations in the accuracy at different evaluation locations, variation in the environment such as displacement of furniture in the setting may cause accuracy to change as in the case of some wi-fi based systems.

In addition to these studies in the literature, there are also patented solutions to the indoor positioning problem when a priori art research is conducted.

One of the patents in the literature is EP 2878974. This patent presents a method and describes the receiver structure in detail to estimate the location of a mobile cellular communication device in disclosures [65]. However, this patent does not describe an indoor positioning system. It rather describes the receiver that is capable of receiving both Multilateral Location and Monitoring Service (M-LMS) signal at 926 MHz and GNSS signal at 1575 MHz. Upon receiving an M-LMS signal, it is up-converted to GNSS frequency to be delivered to a GNSS chipset of the mobile cellular communication device. The chipset estimates the location using the up-converted M-LMS positioning signal [65].

Another patent in the literature is CN 106767831. This patent provides a simulated GNSS signal-based indoor locating system comprising outdoor receivers, an indoor simulation signal generator, simulation signal emitters, and indoor locating modules [66]. The system is built on outdoor GNSS signals. Outdoor receivers collect the self-locating information and send it as a telegraph text signal. The simulation signal generator is located in an indoor environment to generate simulated signals in simulation satellite frequency and band according to received GNSS location information as a telegraph text signal. The simulation signal emitters are located in an indoor environment and in different directions to emit simulation navigation signals indoors. Receiver in an indoor environment receives the stimulation signals of emitters for location estimation [66].

Another GPS-based indoor positioning system patent is EP 1720032. This patent presents a system that receives GPS signals by a single outdoor receive antenna and up-converts to four different carrier frequencies in the 2.4 GHz ISM band [67]. The up-converted signals are transmitted to four different transmit antennas located at four different locations through RF cables inside the building. RF cabling requirement indoors is one of the main drawbacks of the system as it is not cost-efficient and not easy to deploy in large buildings. It may also cause a high RF signal loss. The transmit antennas indoors also serve as access points of a WLAN that is used to transmit not only up-converted GNSS signal but also to transmit antenna positions and signal delays for each transmitter. The GNSS signal at 2.4 GHz ISM band is received and down-converted in the receiver indoors. The receiver cycles through the second positioning signals that are received from the transmit antennas during an assigned time slot for each transmitter in that the position

is estimated using the TDoA method [67]. The system proposed in this patent suffers from the previously mentioned drawbacks of Wi-Fi-based methods such as high path loss at 2.4 GHz frequency and interferences in the 2.4 GHz ISM band. Moreover, existing access points are designed for communication. Therefore, receiving a signal from 4 access points at any location is not that simple. Moreover, the proposed system does not clearly describe how synchronization between transmitters is accomplished. The switching between transmitting antennas may also cause phase jumps that may prevent decoding the GNSS signal.

Tekin et al. propose another GPS repeater-based indoor positioning system in US 2012286992 A1 where the proposed system is composed of at least three outdoor directional GPS antennas and repeaters that amplify and retransmit GPS signals indoors with indoor GPS antennas, and a receiver indoors [3]. The calculation method for indoor positioning is also presented within the patent.

In this thesis, a repeater system with a transmitter that down-converts the GPS signal and transmits down-converted signal has been proposed along with a receiver that up-converts the navigation signal indoors to process in an off-the-shelf GPS receiver.

## **1.2 Motivation**

Developing an indoor positioning system based on GPS is crucial to the success and accuracy of many indoor applications and continuity of positioning from outdoor to the harsh environments where the GPS signals cannot reach adequately such as buildings. Although there are many solutions in the literature to indoor positioning, the problem remains unsolved. The variety of existing indoor positioning systems tells us a fact: there is still no technology that is superior to others in terms of accuracy, deployment overhead, stability, reliability, and coverage.

Researchers attempt to fill the gap of knowledge in the field because GNSS technology performs poorly indoors unlike the outdoors. Although GNSS technology demonstrates a superior positioning performance outdoors, the indoor performance of such systems suffers from the following drawbacks:

- Signal reflection and multipath from building walls and obstacles such as furniture
- Signal attenuation and blocking up to 20-30 dB [2] due to construction materials
- Non-Line-of-Sight conditions
- Environmental changes due to displacement objects or movement of people indoors
- Interferences from other the RF devices

GPS-based indoor positioning can provide continuity between outdoor and indoor. Besides, the need for a GPS-based system performing just well as it performs outdoors in terms of coverage, accuracy, short latency, and so on is the initial motive beneath this study. However, GPS-based systems operating in L1, L2, and L5 bands are supposed to comply with the practices set by the authorities. To comply with practices, the existing GNSS repeater systems forego the coverage area which reduces the availability of the service indoors.

The use of GNSS repeaters is restricted to prevent repeaters from interfering with other uses of GNSS in the vicinity. The Electronic Communications Committee's (ECC) Reports 129 and 145, European Telecommunication Standards Institute's (ETSI) standard EN 302, and the US policy "Manual of Regulations and Procedures for Federal Radio Frequency Management" under section 8.3.28 present the practices on the use of GNSS repeaters and restrictions on their usage.

This thesis work attempts to come up with a novel GPS-based solution that does not contradict with the practices set by authorities. Firstly, the proposed system in this thesis

work operates in 433 MHz ISM band to comply with the power restrictions in GNSS frequencies.

Secondly, the system proposed in this thesis work provides a GPS repeater based indoor positioning system that down-converts the GPS signals to 433 MHz ISM band where signal coverage is increased due to higher permitted power levels. In addition to higher power levels permitted in 433 MHz ISM band, the free space path loss in 433 MHz frequency is much less the while the penetration through walls is higher than it is at 1575.42 MHz (GPS operation frequency) or 2.4GHz (Wi-Fi operation frequency).

Thirdly, this thesis work presents a 1D indoor location positioning method where 2 repeaters and 1 receiver are used to estimate the position of the receiver with distances to both repeaters. This idea of 1D positioning can be expanded to 2D positioning by using 3 repeaters and LSNAV algorithm

Lastly, the results of this study deliver novel developments in the field.

## CHAPTER 2 GPS OVERVIEW

The signals for civilian use are in the carriers of the legacy signal L1 (1575.42 MHz); and modernized signals L2C (1227.60 MHz), L5 (1176.45 MHz), and L1C (1575.42 MHz). The atomic clocks in the satellite generate a fundamental frequency of 10.23 MHz. By multiplying the fundamental frequency by 154, the L1 carrier frequency is generated. The two pseudorandom noise (PRN) codes (the course-acquisition and precision codes), and the navigation message are sent to receivers by superimposing on the carrier frequency of the GPS signals.

The GPS segments, basic principles of operation, and the use of GPS for indoor positioning are explained under sections 2.1, 2.2, and 2.3, respectively. The main approach in this thesis is based on down-conversion of GPS signals to license-free 433 MHz ISM band in repeaters and up-conversion of GPS signals back to 1575.42 MHz in the receiver as explained briefly under section 2.3.

## 2.1 GPS Segments

The Global Positioning System is divided into three segments, namely, the satellite constellation (space segment), ground control/monitoring network (control segment), and user receiving equipment (user equipment segment). These three segments that compose the GPS are demonstrated in Figure 2.1.

The space segment consists of the GPS satellites which send the navigation signals and data to the user segment. The control segment monitors the satellites in orbits around the world and maintains the proper operation of the satellites by updating the satellite clock corrections and ephemerides and many other parameters. The user segment tracks GPS signals and calculates the position and velocity of the user device.

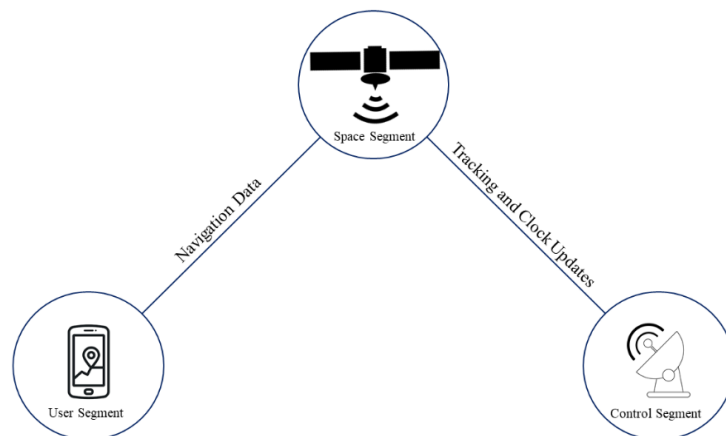


Figure 2.1 GPS Segments

### 2.1.1 Space Segment

There have been 31 satellites operating in the GPS constellation as of February 20, 2020, excluding those that were decommissioned [68]. At least four satellites can be viewed at

any place on Earth due to the four baseline slots in six equally spaced orbital planes around the planet. In June 2011, 27-slot constellation is taken into operation with additional satellites into the baseline for better coverage and robustness in harsh environments.

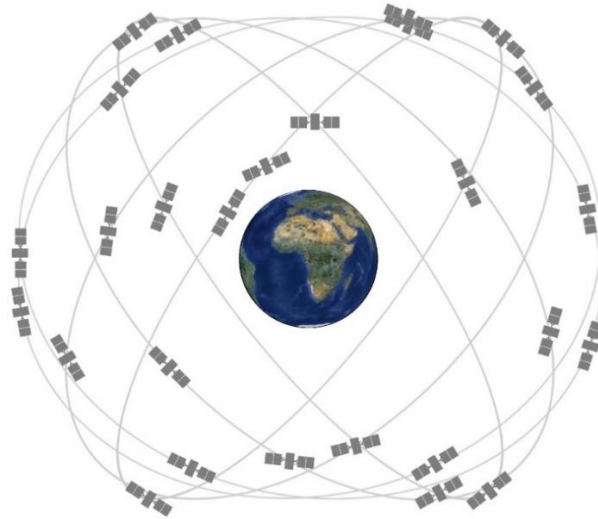


Figure 2.2 GPS Satellite Constellation [68]

The GPS satellites rotate around the Earth twice a day with a period of 11 hours 58 minutes and positioned in medium Earth orbit (MEO) at an altitude of ~20200 km [69].

### 2.1.2 Control Segment

The GPS constellation is monitored, commanded, and controlled by the control segment, which is composed of monitor stations, master control station, and ground antennas. The satellite clock, ephemeris, almanac, and other parameters in the navigation message is updated by the control segment [70].

Monitor stations are responsible units for tracking GPS satellites going over, gathering navigation signals, getting measurements for range and atmospheric data. Monitor stations feed the monitored information to the master control station.

Master control station commands and controls the GPS constellation by using the monitor station observations. The master control station provides navigation data to be uploaded to the satellites. Constellation accuracy, optimality, and maintenance are also performed by the master control station.

Ground antennas are responsible to send commands and navigation data updates to the satellites and to collect telemetry. For this reason, the ground antenna facilities store and uploads telemetry, tracking, and command (TT&C) data. For each satellite, a unique TT&C is prepared by the master control station. Ground antennas transmit TT&C to satellites in the view over S-Band [70].

### **2.1.3 User Segment**

The user segment refers to GPS receiver devices that pick up L-band GPS signals and process to find user position, velocity, and precise time.

## **2.2 Principles of Operation**

The satellite signals are transmitted originally in two frequencies; one at 1575.42 MHz (L1), and one at 1227.60 MHz (L2). The transmitted signals are exposed to phase change when it reaches the receiver. The phase-change pattern is unique for each satellite [71].

A copy of the phase-change pattern is produced by the receiver. This copy signal is correlated with the received signal by shifting it back and forth in time. If the signal that it is trying to correlate with is received, there occurs a match between the received signal and generated signal. Then the receiver locks on to the corresponding satellite. The amount of time shift in the generator shows the time that the signal reached the receiver with respect to the receiver's clock. If the receiver's clock is known with respect to the GPS clock, then the exact amount of traveling time from the satellite to the receiver is known. The distance between the satellite and receiver is found by multiplying the traveling time of the signal with the speed of light. Pseudorange represents the distance between the satellite and the receiver, but it is measured in time unit as the speed of light is a constant multiplier. The pseudo ranges are measured with the same time error as the receiver uses the same clock for all measurements.

The navigation message is also transmitted by the GPS satellite. The navigation message is composed of data such as the ephemeris, almanac, the current GPS time (in seconds), and the correction terms for the satellite clock. The receiver clock is corrected using these pieces of information.

In addition to reading the current GPS time in navigation message and setting its clock to the satellite clock, the receiver gets the ephemeris data that characterize the satellite position on the orbit at a given time. The receiver calculates the position of the satellite in the World Geodetic System 1984 (WGS84) from the ephemeris data [72].

Knowing the position of the satellite and the pseudorange is adequate to describe the location of a receiver on a sphere with a radius of pseudorange multiplied by the speed of light, and centered at the satellite position. In theory, a receiver would estimate its location if signals from three GPS satellites can be received. In that case, the receiver position can be estimated at the intersection of the three spheres (Figure 2.3). In this case, range measurements to 3 different satellites are expected to be adequate. However, the clock offset, which is defined as the time difference between the receiver clock and GPS time, is another unknown parameter in addition to  $x$ ,  $y$ , and  $z$  of the receiver (receiver position)

[70]. Therefore, the user can calculate its position by an additional range measurement to a fourth satellite for the fourth unknown, receiver clock offset.

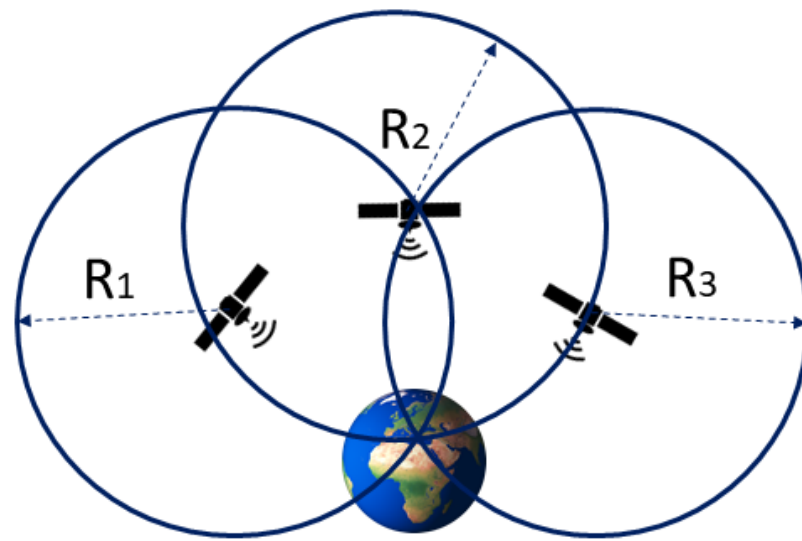


Figure 2.3 Basic principle of GPS positioning

There are also other sources of GPS errors. GPS errors occur due to different aspects of the system such as geometric locations of the GPS satellites seen by the receiver, ephemeris errors, satellite clock errors, receiver clock errors, multipath error, receiver noise, the propagation delays, and so on (Figure 2.4)

The ephemeris data brings 30 cm of accuracy and the location of a satellite is based on the ground observations [71]. There are also errors due to the computational precision of the receiver. When the transmitted signals propagate through space, the ionosphere layer causes shifting the signal and bending its path. The troposphere also affects its speed and path. Around the receiver environment, there occur reflections from buildings, water, and

other objects. This means that the reflected signals travel along a longer path, or namely, the multipath effect.

The geometric position of the satellites seen by the receiver is also an important aspect of the accuracy. As the satellites spread out, the satellite geometry yields a better-estimated position [73]. This phenomenon is called the Dilution of Precision.

The satellite clocks can also cause errors in the positioning. Although the satellite clocks are highly accurate [72], there is still drift. The drift is monitored by ground stations and send in the navigational message to the receiver for the correction. However, there are still some residual errors that may affect the accuracy of a few meters [72].

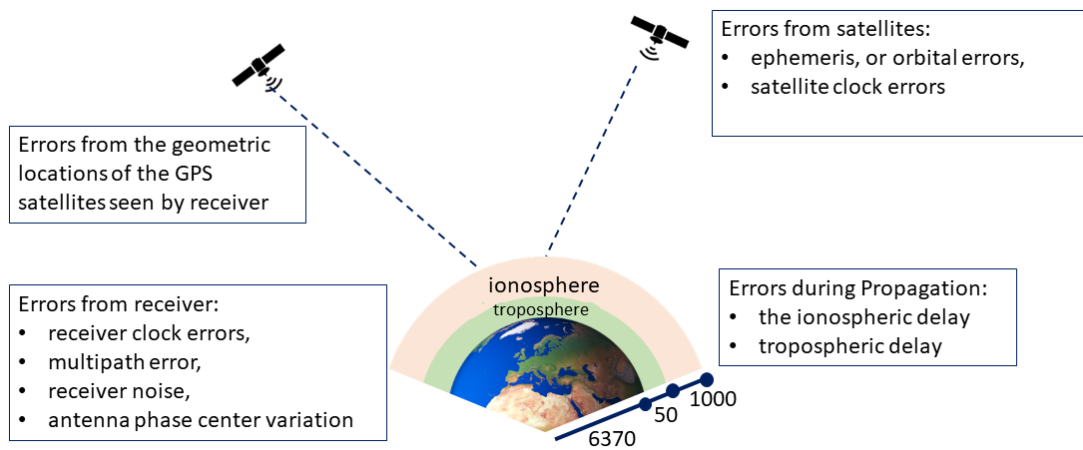


Figure 2.4 GPS Errors [72]

As mentioned previously in this section, the locally generated code in the receiver is compared to the code transmitted from the satellite for the propagation time of the signal. The navigation message and the calculated propagation time enable the receiver to calculate its position at a certain time. The range from satellite to receiver is calculated with the Pythagorean theorem [74].

The pseudorange equation is corrected by taking some of the error sources into account. For the corrected pseudorange equation a range measurement to the fourth satellite is included to solve for the receiver clock offset, clock parameters of the satellite in

navigation message are used to calculate satellite clock offset, and ionospheric and tropospheric delay models used to correct the delays due to the change in the speed of light in these mediums. The corrected pseudo range measurement is given in Eq. 2.1 where  $PR_u^i(corr)$  represents the corrected pseudorange measurement to satellite  $i$ ;  $X^i$ ,  $Y^i$ , and  $Z^i$  denote the geocentric coordinates of the  $i^{\text{th}}$  satellite position;  $X_u$ ,  $Y_u$ , and  $Z_u$  stands for the geocentric coordinates of the receiver position while  $C_u$  denotes the receiver clock offset in meters [74]. Note that  $i$  ranges from 1 to at least 4 for 3D positioning, and 1 to at least 3 for 2D positioning.

$$PR_u^i(corr) = \sqrt{(X^i - X_u)^2 + (Y^i - Y_u)^2 + (Z^i - Z_u)^2} - C_u \quad (2.1)$$

The corrected pseudorange ( $PR_u^i(corr)$ ) is derived from the measured pseudorange ( $PR_u^i(measured)$ ) as given in Eq. 2.2 where  $C^i$  represents the  $i^{\text{th}}$  satellite's clock offset while  $I_u^i$  and  $T_u^i$  stands for ionospheric and tropospheric delays, respectively [74]. Note that  $i$  ranges from 1 to at least 4 for 3D positioning, and 1 to at least 3 for 2D positioning.

$$PR_u^i(corr) = PR_u^i(measured) - C^i - I_u^i - T_u^i \quad (2.2)$$

### 2.3 GPS Based Indoor Positioning

When it comes to indoor positioning based on GPS, the approach is to deploy a repeater system which increases GPS coverage to indoor environments as mentioned in Section 1.

At least 3 repeaters that pick signals from 3 different satellites are necessary to enable such a system for 2D position estimation indoors. If each repeater retransmits a different

satellite's GPS signal, then these repeaters can work simultaneously without any need for switching [4]. Such a repeater system is shown in Figure 2.5.

The system in Figure 2.5 leads to errors due to the non-line-of-sight conditions (NLOS). The calculated difference using the repeaters differs from the line-of-sight distance. Off-the-shelf receivers estimate the location assuming that the total range ( $R_i + r_i, i = 1, 2, 3$ ) is the line-of-sight distance [4]. The triangulation of these measurements results in an incorrect position. This erroneous position is calculated as in Eq. 2.1. However, the calculation can be modified to correct the estimation for indoor non-line-of-sight conditions.

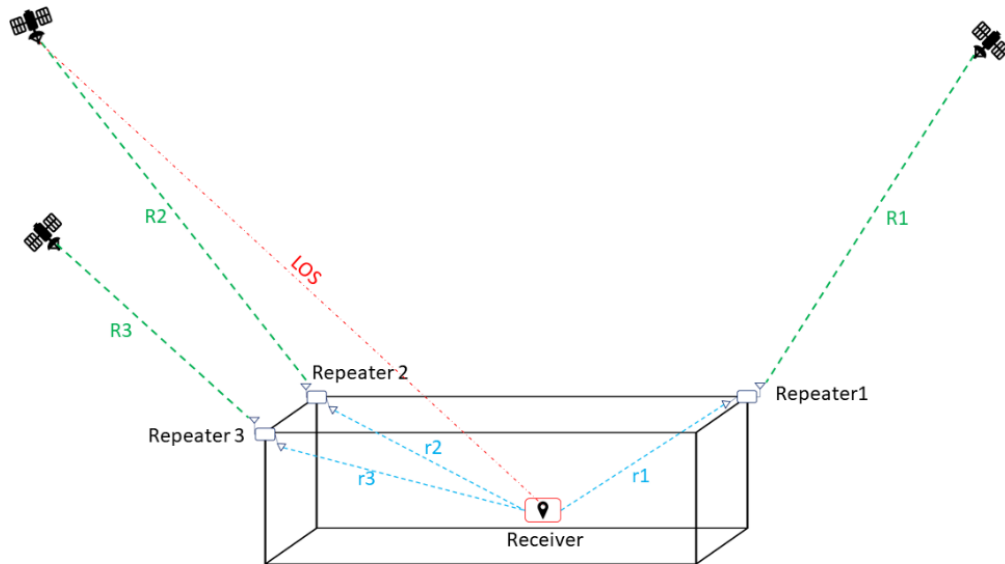


Figure 2.5 Overview of 2D Indoor Positioning Based on GPS

The calculated pseudorange in the GPS receiver is given in Eq. 2.3 where  $PR_u^i(\text{measured})$  is the measured pseudorange with respect to satellite  $i$ ,  $C_u$  is the receiver clock offset calculated by multiplication of clock bias with the speed of light.

$$PR_u^i(\text{measured}) = R_i + r_i + C_u \quad (2.3)$$

In the system demonstrated in Figure 2.5, the repeater locations are known and can be denoted by  $X_r$ ,  $Y_r$ , and  $Z_r$ . The distance between the satellite  $i$  and the repeater  $r$  is denoted with  $R_i$  which can be calculated as given in Eq. 2.4.

$$R_i = \sqrt{(X^i - X_r)^2 + (Y^i - Y_r)^2 + (Z^i - Z_r)^2} \quad (2.4)$$

The distance between a repeater and the receiver can be calculated by subtracting the range between the satellite and the repeater from the measured pseudorange. Then, the distance between receiver and repeater with clock bias is left as shown in Eq. 2.5 where  $p_i$  is found by subtracting the range between the satellite and the repeater from the measured pseudorange;  $r_i$  is the distance between receiver and repeater  $i$ ;  $C_u$  is the clock offset.

$$p_i = r_i + C_u \quad (2.5)$$

The correct position can be found when  $C_u$  is eliminated from the triangulation of every receiver.

In order not to send the same satellite signals from two or more repeaters, the directional antennas [75] must be deployed as outdoor GPS antennas. In the previous studies, the amplification and repetition of these signals take place in GPS frequency. However, the use of GNSS repeaters is restricted to prevent repeaters from interfering with other uses of GNSS in the vicinity. The Electronic Communications Committee's (ECC) Reports 129 and 145, and European Telecommunication Standards Institute's (ETSI) standard EN 302 645 prohibit the overall amplification of GNSS signals more than 45 dB, and the antenna gain exceeding 3 dB as it otherwise would affect nearby systems using GNSS services such as aeronautical radio navigation system DME, military and civilian radars, Earth Exploration Satellite Service, and so on [76], [77], [78]. The US policy "Manual of Regulations and Procedures for Federal Radio Frequency Management" presents under section 8.3.28 that GPS repeaters may be used only by the departments of the US Federal

Government or those who will deploy the system within a shielded indoor environment or have a license under FCC [30].

The legal restrictions on the power level reduce the success of the GPS repeater systems for indoor applications as the coverage is restricted. In order to circumvent the limitations, the present system in this thesis operates in the license-free 433 MHz ISM band. The allowable power level in 433 MHz ISM band is 10 dBm, which is 87 dB higher than the GPS allowed power level. Moreover, the free space path loss in 433 MHz is 11 dB less compared to GPS 1575.42 MHz signal. Another advantage of 433 MHz ISM when compared to 1575.42 MHz GPS frequency is that the signal can penetrate walls and buildings further due to larger wavelength operation. This also increases the coverage of the indoor area with the 433 MHz signals. A further advantage to design a system in 433 MHz ISM frequency is that the signals radiated at 433 MHz indoors will not interfere with outdoor GNSS signals.

For this reason, the outdoor directional GPS antenna is connected to a novel repeater structure, which down-converts GPS signals at 1575.42 MHz to 433 MHz, then amplifies in 433 MHz ISM band. The receiver front amplifies and up-converts the 433 MHz signals back to 1575.42 GPS frequency to process by an off-the-shelf receiver.

Lastly MATLAB® is used to implement and run the positioning algorithms.

## **CHAPTER 3 REPEATER HARDWARE OF THE INDOOR POSITIONING SYSTEM**

The proposed indoor positioning system comprises at least three repeaters and a receiver. In this chapter, the repeater hardware is explained in detail. The repeater consists of three main building blocks that the GPS signal passes through and two additional blocks that support the main blocks by controlling the operation of these building blocks. Following is the four main building blocks of the repeater hardware:

- Directional outdoor GPS antenna,
- Down-converter,
- Signal power conditioner and filter, and
- 433 MHz indoor antenna

In addition to these three blocks; the voltage regulator block and programmer/controller over Wi-Fi block serve as the supporting blocks. The latter block is used in the receiver hardware as well without any modification. The voltage regulator block is responsible for providing required current and voltages to the main building blocks while the controller and programmer block is responsible to adjust attenuation level for signal power conditioning and setting the down-converter register sets over Wi-Fi. Repeater hardware is demonstrated with building blocks in Figure 3.1.

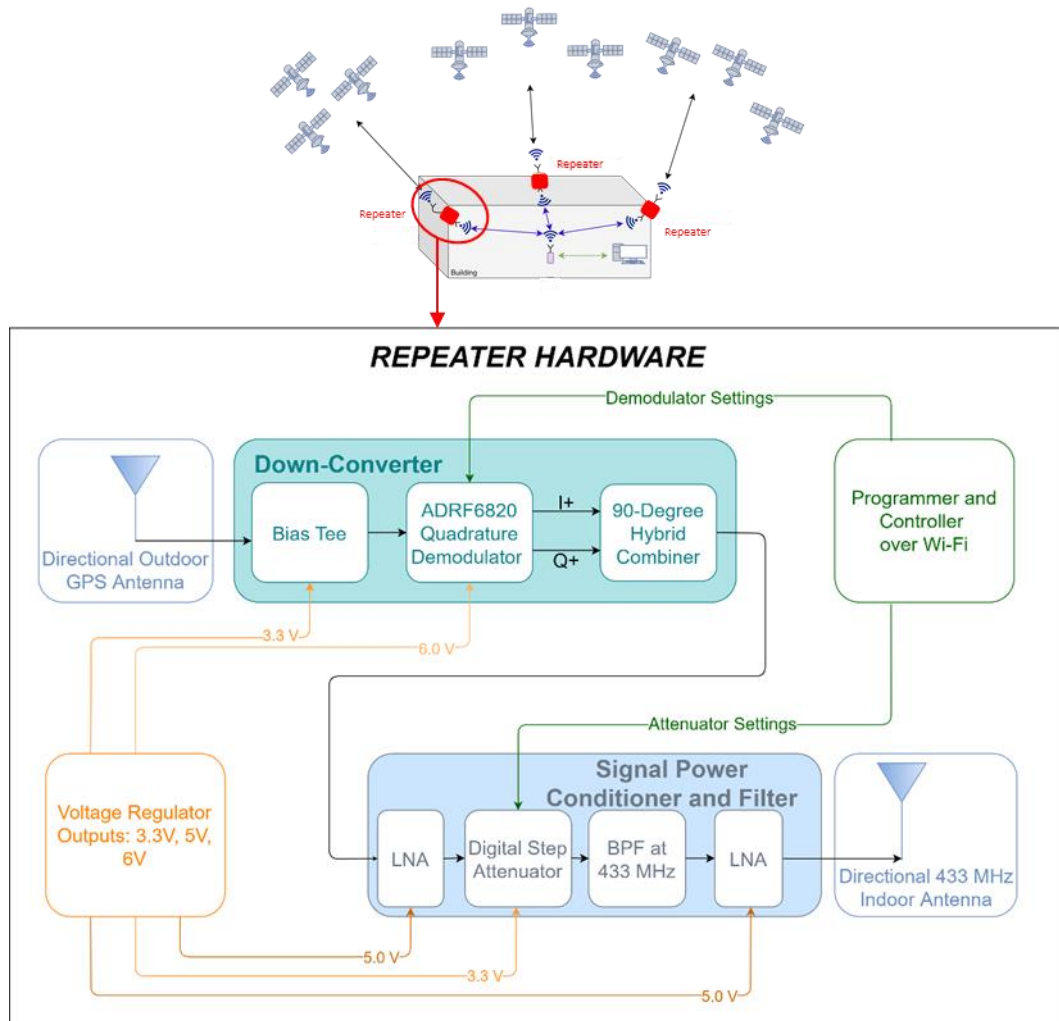


Figure 3.1 Repeater hardware and its building blocks

The active GPS antennas located outside the building picks up the GPS signals at 1575.42 MHz. The down-converter down-converts the signals at 1575.42 MHz to 433 MHz. The logic behind such an operation is to circumvent the legal restrictions on the GPS repeaters in 1575.42 MHz frequency, thus, to be able to increase the coverage due to higher allowable power level and less path loss in the 433 MHz ISM band. The amplifiers in the signal power conditioner and filter block amplify the signal, and whenever it is necessary, the amplification level is reduced by the digital step attenuator up to 31.5 dB. Hence, the gain of the overall system may be set to different values. The down-converted signal is also filtered at a band-pass filter at 433 MHz frequency before another amplification and indoor transmission. The directional 433 MHz antenna at each repeater, transmits the

down-converted GPS signal indoors. An overview of modules in repeater hardware is provided in Table 3.1.

Table 3.1 Overview of Repeater Hardware Modules

Block	Operation	Properties
<b>Directional Outdoor GPS Antenna</b>	Receives GPS signals coming from satellites at 1575.42 MHz	<ul style="list-style-type: none"> <li>• Tango 20 off-the-shelf active GPS antenna is used</li> <li>• The conic floating reflector is integrated to narrow the beamwidth and increase the directivity and gain</li> <li>• The total measured gain is 34.45 dBi</li> <li>• Beamwidth of 60 degrees</li> <li>• 3.3 V DC supply voltage over bias tee</li> </ul>
<b>Down-Converter</b>	Down-converts GPS signals from 1575.42 MHz to 433 MHz	<ul style="list-style-type: none"> <li>• Bias tee TB-JEBT-4R2GW+ is used to supply DC to directional active GPS outdoor antenna</li> <li>• ADRF6820 quadrature demodulator is used to down-convert GPS signals to 433 MHz <ul style="list-style-type: none"> <li>○ ADRF6820 is programmed over SPI from Programmer/Controller block</li> <li>○ ADRF6820 register sets and hardware is optimized for 1575.42 MHz to 433 MHz down-conversion and less loss</li> </ul> </li> <li>• 90-Degree power combiner ZX10Q-2-5-S is used to combine down-converter I+ and Q+ outputs</li> <li>• The total loss caused by ADRF6820 board, down-conversion, and insertion losses due to cables and 90-degree combiner is measured as 8.7 dB</li> </ul>
<b>Signal Power Conditioner and Filter</b>	Amplifies down-converted GPS signal by 11.7 dB to 43.2 dB and filters at 433 MHz	<ul style="list-style-type: none"> <li>• Cascaded topology of <ul style="list-style-type: none"> <li>○ Low Noise Amplifier LHA-13LN+</li> <li>○ Digital Step Attenuator DAT-31R5A-SP+</li> <li>○ Band Pass Filter DBP.433.T.A.30 at 433 MHz,</li> <li>○ Another Low Noise Amplifier LHA-13LN+</li> </ul> </li> <li>• LNA gain is measured as 22.43 dB <ul style="list-style-type: none"> <li>○ LNA noise figure is 0.9 dB,</li> <li>○ LNA IP3 is 38.3 dB</li> </ul> </li> </ul>

- Digital Step Attenuator is variable.
  - Attenuation can vary from 0 to 31.5 dB by 0.5 dB step size
  - The attenuator is programmed over SPI from the Controller/Programmer block.
  - Attenuation may be changed to prevent the near-far effect.
- Band pass filter has 19 MHz measured bandwidth from 426 to 445 MHz. The insertion loss of BPF is
  - -1.7 dB at 433 MHz,
  - -1.9 dB at 431 MHz,
  - -1.63 MHz at 435 MHz.

**433 MHz Indoor Antenna** Transmits down-converted GPS signals to indoors

- Directional antenna can be used.
  - Antenna size is 15.35 cm x 16 cm
  - The patch size is 12.3 cm x 13 cm
  - $S_{11} = -11.42$  dB @433 MHz
  - Simulated gain is 1.5 dBi
  - The substrate is formed by two 1.28-mm thick RO3010 substrates piled up with an air gap of 3 mm in between
- or Dipole antenna in Appendix C can be used.

The proposed hardware that is explained in detail in the following sections is demonstrated with all the modules but 433 MHz indoor antenna is demonstrated in Figure 3.2.

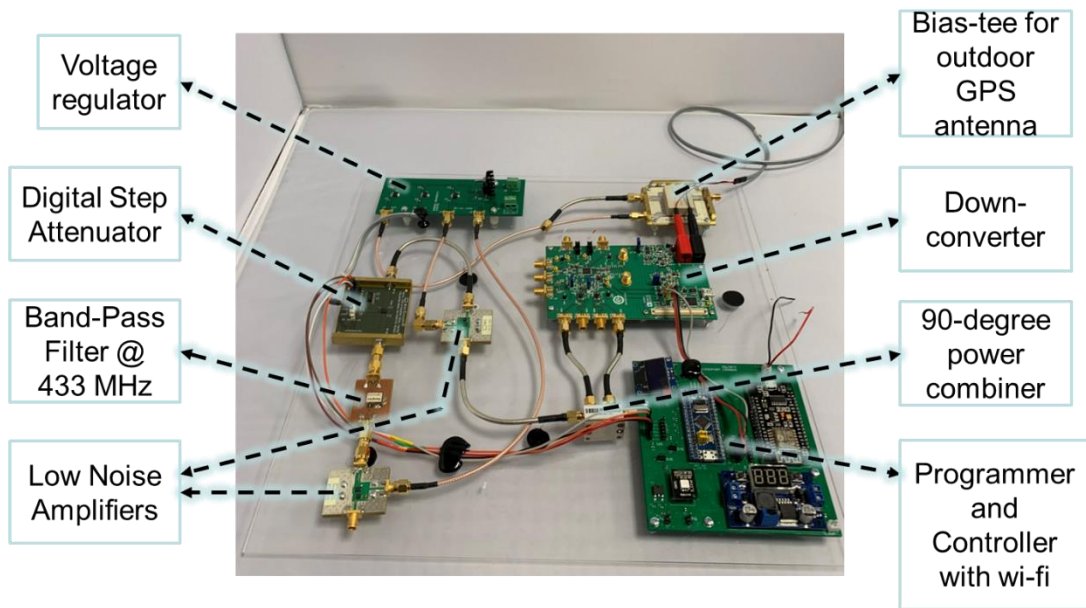


Figure 3.2 Repeater hardware excluding the 433 MHz directional antenna

In the following sections, the design of the directional outdoor GPS antenna and its measurements, the design of the down-converter and its measurements, the design of the signal power conditioning and filtering block and its measurements are analyzed in detail. The designs of the voltage regulator for repeater hardware is described in detail. The programmer/controller over the Wi-Fi block is designed such that it operates in both repeater and receiver hardware. For this reason, a detailed explanation of the programmer/controller block is presented under Chapter 4.

### 3.1 Directional Outdoor GPS Antenna

The directional outdoor GPS antenna is the first block of the repeater hardware. Such antenna was proposed by Özsoy et al. in their work titled “Directional GPS Antenna for Indoor Positioning Application” [75]. The directional outdoor GPS antenna addresses the issue of GPS satellite selection by the increased directivity and narrowed beamwidth of

the outdoor antenna. These properties of the antenna are achieved by placing a floating conic reflector structure around a customary active GPS antenna and integrating all these elements on a larger ground plane.

Off-the-shelf GPS active antenna has a beamwidth more approximately 90 degrees and a gain of 30 dBi. In order to reduce beamwidth and increase the directivity, the off-the-shelf antennas ground plane is extended by soldering it onto a larger ground plane. Then, a conic floating reflector structure is integrated. The designed active antenna with a floating reflector and larger ground plane has narrower beamwidth by 30 degrees and higher gain by 4.45 dBi than the off-the-shelf active GPS antenna. The total measured gain is 34.45 dBi while the beamwidth reduces to 60 degrees for the designed antenna. The design of the antenna and measurements are discussed in Sections 3.1.1 and 3.1.2.

### **3.1.1 Directional Antenna Design**

The directional outdoor GPS antenna consists of a customary active GPS antenna, a ground plane holding the active GPS antenna, and a floating reflector of a conic shape whose inner surface is aluminum while the outer surface is PLA.

To examine the effect of the floating reflector, a circularly polarized GPS patch antenna at 1575.42 MHz is modeled and simulated in HFSS. The antenna is modeled on a ceramic substrate with permittivity of 68. The dimensions of patch, substrate, reflector, and ground are provided in Figure 3.3.

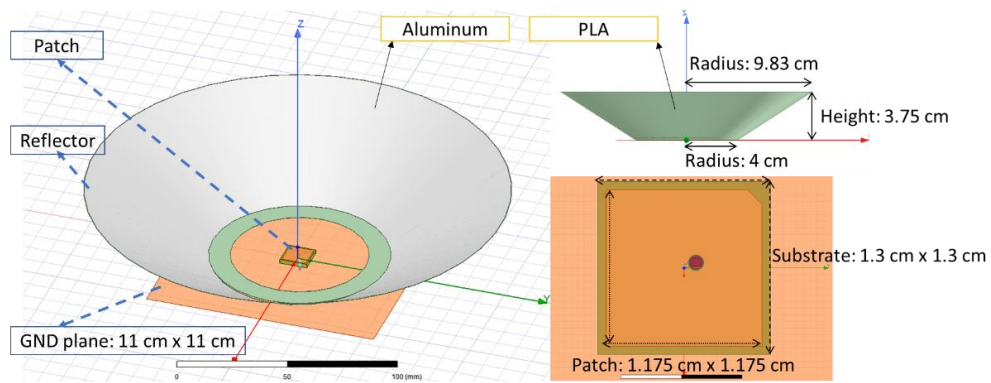


Figure 3.3 Antenna design in HFSS

The inner aluminum surface of the reflector does not contact the ground plane of the antenna in that the reflector floats. The simulation results suggest that the total directivity increases while the beamwidth decreases by placing a conic reflector of the given sizes and extending the ground plane Figure 3.4.

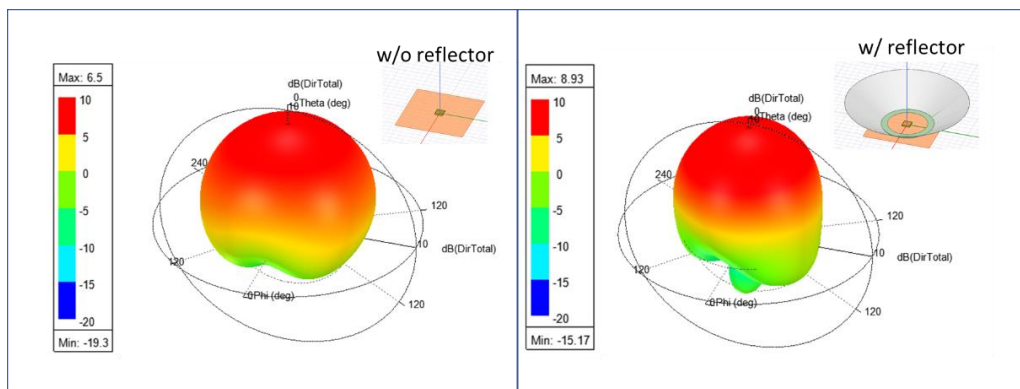


Figure 3.4 Total directivity with and without the conic reflector

The total directivity increases by 2.43 dB when the suggested floating reflector placed around the GPS antenna located at the center. The total directivity is 6.5 dB without the cone and 8.93 dB with the cone.

Further simulation results are presented in Figure 3.5. The 3 dB beamwidth of the patch antenna decreases by 30 degrees when the suggested floating reflector placed around the GPS antenna located at the center. The beamwidth is 98 degrees without the cone and 68 degrees with the cone. The realized gain increases by 1.22 dB with the integration of the conic reflector.

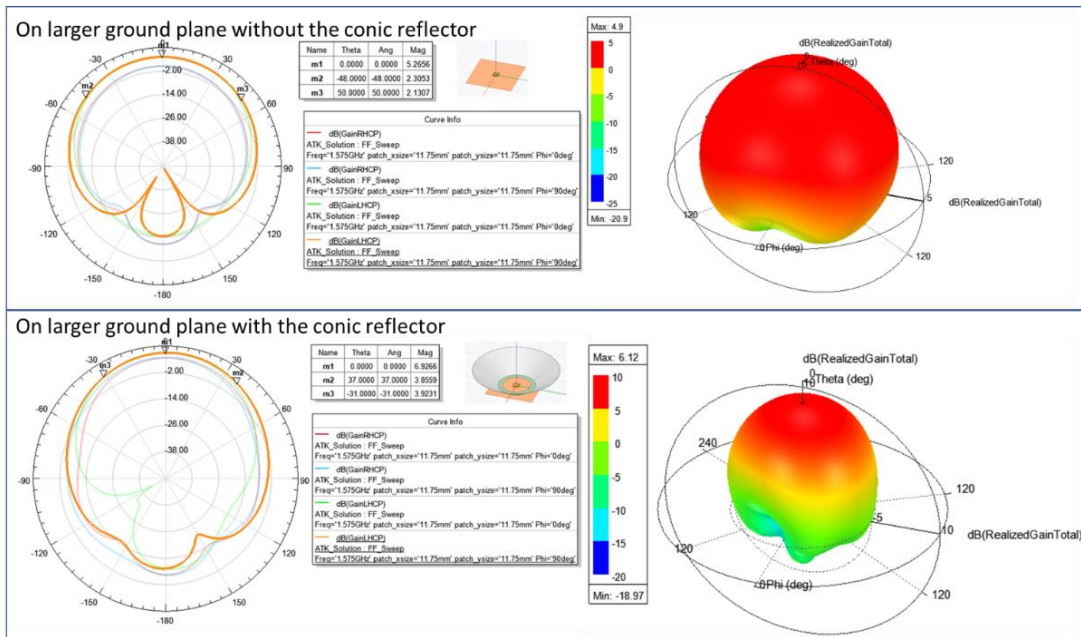


Figure 3.5 2D Polar gain and total realized gain plots with and without the conic reflector

The customary active antenna is the product of TANGO20/3M/SMAM/S/S/26 of Siretta Ltd shown in Figure 3.6. This antenna operates at 1575.42 MHz frequency. The antenna requires 2.2-5 V DC. The reported antenna gain is 28 dBi while the noise figure is less than 1.5. dB [79]. Further details of the active antenna are provided in Table 3.2.

Table 3.2 Off-the-shelf GPS Active Antenna Specifications [79]

Antenna Parameter	Value
Gain	30 dBi
Noise Figure	<1.5 dB
Ex-band Attenuation	12 dB@CF+50MHz, 16 dB@CF-50 MHz
Supply Voltage	2.2-5 V DC
Current Consumption	5-15 mA
VSWR	<2.0



Figure 3.6 Active GPS antenna

Tango 20 antenna's plastic box was removed and then the active antenna was soldered onto the large ground plane of the sizes 11 cm x 11 cm as shown in Figure 3.7.

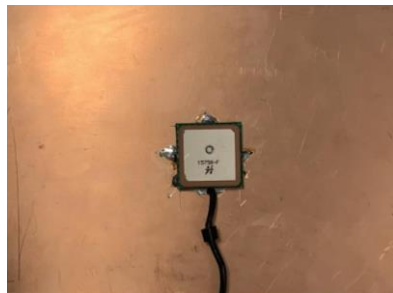


Figure 3.7 Active antenna on the large ground plane

Finally, taking the antenna as the center, the conic reflector is integrated around the antenna to form the directional active GPS antenna depicted in Figure 3.8.



Figure 3.8 Directional outdoor GPS active antenna

### 3.1.2 Directional Antenna Measurement Results

Completing the design and fabrication of the conic reflector with 3D printing technology, the reflector is integrated into the active antenna located on the 11 cm x 11 cm ground plane. The measurements are done in the semi-anechoic chamber shown in Figure 3.9.

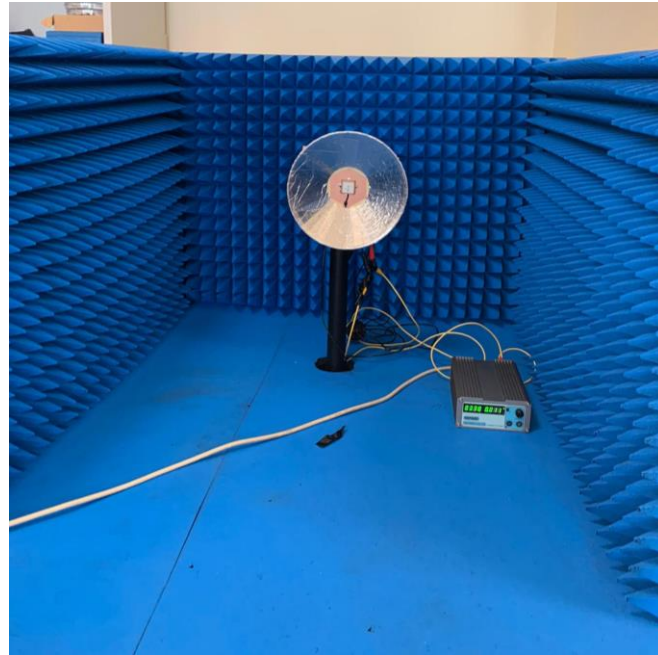


Figure 3.9 Directional antenna and the semi-anechoic chamber

Double Ridge Guide Horn Antenna SAS-571 is placed 2.20 m away from the antenna under measurement. The input power to the horn antenna is -25 dBm at 1575.42 MHz. The path loss for 1575.42 MHz in 2.20 meters is 43.2 dB. The horn antenna is reported to have 10 dBi gain [80].

The measured values and calculated gain values for the Tango 20 antenna, Tango 20 antenna with and without the conic reflector are provided in Table 3.3.

Table 3.3 Received Power and Calculated Gain of GPS Active Antenna

	Tango 20 <sup>[79]</sup>	Large GND	Large GND Plane
		w/o Conic Reflector	w/ Conic Reflector
<b>Maximum Power Received</b>	-28.2 dBm	-25.33 dBm	-23.75 dBm
<b>Calculated Gain</b>	30 dBi	32.87 dBi	34.45 dBi

Simulation results suggest that the gain increases by 1.22 dB as mentioned previously. The calculated gain with and without the conic reflector according to the measurements differs by 1.58 dB.

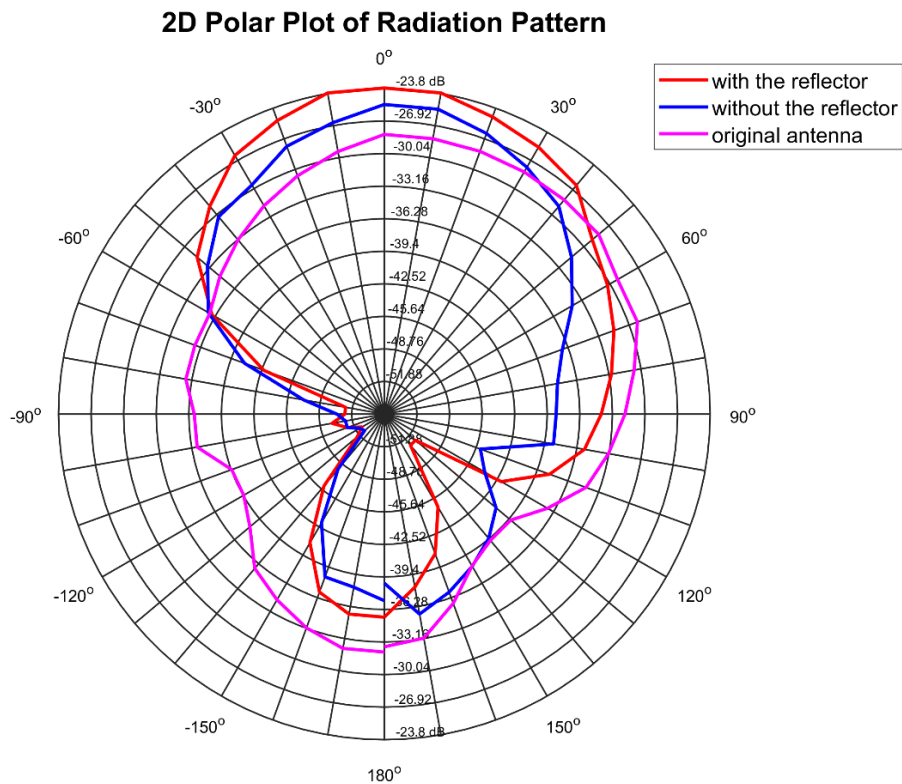


Figure 3.10 Measured 2D Patterns with and without the reflector, and the original antenna

The measurement results suggest that the gain increases with the larger ground plane on the back and the conic reflector by 4.45 dB compared to the values provided in the

datasheet and measured. Moreover, the fabricated antenna is directly connected to the ground plane while the off-the-shelf antenna lies tilted in a plastic box that surrounds the patch and substrate.

The beamwidth of the Tango 20 antenna used is 90 degrees according to the datasheet of the product and measurements done with the off-the-shelf antenna [79]. The extended ground plane and the cone reduces the beamwidth to 60 degrees.

### **3.2 Down-converter**

The down-converter block is the second part of the repeater hardware and follows the active GPS outdoor antenna. The RF signals at 1575.42 MHz is down-converted to 433 MHz in this block. This block consists of 3 modules listed as follows:

- Bias Tee
- ADRF6820 Quadrature Demodulator
- 90-Degree Hybrid Power Combiner

These modules in the block are depicted in Figure 3.11. The first module is a bias tee that provides required DC to the active antenna in the first block. The GPS signals pass through the bias tee, then downconverted to 433 MHz by ADRF6820 quadrature demodulator. This module can be programmed via a computer or the programmer/controller block. Since the outputs of ADRF6820 is designed as I/Q outputs, a 90-degree hybrid combiner is deployed as the last module to combine the signals with a 90-degree phase difference.

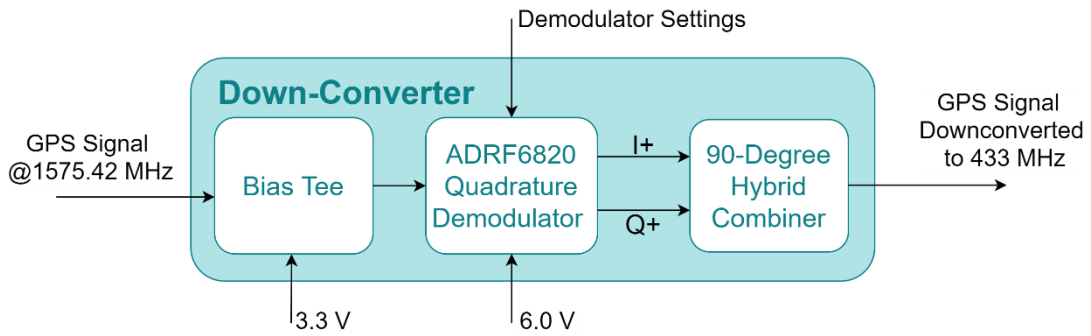


Figure 3.11 Modules in the down-converter block

Section 3.2.1 describes briefly the modules in the down-converter block and presents how they are brought together to build the block. Following the brief description of the down-converter design in section 3.2.1, section 3.2.2 elaborates on the optimizations in the register sets of ADRF6820 and modifications carried out in ADRF6820 quadrature demodulator from the hardware point of view for this study.

Section 3.2.3 presents the overall performance of the block after modifications and optimizations and explains the measured loss of the down-converter block, excluding the bias tee. The measured loss of the down-converter block is found as 8.7 dB under section 3.2.3.

### 3.2.1 Down-converter Modules and Design

As mentioned previously down-converter consists of a bias tee, ADRF6820 quadrature demodulator, and a 90-degree hybrid power combiner. These modules are shown in Figure 3.12.

TB-JEBT-4R2GW+ of Mini-Circuits is opted out as the bias tee module in the down-converter block. This evaluation board has 3 ports: RF, DC, RF&DC (Figure 3.12a). The RF&DC port is connected to the outdoor active GPS antenna, while the DC port is

connected to the voltage regulator block in order to provide 3.3 V DC to the active outdoor GPS antenna. RF port of the bias tee is connected to the ADRF6820 quadrature demodulator board.

The bias tee is followed by the ADRF6820-EVALZ evaluation board (Figure 3.12). ADRF6820-EVALZ is used to down-convert the GPS signals to 433 MHz. The I+ and Q+ outputs of ADRF6820-EVALZ have a 90-degree phase difference.

ADRF6820-EVALZ evaluation board meets the DC voltage requirement of 6 V from the voltage regulator block. This board can be programmed via a computer or the programmer/controller that is connected to the serial ports. ZX10Q-2-5-S 90-degree hybrid coupler from Mini-Circuits is connected to the I+ and Q+ output channels to combine these signals. The hybrid coupler is shown in Figure 3.12c.

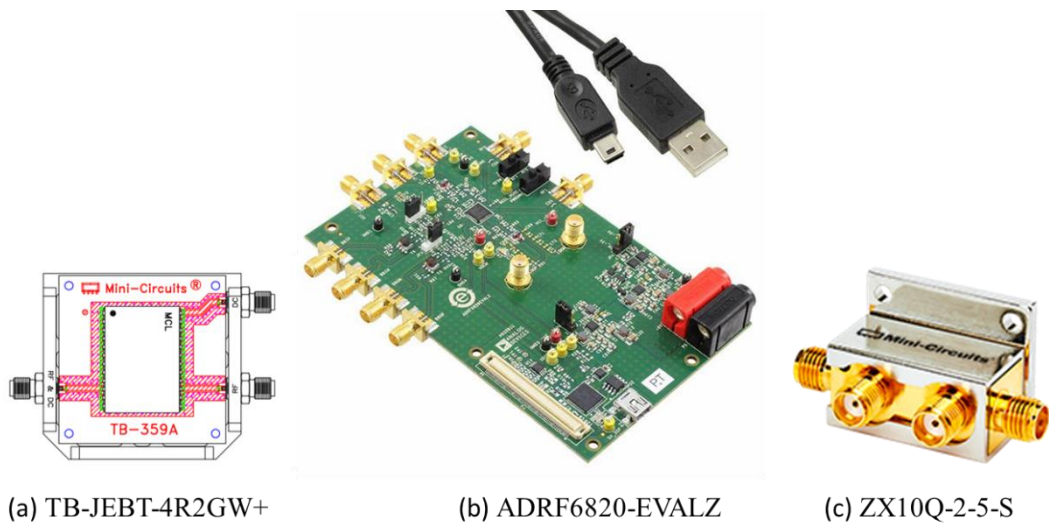


Figure 3.12 Modules used in the down-converter block

These three modules down-converts the GPS signal to 433 MHz and deliver to the 433 MHz directional indoor antenna. Down-Converter modules are shown together in Figure 3.13.

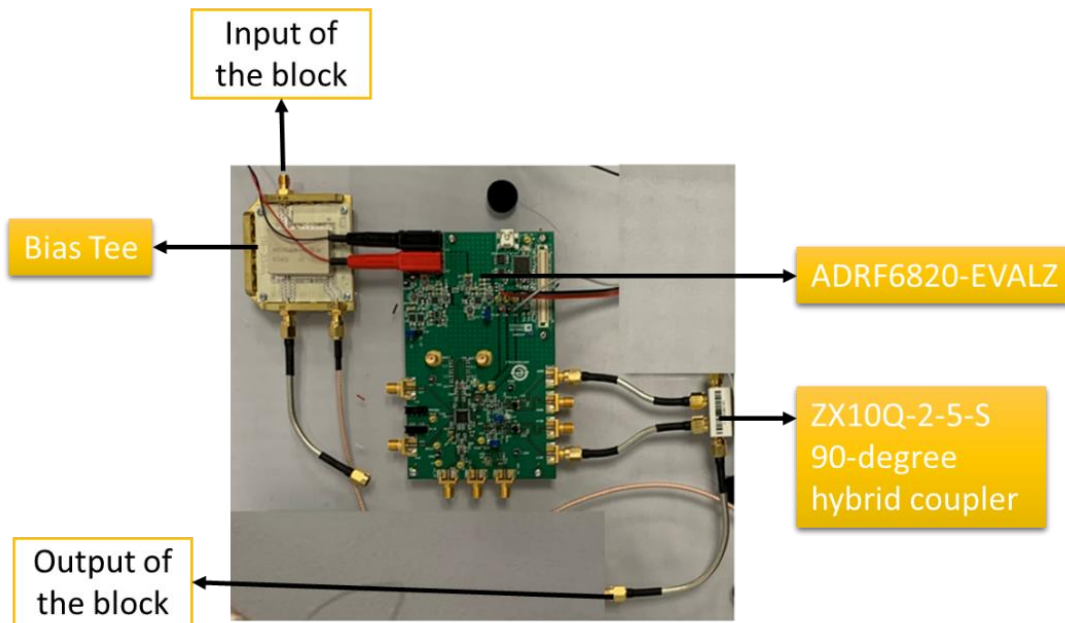


Figure 3.13 Down-converter block formed with the modules presented

### 3.2.2 Down-Converter Optimization, Simulations and Measurements

This section presents the details of the hardware modifications of the ADRF6820-EVALZ board and its programming details to optimize the down-converter performance for 1575.42 MHz to 433 MHz down-conversion. The measurements at the input of ADRF6820-EVALZ and the output of 90-degree hybrid combiner are measured to calculate the total loss due to down-conversion loss, board loss, and cable loss. Each output of ADRF6820-EVALZ is connected to a 90-degree hybrid coupler with a 3-inch cable from Crystek Corporation product number CCSMA18-MM-141-3.

### 3.2.2.1 ADRF6820-EVALZ Hardware Optimizations, Simulations and Measurements

ADRF6820-EVALZ is reported having more than 17 dB loss due to board loss and the L-section matching network at the outputs for matching [82]. The board has undergone several important changes in order to reduce the loss. The main changes made to the hardware of the evaluation board are as follows:

- An oscillator at 38.4 MHz frequency has been added
- L-section matching network has been bypassed by replacing TC1-1-13M+ 1:1 transformers with TC4-1WX+ 4:1 transformers

The first modification of integrating an oscillator that oscillates at 34.8 MHz is necessary to generate the local oscillator (LO) input signal internally. Fractional-N synthesizer on the chip generates the LO signal. The oscillator is required for the reference PLL input. ADRF6820-EVALZ is capable of dividing and multiplying the PLL reference input signal to get the required signal frequency to deliver to the phase frequency detector (PFD). Because of these reasons, IQD Frequency Products' oscillator with the product number of LFTCXO070898REEL has been integrated into the Y2 region on the board.

The second modification is done to reduce the loss caused by the L-section matching network at I/Q outputs. I/Q outputs are terminated with 200-ohm impedance. The L-section matching exists to match the impedance to 50 ohms from 200 ohms as shown in Figure 3.14. However, L-section matching is a lossy method.

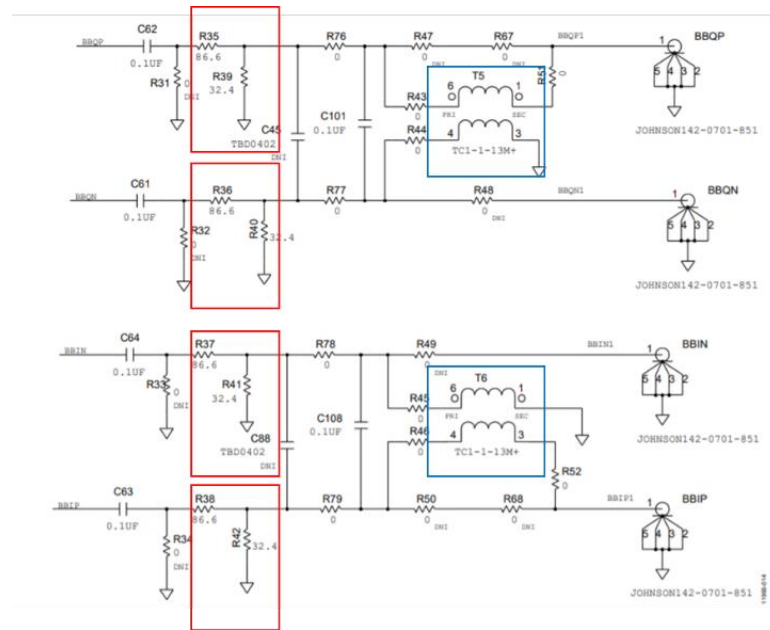


Figure 3.14 L-section matching network and 1:1 transformers

Firstly, the signal loss is simulated and then board loss measured. The signal loss caused by L-section matching on the ADRF6820-EVALZ is simulated using Advanced Design System (ADS) software presented in Figure 3.15.

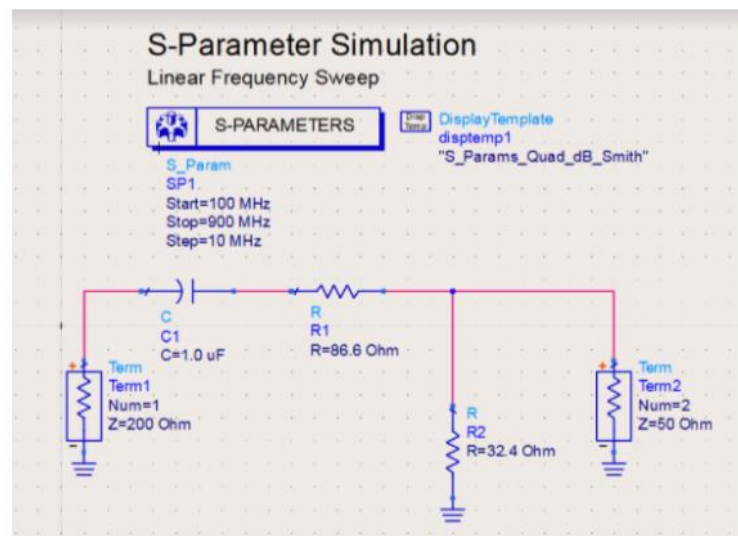


Figure 3.15 L-section matching and ADS S-parameter Simulation

The S-Parameter simulation result shows that the insertion loss of the L-section matching network is 11.8 dB at 433 MHz (Figure 3.16).

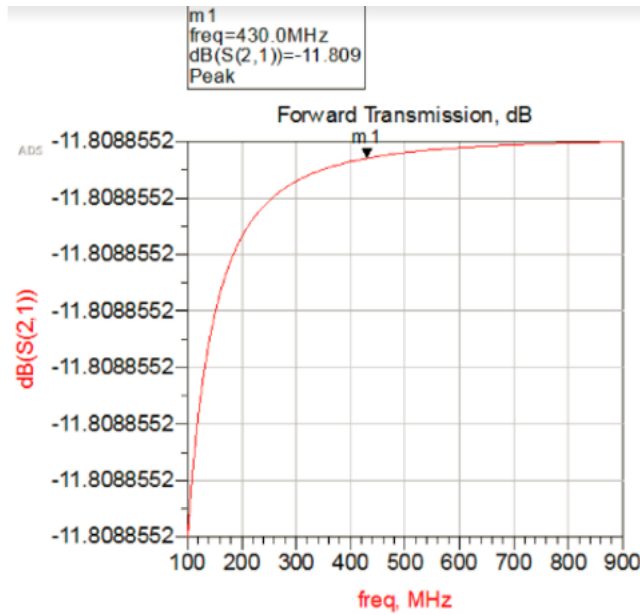


Figure 3.16 Insertion Loss of L-section matching network

Secondly, the overall loss of ADRF6820-EVALZ board (down-conversion, insertion losses from components and board loss) with the L-section matching network and 1:1 transformers at the output is measured. -30 dBm RF signal at 1575.42 MHz is provided from Agilent E4437B ESG-DP Serial RF Signal Generator at the board input. The signal power at the output is measured with Agilent E4407B ESA-E Spectrum Analyzer. The measurement setup is depicted in Figure 3.17.



Figure 3.17 ADRF6820-EVALZ loss measurement setup

The signal levels at I+ and Q+ are -50.32 dBm and -50.73 dBm, respectively Figure 3.18.

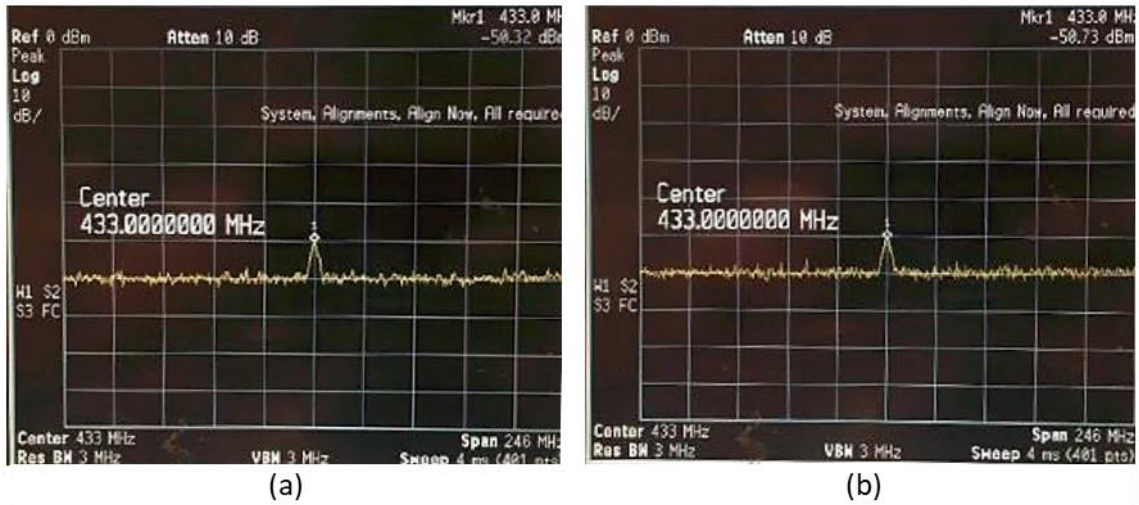


Figure 3.18 Power level at the outputs of I+ and Q+ channels, respectively in (a) and (b)

I+ is connected to PORT 1 (+90°) while the Q+ output is connected to PORT 2 (0°) of the 90-degree hybrid combiner to be summed up. The summation of two outputs results in -47.36 dBm signal power which is 3 dB greater than both outputs as expected (Figure 3.19).

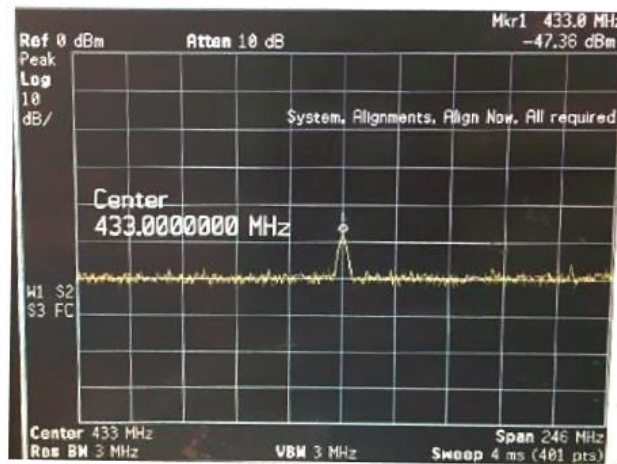


Figure 3.19 Power level at the output of the 90-degree hybrid combiner

These measurements conclude that the overall board loss is 17.36 dBm if 1:1 transformers and L-section matching network is kept. It is necessary to replace 1:1 transformers at T5

and T6 locations with 4:1 transformers and by-pass the L-section matching network which would no longer be necessary when the existing transformers are replaced.

The L-section matching network at each output is by-passed with the following arrangements:

- R35, R36, R37, and R38 resistors are replaced with 0-ohm resistors.
- R31, R32, R33, R34, R39, R40, R41, and R42 resistors are not inserted.

Thirdly, the measurements are repeated for the hardware with 4:1 transformers and by-passed L-matching network (Figure 3.20). When the signal power at the input of ADRF6820-EVALZ is -7.3 dBm at 1575.42 MHz, the measured signal power at the output of the 90-degree hybrid combiner is -14.18 dBm at 433 MHz (Figure 3.21).

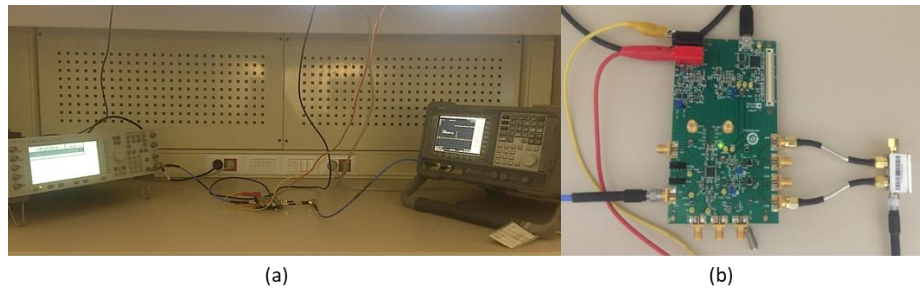


Figure 3.20 Measurement setup in (a) and the modified ADRF6820 combined with the 90-degree power combiner in (b)

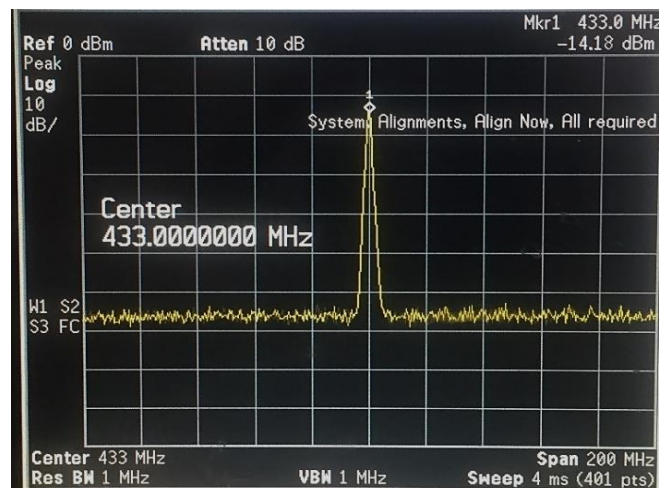


Figure 3.21 Signal power at the output for the fully modified ADRF6820-EVALZ combined with the 90-degree power combiner

The removal of the L-section network has improved the circuit performance by reducing the total loss of down-converter block by 11 dB. This result is in accordance with the simulated S-parameters for the L-section matching network.

### **3.2.2.2 Setting ADRF6820-EVALZ Register Sets for the Optimized Performance for the Said Frequency Down-Conversion**

The ADRF6820-EVALZ evaluation board has been programmed via Customer Evaluation Rev 0.0.0 software and the final register sets that optimize the performance of the circuit for down-conversion from 1575.42 GPS frequency to 433 MHz is obtained. The values shown in Figure 3.22 optimizes the performance of the system. Each value seen on the programming interface corresponds to some bits in the register sets which can be seen in the datasheet of ADRF6820 in [83]. Then, these register sets are recorded and loaded into the ADRF6820 chip via a serial interface.

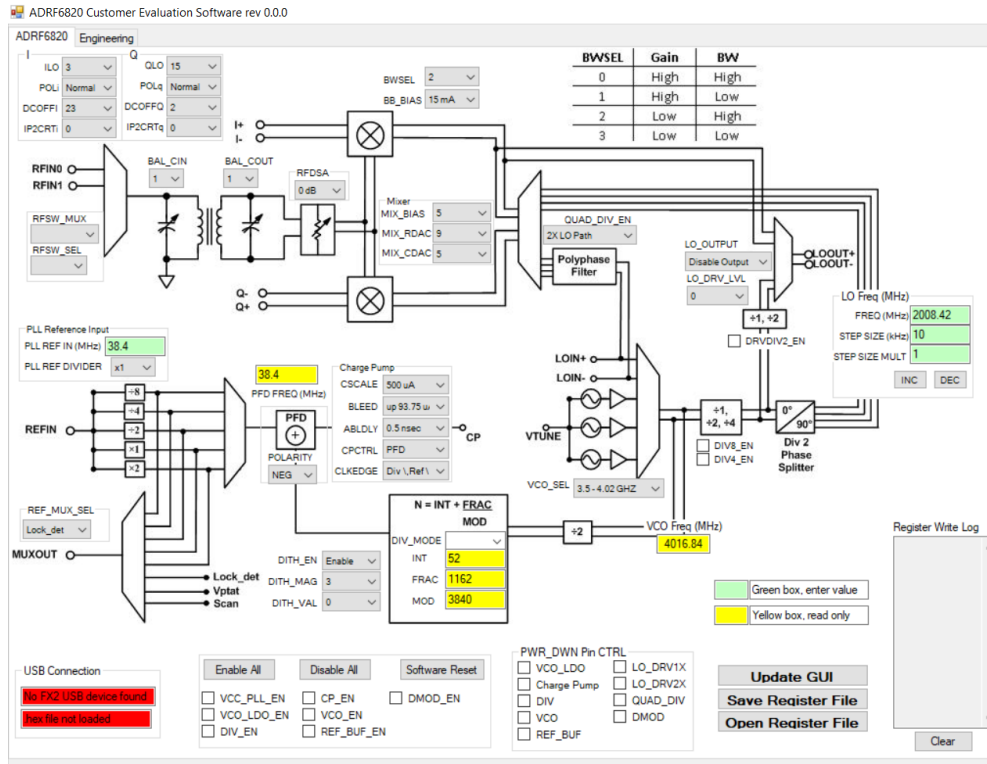


Figure 3.22 ADRF6820 Customer Evaluation Software Interface and The Optimized Values

The following part of this section elaborates on and ADRF6820 quadrature demodulator chip and the logic behind obtaining these values. Some aspects of ADRF6820 that result in the values presented in Figure 3.22 are explained below.

1. The local oscillator frequency is set to 2008.42 MHz ( $f_{LO}=2008.42$  MHz) in that mixing GPS signal ( $f_{GPS}=1575.42$  MHz) and LO results in down-conversion of GPS signal to 433 MHz ( $f_{LO}- f_{GPS}=433$  MHz). Since LO frequency is higher than the RF signal, it is called high-side LO injection. In the case of high-side LO injection, Q channel leads I channel by 90 degrees at ADRF6820 outputs [83] as depicted in Figure 3.23.

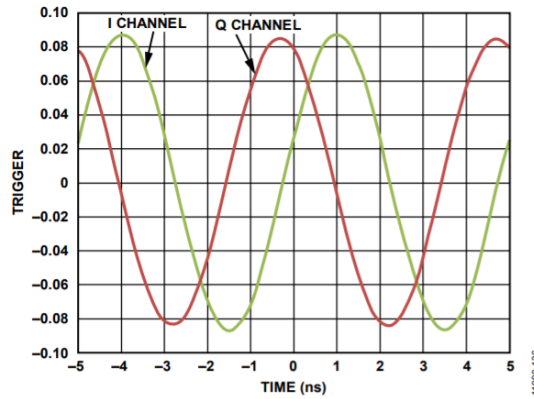


Figure 3.23 Q channel leading I channel by 90 degrees if  $f_{LO} > f_{GPS}$  [83]

The high-side LO injection and Q leading I channel implies that  $POL_I=1$  and  $POL_Q=2$  which characterizes the polarities of I and Q channels as “normal” [83]. In line with this information,  $POL_I$  and  $POL_Q$  values are entered as "normal" in the programming interface. This also explains why  $I_+$  is connected to PORT 1 ( $+90^\circ$ ) while the  $Q_+$  output is connected to PORT 2 ( $0^\circ$ ) of the 90-degree hybrid combiner. In this way, the phase difference between I/Q channels is compensated for summation.

2.  $BAL\_CIN$ ,  $BAL\_COUT$ ,  $MIX\_BIAS$ ,  $DEMOD\_RDAC$ , and  $DEMOD\_CDAC$  values for ADRF6820 are set according to the suggested values for the RF input frequency of 1575.42 MHz [83]. Selected values are demonstrated in Figure 3.24. However,  $MIX\_BIAS$  and  $MIX\_RDAC$  values are changed with respectively, 5 and 9 as these values are observed to improve the performance at 1575.42.

BWSEL	f <sub>RF</sub> (MHz)	BAL_CIN	BAL_COUT	MIX_BIAS	DEMOD_RDAC	DEMOD_CDAC
2	500	7	7	3	5	7
2	600	7	7	3	5	7
2	700	7	7	2	4	9
2	800	7	3	3	8	4
2	900	6	2	3	9	5
2	1000	5	1	3	7	7
2	1100	3	2	2	6	9
2	1200	3	1	2	8	9
2	1300	2	1	2	3	9
2	1400	2	1	3	8	5
2	1500	1	1	3	8	6
2	1600	1	1	2	8	5
2	1700	1	0	2	8	5
2	1800	1	1	2	8	7
2	1900	1	0	2	5	6
2	2000	1	0	3	5	7
2	2100	1	0	2	4	6
2	2200	1	0	2	4	6
2	2300	1	0	3	8	6
2	2400	1	0	3	8	6
2	2500	1	0	3	9	6
2	2600	1	0	3	9	6
2	2700	1	0	2	8	5
2	2800	1	0	2	8	5

Figure 3.24 Suggested BAL\_CIN, BAL\_COUT, MIX\_BIAS, DEMOD\_RDAC, and DEMOD\_CDAC values emphasized in red rectangle

3. While deciding BAL CIN-COUT values, the capacitance at the input and the output of balun, it is considered that higher frequency requires larger capacitance. For that reason, low BAL\_CIN and BAL\_COUT values are opted out for the 1575.42 MHz RF signal input. According to the graph presented in Figure 3.25, the highest gain (least loss from the ADRF6820-EVALZ evaluation board) may be obtained by defining both BAL\_CIN and BAL\_COUT codes as 1 in the program interface.

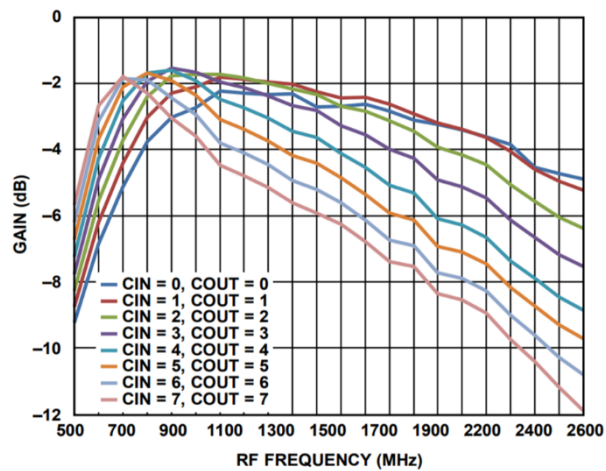


Figure 3.25 Gain vs Frequency of RF signal at the input of ADRF6820 for several BAL\_CIN and BAL\_COUT codes [83]

4. Finally, the image frequency rejection performance of the ADRF6820-EVALZ is improved by improving the phase error between I and Q channels [83]. By using

the plotted data for LO=1940 MHz frequency presented in Figure 3.26, the ILO and QLO values are set to 3 and 15, respectively. It is also considered that the hybrid coupler may cause a phase error of approximately 2.11 degrees at 433 MHz frequency according to the data provided in its datasheet.

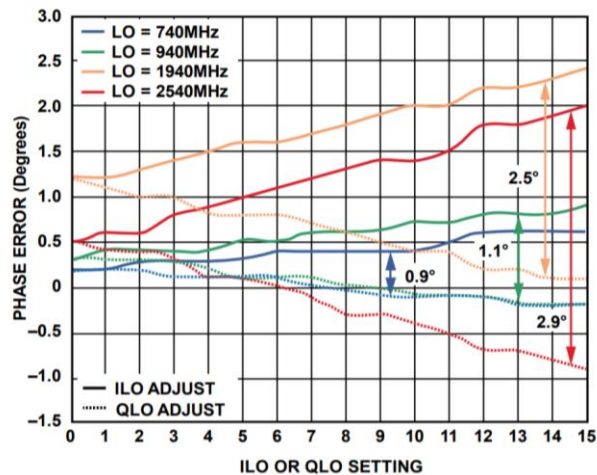


Figure 3.26 Setting ILO and QLO and for improved image rejection [83]

The image rejection performance of the ADRF6820-EVALZ board is measured. Rohde & Schwarz FSH8 Spectrum Analyzer and Agilent E4437B ESG-DP Serial RF Signal Generator are used in the measurements. LO frequency is set to 2008.42 MHz. The signal level for only one of the outputs of ADRF6820-EVALZ is measured at 433 MHz and 3583.84 MHz ( $f_{LO}+f_{GPS}$ ) to calculate image frequency rejection Figure 3.27.

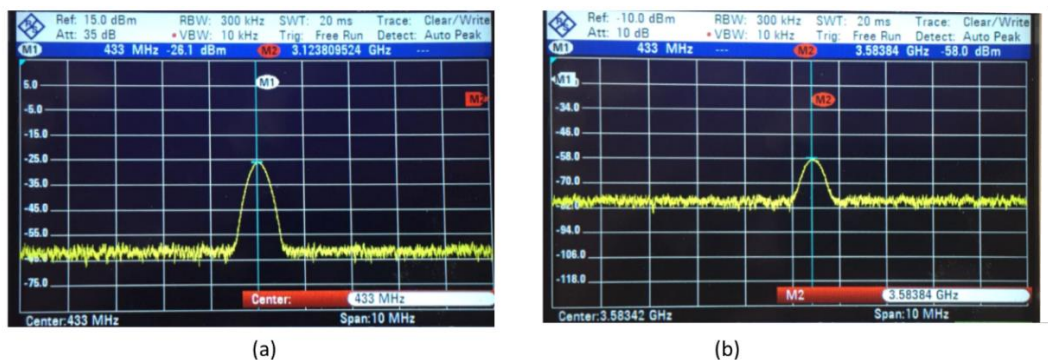


Figure 3.27 The power level of the signal formed at the frequency of 433 MHz and 3583.84, respectively in (a) and (b)

The power level of the signal formed at the frequency of 433 MHz is -26.1 dBm while it is -58.0 dBm at 3583.84 MHz. By subtracting these values, it is revealed that the high-frequency image is suppressed by 31.9 dB. This measurement does include the summation of I+ and Q+ signals. T

The signal level at the input of ADRF6820 is -15 dBm, and the signal level at the output port of the power combiner is -26.1 dBm. At this point, one should notice that the registers of the ADRF6820 chip are set as explained in this section for down-converting the GPS signal and preserving its fidelity. Although the ADRF6820 board can reach less loss, the register set is not optimized for the highest gain. The ADRF6820 hardware and register sets are optimized for the down-conversion GPS signal while preserving its fidelity with the minimum power loss.

Detailed measurement results for the whole down-converter block is presented under Section 3.2.3. Moreover, some of the parameters in the interface such as DCOFFI and DCOFFQ are found as a result of different experiments because the optimized values for these parameters do not exist in the ADRF6820 datasheet. However, the graphics and optimized values and explanations related to this family of chipsets and evaluation boards are given in more detail in the ADRF6720-27 datasheet. ADRF6720-27-EVALZ is deployed in the receiver hardware. Therefore, some of the parameters in the interface are found based on the data presented in [84]. This section is included when explaining the optimized values in the programming of ADRF6720-27-EVALZ in the next chapter.

### **3.2.3 Down-Converter Measurement Results**

After the optimization of hardware and register sets of ADRF6820-EVALZ for the down-conversion of the GPS signal, the down-converter block's gain is calculated through

power measurements at the output and input of the block, excluding the bias-tee in order not to harm measurement devices due to DC bias it provides to the device at the input of the block. Therefore, the measurement of this block is done excluding the bias tee, but combining the ADRF6820 evaluation board with the hybrid combiner as explained previously. Rohde & Schwarz FSH8 Spectrum Analyzer and Agilent E4437B ESG-DP Serial RF Signal Generator are used in the measurements.

The frequency down-converter ADRF6820-EVALZ at the input is fed with a sinusoidal signal at 1575.42 MHz from the RF signal generator at a power level of -21.6 dBm. The power level at the output of each I+ and Q+ channels is measured as -33.5 dBm individually (Figure 3.28).

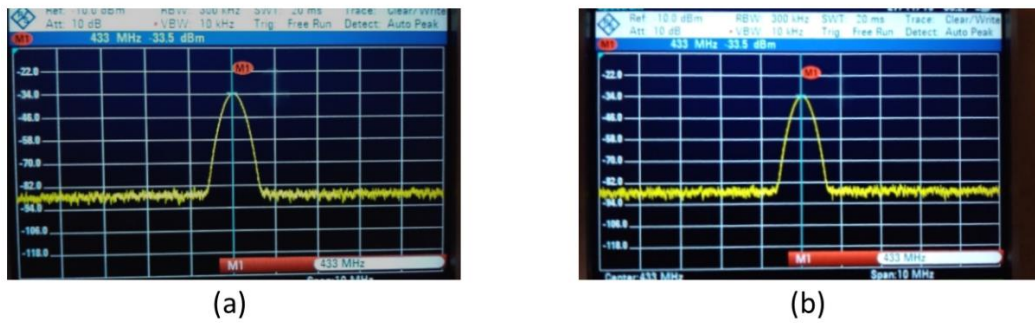


Figure 3.28 Signal levels at the output of I+ in (a) and Q+ in (b) after optimizations

Combining both channels with the hybrid combiner, the signal power measured as -30.4 dBm. This result is presented in Figure 3.29.

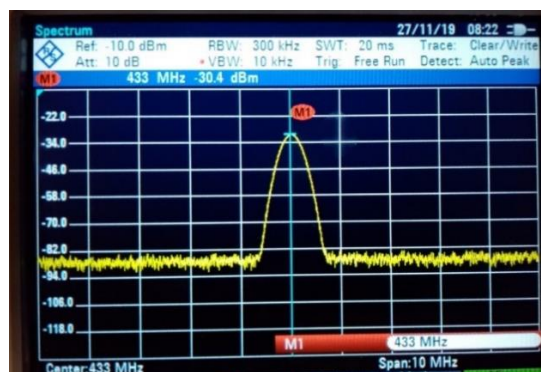


Figure 3.29 Signal level at the output of down-converter block after optimizations

The signal level at the sum port of the hybrid power combiner is measured as -30.4 dBm. The cable loss deployed at the output port is 0.1 dB. Therefore, the optimized down-converter block has a loss of 8.7 dB ( $30.4\text{dBm} - 0.1\text{dBm} - 21.6\text{dBm} = 8.7\text{ dB}$ ), excluding the bias tee.

### **3.3 Signal Power Conditioner and Filter**

The signal power conditioner and filter block is the third part of the repeater hardware and follows the down-converter. The input signal to this block is at 433 MHz. The RF signals at 433 MHz is amplified to the desired level by fixed-gain amplifiers and digitally controlled step attenuator modules in this block. By changing the attenuation level, the gain may be varied in this block to prevent the near-far effect. The near-far effect occurs as the difference between the powers of two GPS signals may be up to tens of decibels indoors [46]. This may cause lower GPS signals to be undetected. In order to prevent such problems, the gain of the repeaters is designed in a way that the gain can decrease by 31.5 dB due to the digital step attenuator in the signal power conditioner and filter block. If a GPS signal causes other signals not to be sensed by suppressing them due to high power differences, the gain is reduced with a digital step attenuator to prevent the near-far effect.

The modules in signal power conditioner and filter block are listed as follows:

- Low Noise Amplifier
- Digital Step Attenuator
- Band Pass Filter at 433 MHz
- Low Noise Amplifier

These modules in the block are depicted in Figure 3.30. The first module is an LNA that amplifies the RF signal received from the down-converter block. The first module is

followed by a digital step attenuator and a band pass filter at 433 MHz. At the output of the stage, another LNA is deployed.

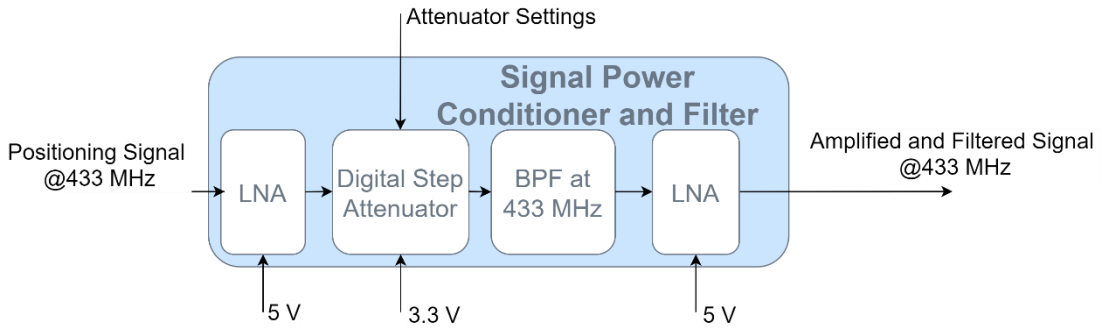


Figure 3.30 Modules in the signal power conditioner and filter block

This topology is selected considering the noise figure of the cascaded system for this block. The noise figure for a cascaded system is calculated from the Friis Formula in Eq.3.1 where  $n$  represents the last module and the number of modules in a cascaded system [85].

$$NF = F_1 + \frac{F_2 - 1}{G_1} + \frac{F_3 - 1}{G_1 G_2} + \dots + \frac{F_n - 1}{G_1 G_2 \dots G_{n-1}} \quad (3.1)$$

Since the most critical module is the first module in a cascade system for the noise figure, the first module is a low noise amplifier with an excellent low noise figure and high gain. A very similar signal power conditioner and filter block is deployed in receiver hardware. The realized signal power conditioner and filter block is depicted in Figure 3.31.

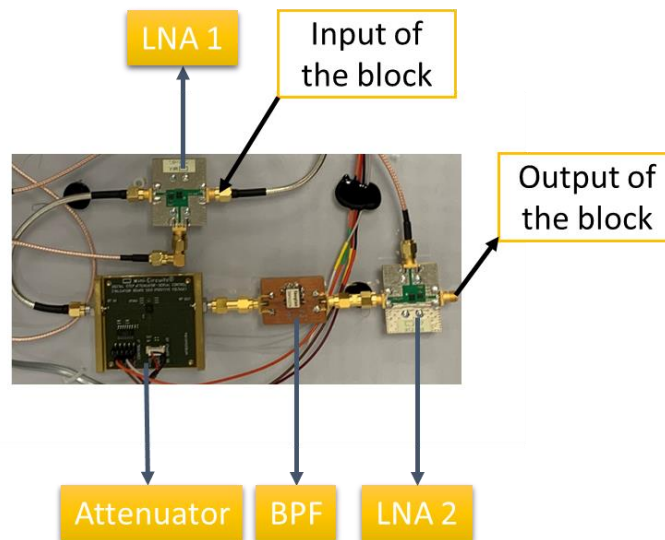


Figure 3.31 Realized signal power conditioner and filter block

The gain of the signal power conditioner and filter block with 20 dB attenuation is presented under section 3.3.2. The measured gain is 23.21 dB when the digital step attenuator's attenuation is set to 20 dB. With 20 dB attenuation in the block, S11 and S22 of the block are measured as less than -10 dB in the operating frequency band. When attenuation increased, the S11 curve moves downward. In the case of no attenuation, the S22 curve is reported to be still less than -10 in the frequency band.

The measurements conclude that the signal power conditioner and filter block may amplify the signal in the range of 11.71-43.21 dB as the attenuation up to 31.5 dB may be introduced by varying the attenuation of the digital step attenuator.

Section 3.3.1 presents the modules that are used to build the signal power conditioner and filter block and reveals out the realized cascaded topology formed by LNA, attenuator, band pass filter, and LNA. A more detailed description with S-parameter measurements are provided under section 3.3.2. The topology is formed in this section step by step starting with a single LNA with an excellent noise figure of 0.9 dB and a gain of 22.4 dB.

### 3.3.1 Signal Power Conditioner and Filter Design

TB-1063-13LN+ evaluation board for LHA-13LN+ from Mini-Circuits is opted out as the LNA modules. LHA-13LN+ is reported to have an excellent low noise figure of 0.9 dB, ultra-high IP3 of 38.3 dB, low voltage requirement between 3 V and 5 V, and gain of 22.4 dB [86].

TB-DAT31R5A-SP+ evaluation board for DAT-31R5A-SP+ from Mini-Circuits is opted out for the digital step attenuator module DAT-31R5A-SP+ is controlled by the 6-bit serial interface to provide attenuation from 0 dB to 31.5 dB with a 0.5 dB step size [87].

DBP.433.T.A.30 is selected as the band pass filter. The 3 dB bandwidth of the filter is 20 MHz and is applicable for civil GPS L1 signals [88].

LNA module TB-1063-13-LN+, the layout of digital step attenuator TB-DAT31R5A-SP+ [89], the band pass filter chip DBP.433.T.A.30, and the evaluation board fabricated for the band pass filter on FR4 are demonstrated in Figure 3.32.

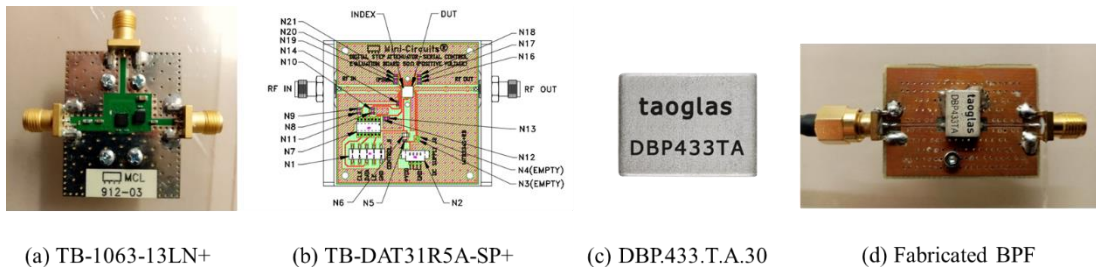


Figure 3.32 Modules in signal power conditioner and filter block

These modules are cascaded in the order of LNA, attenuator, filter, and LNA as shown in Figure 3.31 to form the signal power conditioner and filter block.

### **3.3.2 Signal Power Conditioner S-Parameter Measurements and Results**

In this part, the LNA and the band pass filter (BPF) S-Parameters are measured. Then, LNA-BPF-LNA and LNA-Attenuator-BPF-LNA cascaded systems S-Parameters are measured. S-parameters are measured with the Agilent E5062A S-Parameter Network Analyzer. Before the measurement, the analyzer is calibrated with the Agilent 85032E N-type calibration kit for the frequency between 200 MHz and 650 MHz.

#### **3.3.2.1 S-Parameter Measurement for LNA**

Input and output reflection coefficients ( $S_{11}$  and  $S_{22}$ ), and the gain ( $S_{21}$ ) of the evaluation board TB-1063-LN13 are measured to analyze the LNA performance. During these measurements, the LNA bias voltage is supplied from the voltage regulator block designed and fabricated.

According to the results presented in Figure 3.33,  $S_{11}$  and  $S_{22}$  parameters are below -10 dB at the frequency of 433 MHz, and in a band much larger than the operating frequency. The input and output reflection coefficients are below -10 dB for all frequencies between 233 MHz and 633 MHz. Therefore, it can be said that there is no loss of reflection in the ports. At 433 MHz frequency, the gain of the amplifier measured as 22.43 dB. The measured gain complies with the value presented in the product datasheet.

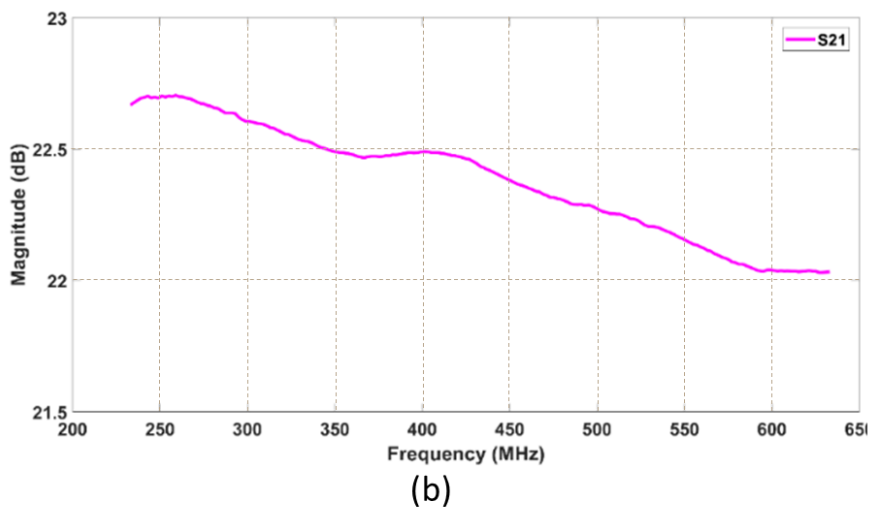
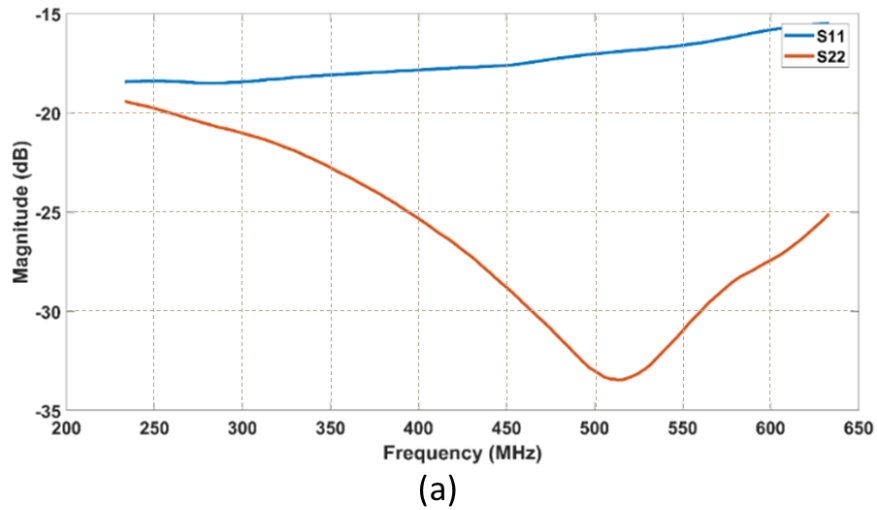


Figure 3.33 (a) Reflection coefficient of the input port (S11) and output port (S22), (b) Gain (S21) Measurement Results

### 3.3.2.2 S-Parameter Measurement for Band Pass Filter

DBP.433.T.A.30 Band Pass Filter Chip is integrated on the designed board (Figure 3.34) and the reflection coefficient at the input and output ports (S11 and S22) and the insertion loss (S21) between the two ports are measured.

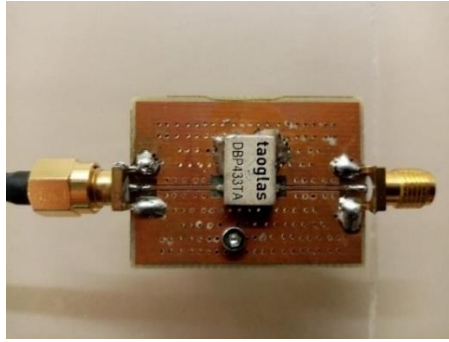
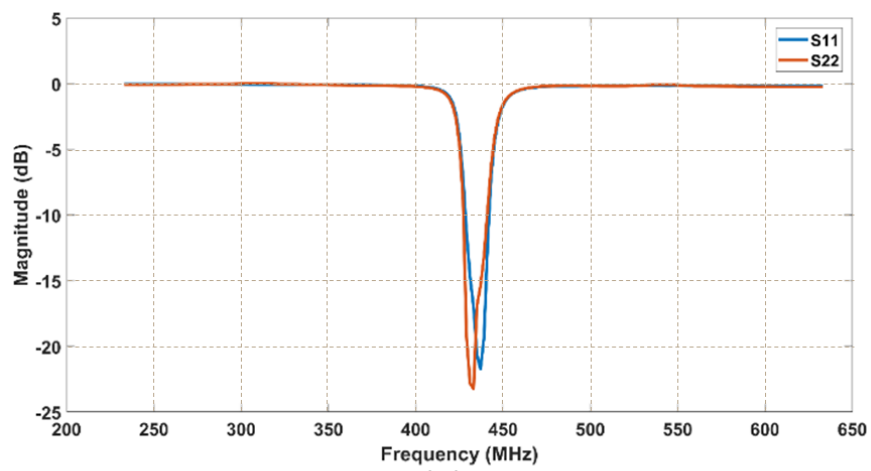
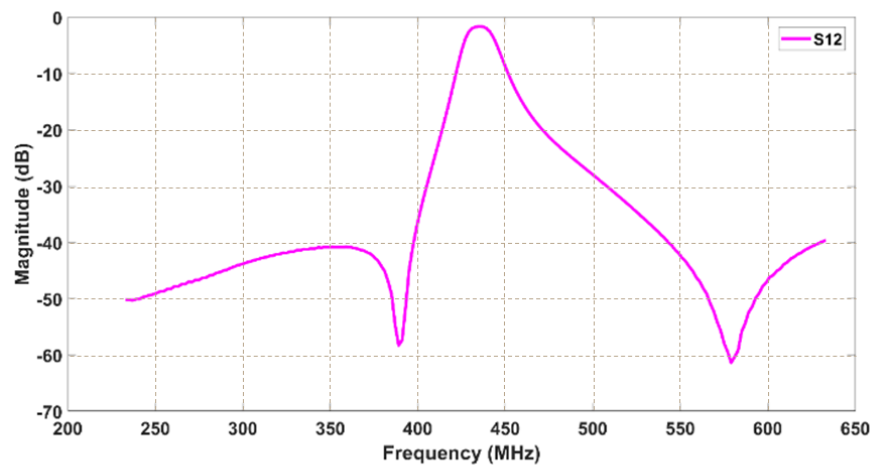


Figure 3.34 BPF as module

S11, S22, and S12 measurement results are given in Figure 3.35.



(a)



(b)

Figure 3.35 (a) Reflection coefficient of the input port (S11) and output port (S22), (b) Insertion loss (S12) measurement results

The input reflection coefficient ( $S_{11}$ ) is less than -10 dB between 428 MHz and 442 MHz while the output reflection coefficient ( $S_{22}$ ) is less than -10 dB between 428 and 440 MHz. Since civilian L1 code has 2 MHz bandwidth, the filter bandwidth is sufficient for the system.  $S_{21}$  measurement result depicts that  $S_{21}$  is -1.7 dB at 433 MHz, -1.9 dB at 431 MHz, and -1.63 MHz at 435 MHz. The 3 dB bandwidth of the filter is measured as 19 MHz between 426 MHz and 445 MHz.

### 3.3.2.3 S-Parameter Measurement for Cascaded LNA, BPF, and LNA

Low noise amplifiers and band pass filter boards are cascaded as the diagram demonstrated in Figure 3.36. Low noise amplifiers TB-1063-LN13 (LNA) and filter DBP.433.T.A.30 board are cascaded in the order shown in the diagram Figure 3.36. In this configuration, S-parameter measurement is performed without the attenuator. The results of the measurements made by placing an LNA, then a filter and LNA are presented in Figure 3.37.



Figure 3.36 Cascaded LNA, BPF, and LNA

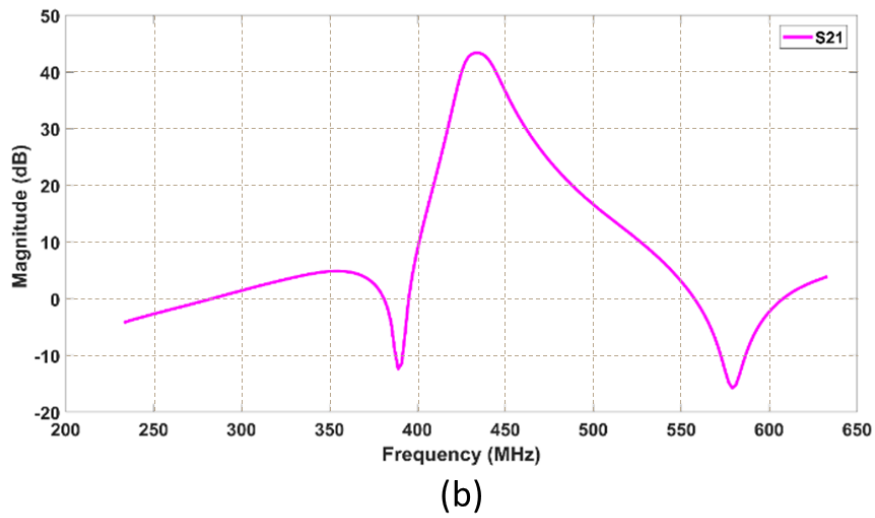
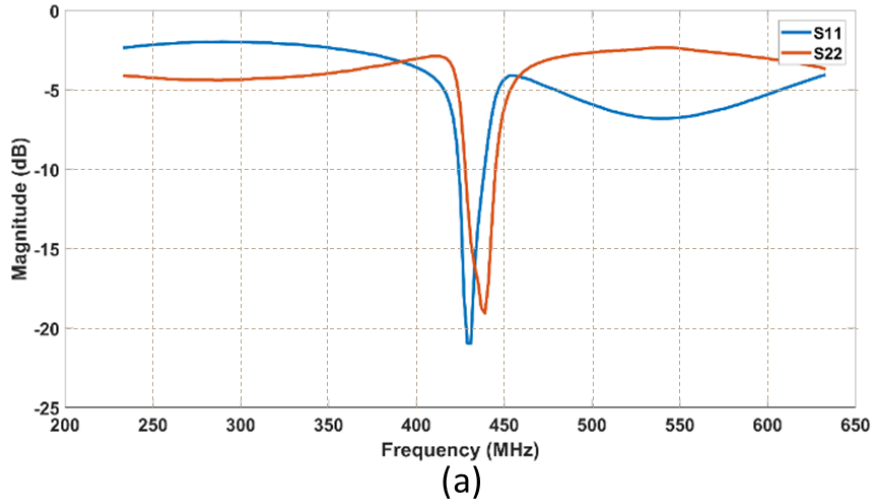


Figure 3.37 S11 and S22 of Cascaded LNA, BPF, and LNA in (a) and S21 of the overall cascaded topology in (b)

As a result of the measurement cascading LNA, BPF, and another LNA, S11 of the cascaded topology is measured as -16.3 dB at 433 MHz while S22 value is -16 dB. The S21 value, that is, the total gain of the system, is measured as 43.38 dB at 433 MHz.

### 3.3.2.4 S-Parameter Measurement for Cascaded LNA, BPF, Attenuator and LNA

This topology is the finalized topology for the signal power conditioner and filter block that is built with Low noise amplifiers TB-1063-LN13 (LNA), band pass filter DBP.433.T.A.30, attenuator TB-DAT31R5A-SP+. This block is the third block in the repeater hardware. The attenuation of the cascaded system is fixed to 20 dB. This means that the measured overall gain for signal power conditioner and filter block is expected to be 20 dB lower than the measurement result given in Figure 3.37b. Moreover, the attenuator module, which is the TB-DAT31R5A-SP+ evaluation board, improves the reflection coefficient value at the input port. The cascaded topology that forms the said block of the repeater hardware is represented in Figure 3.38.

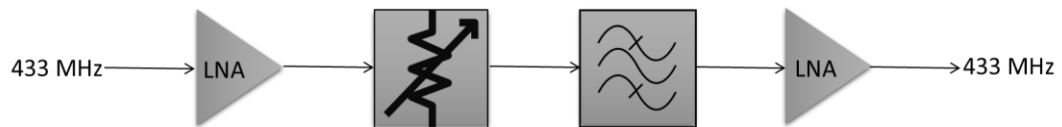


Figure 3.38 Cascaded LNA, BPF, Attenuator and LNA

The reflection coefficients at the input and output ports are presented in Figure 3.39 when the attenuation is set to 20 dB.

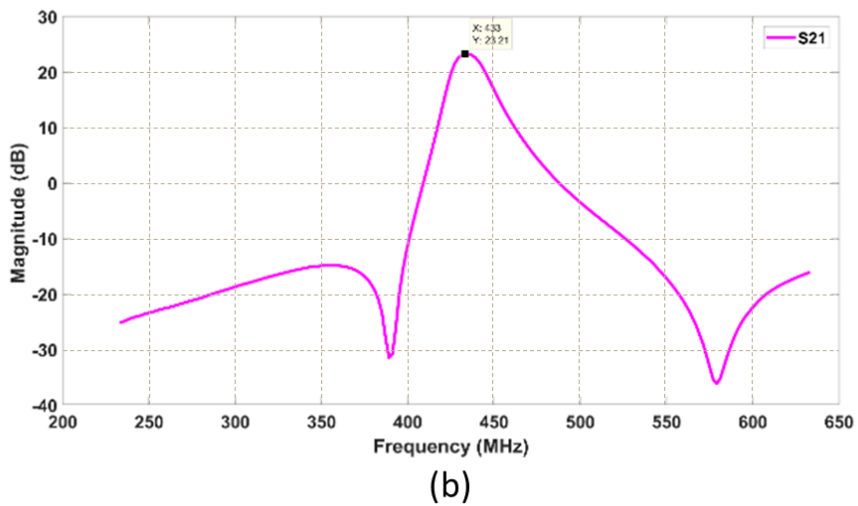
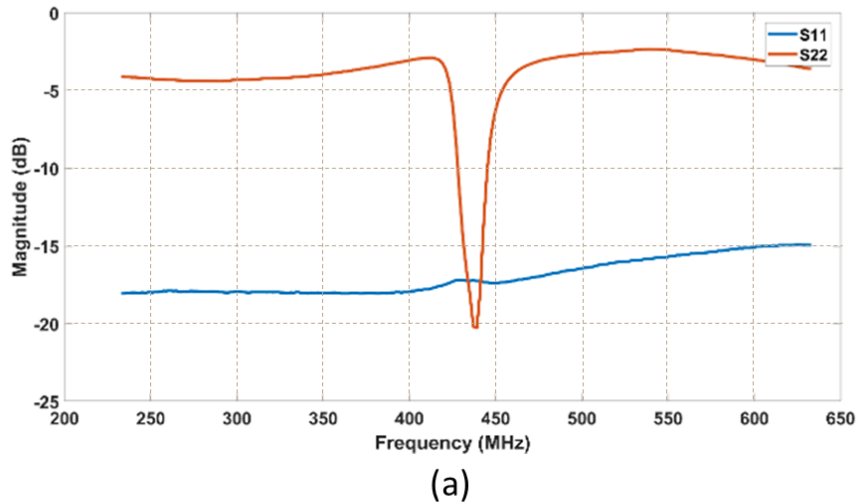


Figure 3.39 S11 and S22 of Cascaded LNA, Attenuator, BPF, and LNA in (a) and S21 of the overall cascaded topology in (b)

The gain of the signal power conditioner and filter block with 20 dB attenuation is measured as 23.21 dB. S11 and S22 of the cascaded topology are measured less than -10 dB in the operating frequency band when the attenuation is 20 dB.

S22 is not affected by the attenuation level. When attenuation increased, the S11 curve moves downward. In the case of no attenuation, S22 curve is reported to be less than -10 in the frequency band as depicted in

### 3.4 433 MHz Directional Indoor Antenna

The directional indoor antenna at 433 MHz is the last block of the repeater hardware. This antenna is responsible to transmit down-converted GPS signals indoors. For improved performance, the back radiation must not exist. Therefore, the antenna is designed to be directional.

Designed antenna is a patch antenna because it is fast and cost-efficient to fabricate patch antennas for narrowband applications proposed in this thesis.

The dimensions of the patch antennas, which are produced with a low dielectric constant material and operate at a frequency of 433 MHz, are too large for indoor positioning. Patch sizes can be reduced by building the patch antenna on a substrate with a higher dielectric constant, but this results in lower antenna gain. For this reason, two high dielectric substrates were used, and an air gap is created between the substrates. When the air gap is left between the substrates, the effective electrical permittivity between the patch and the ground planes is reduced. In this case, the gain increases, but also the patch size increases. In particular, the length of the patch antenna needs to be increased due to the decreased effective dielectric constant. If the dielectric constant decreases keeping the patch size fixed, the resonance frequency shifts to a higher frequency value. Therefore, the patch length must be increased to compensate for the shift. For these reasons, a design with an appropriate size, gain, and efficiency is obtained by using size reduction techniques.

In the antenna design, two Rogers 3010 substrates with dielectric constant equals 9.2 ( $\epsilon_r=9.2$ ) and low tangent loss ( $\tan\delta = 0.0048$ ) are selected for the substrate. Each Rogers 3010 plate has 1.28mm thickness. However, substrates with higher dielectric constants lead to lower gain and poor efficiency. To prevent poor gain and efficiency problems, an air gap between the substrate and the ground is inserted [90].

Section 3.4.1 presents 3 different antenna designs and simulation results for each antenna. The substrate stack-up in all three designs are of the same 3 layered RO3010-airgap-

RO3010 structure. However, the sizes of the patch are halved from 1<sup>st</sup> to 2<sup>nd</sup> design keeping the substrate width and length in the same dimensions. The reduction of patch size is done by short-circuiting the patch to the ground at quarter-wavelength by deploying vias in the 2<sup>nd</sup> design. Then, the ground plane and length of the substrate is halved from 2<sup>nd</sup> to 3<sup>rd</sup> design. The short-circuiting structure in the 3<sup>rd</sup> design is changed from vias to folded conductive tape at the corresponding edge of the patch. As the ground and substrate length is halved, the length of the overall antenna is halved in that the 3<sup>rd</sup> design became more compact than the 1<sup>st</sup> and 2<sup>nd</sup> antennas. A comparison of these 3 designs is provided in section 3.4.1. The 1<sup>st</sup> and the 3<sup>rd</sup> antennas are fabricated and their S11 parameter is measured. The results are provided under section 3.4.2.

Moreover, a 433 MHz dipole antenna design is presented in Appendix C. 1D positioning tests under section 5.3 are completed with the proposed 433 MHz dipole antenna because a directional antenna is not needed in the experimental setup.

### **3.4.1 433 MHz Directional Indoor Antenna Design**

Three different designs have been proposed and one of them is fabricated to deploy in the receiver hardware. The patch and ground sizes with the substrates are reduced from the first design to the third design.

### 3.4.1.1 Design and Simulation of 433 MHz Patch Antenna 1

The design and simulation of this antenna are carried out using HFSS software. Figure 3.40 depicts the optimized antenna sizes and the substrate of the antenna.

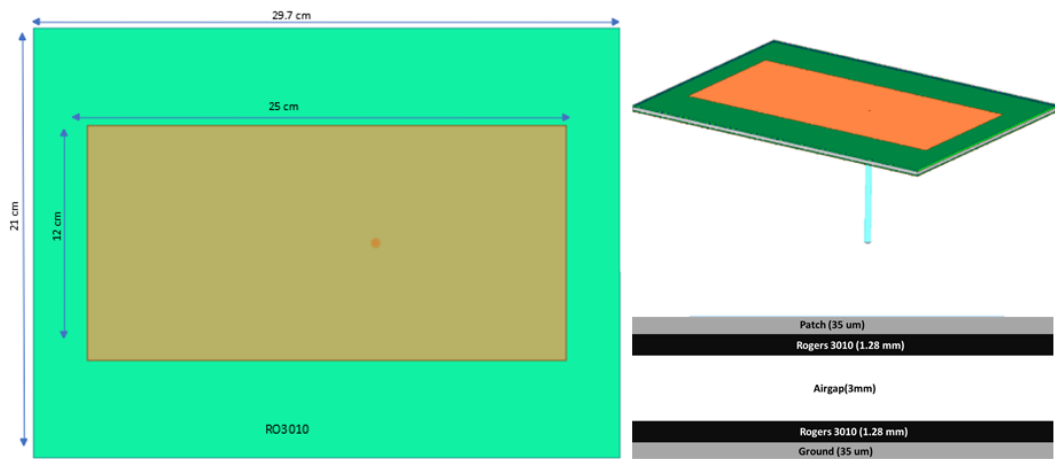


Figure 3.40 Designed 433 MHz Patch Antenna 1 with the optimized dimensions

The substrate consists of 3 layers. The substrate is built by creating an air gap of 3 millimeters between two Rogers RO3010 plates of 1.28-millimeter thickness. The thickness of the air gap has been finalized after several optimizations for the antenna to operate at the frequency of 433 MHz.

The simulation results for the reflection coefficient (S11) and the realized gain values are presented in Figure 3.41 and Figure 3.42, respectively. The simulated S11 value at the frequency of 433 MHz is -16.34 dB while the simulated realized gain value in  $\Theta = 0^\circ$  and  $\Phi = 0^\circ$  direction is 6.27 dBi.

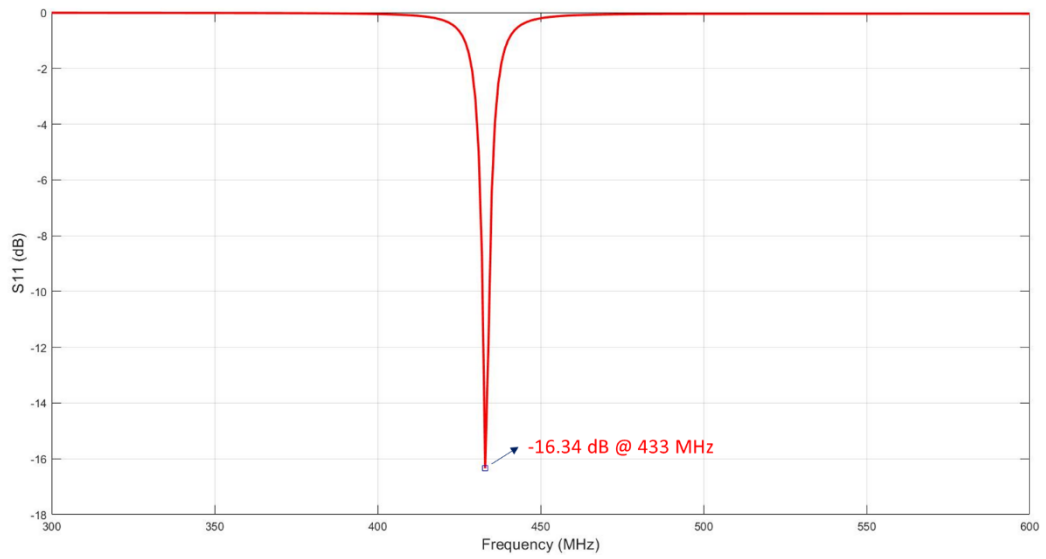


Figure 3.41 S11 simulation result for 433 MHz patch antenna 1

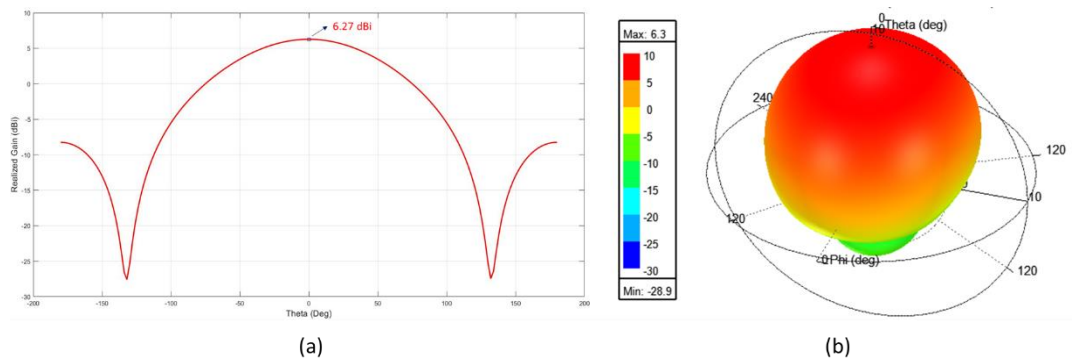


Figure 3.42 Realized gain (a) and radiation pattern (b) simulation results for 433 MHz patch antenna 1

### 3.4.1.2 Design and Simulation of 433 MHz Patch Antenna 2

The design and simulation of the second antenna are also carried out using HFSS software. Several techniques are available to reduce the size of the microstrip patch antenna [90], [91]. One of the techniques that may be applied to reduce the size is the short-circuit quarter-wavelength antenna.

Firstly, using the same substrate structure with the same thickness and area with 433 MHz patch antenna 1, the patch antenna size is reduced to half of 433 MHz patch antenna 1. Vias are inserted close to the feed point in order to short circuit patch to the ground plane. The antenna design, substrate layers, optimized dimensions, and via locations are demonstrated in Figure 3.43.

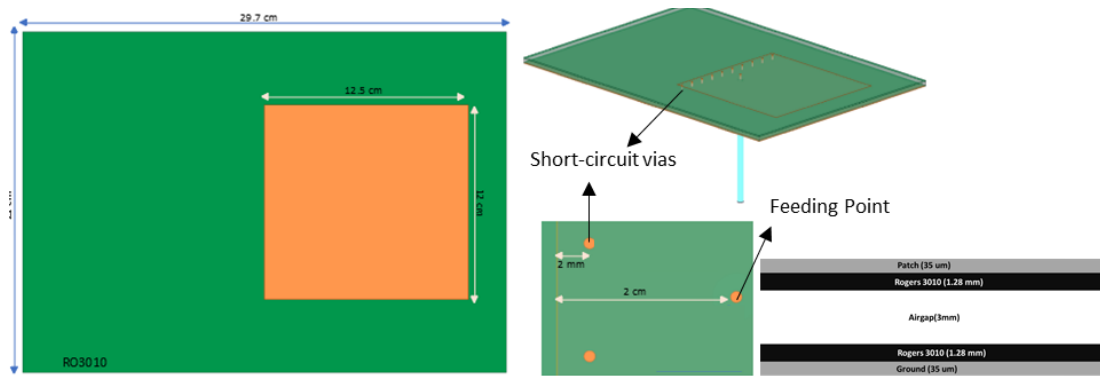


Figure 3.43 Designed 433 MHz Patch Antenna 2 with optimized dimensions and via locations

The simulated results for the reflection coefficient ( $S_{11}$ ) and realized gain are given in Figure 3.44 and Figure 3.45, respectively. The simulated  $S_{11}$  value at the frequency of 433 MHz is -11.9 dB while the simulated realized gain is 2.66 dBi. The gain value is more than 3 dB lower than patch antenna 1 due to the fact that the length of the patch is half of the patch antenna 1.

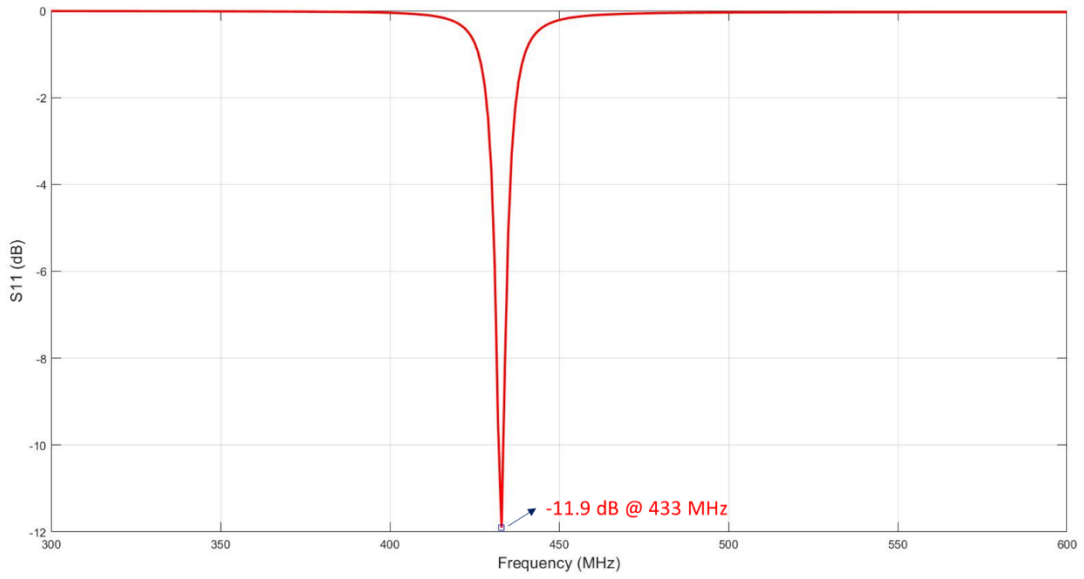


Figure 3.44 S11 simulation result for 433 MHz patch antenna 2

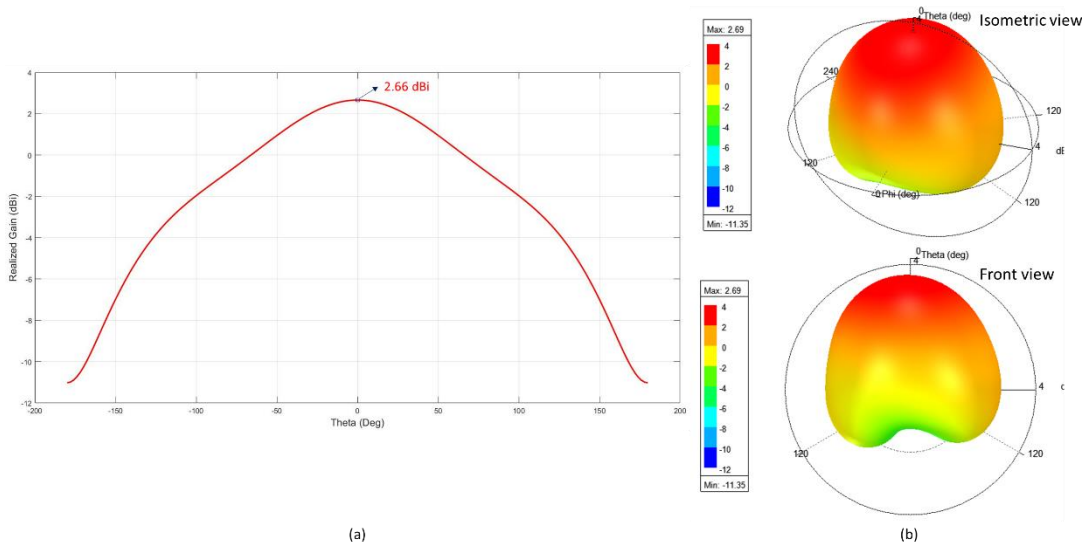


Figure 3.45 Realized gain (a) and radiation pattern (b) simulation results for 433 MHz patch antenna 2

### 3.4.1.3 Design and Simulation of 433 MHz Patch Antenna 3

The design and simulation of 433 MHz patch antenna 3 is carried out using HFSS software. Increasing the number of short-circuit vias creates better grounding. For this reason, instead of the vias shown in Figure 3.43 for the patch antenna 2, a folded copper layer is used to create a continuous grounding and short-circuiting all along that end of the patch for the patch antenna 3. At the same time, the substrate length is reduced to half of the substrate used in patch antenna 2. Antenna 3 and its optimized dimensions are presented in Figure 3.46.

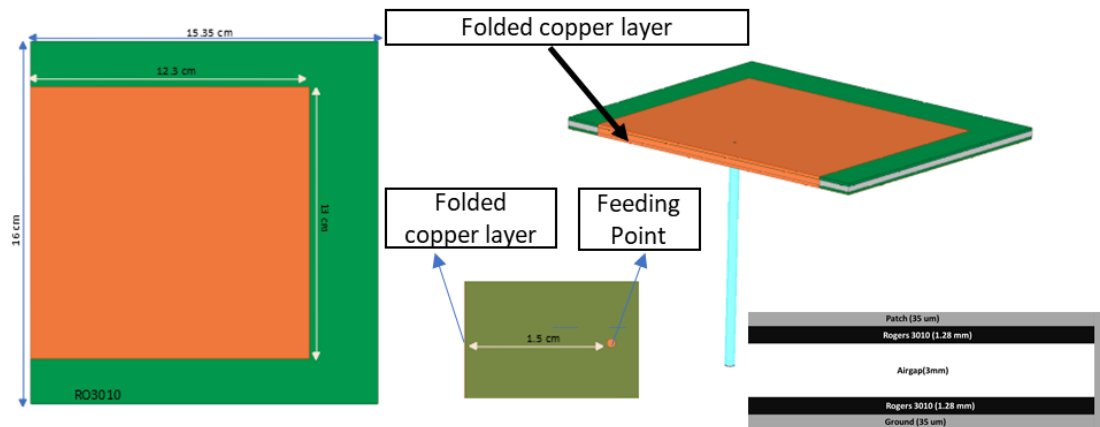


Figure 3.46 Designed 433 MHz Patch Antenna 3 with optimized dimensions and short-circuit layer

The simulated results for the reflection coefficient ( $S_{11}$ ) and realized gain are given in Figure 3.47 and Figure 3.48, respectively. The simulated  $S_{11}$  value at the frequency of 433 MHz is -11.42 dB while the simulated realized gain is 1.5 dBi.

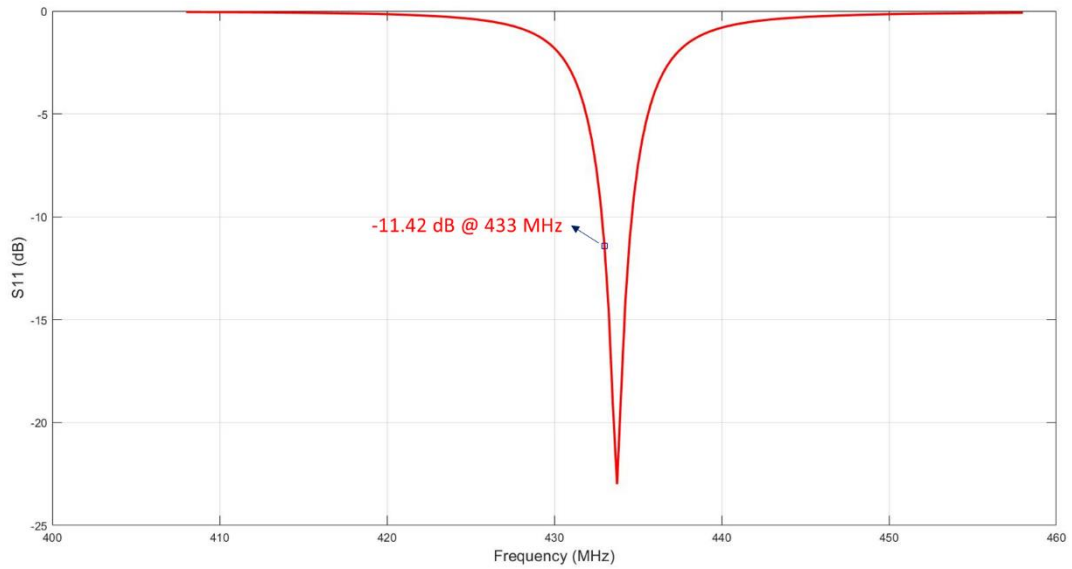


Figure 3.47 S11 simulation result for 433 MHz patch antenna 3

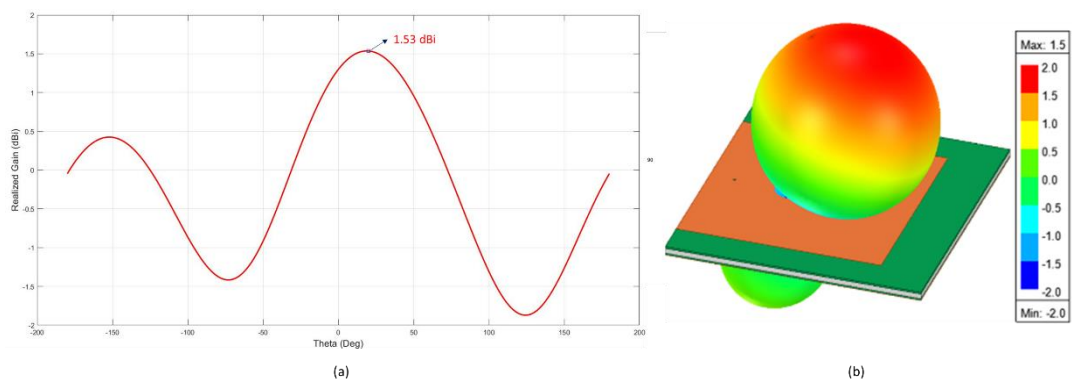


Figure 3.48 Realized gain (a) and radiation pattern (b) simulation results for 433 MHz patch antenna 3

The main beam direction rotates from  $\text{Theta} = 0^\circ$  to  $\text{Theta} = 20^\circ$  while the gain decreases from 2.66 dBi to 1.5 dBi when the patch antenna 3 is compared with patch antenna 2. Since the ground plane is to half of the patch antenna 1 and 2, the back lobe appears stronger, and this squints the main lobe and reduces the gain as shown in Figure 3.48.

Table 3.4 summarizes the simulated S11 value at 433 MHz, the simulated realized gain value at 433 MHz, the design techniques, the dimensions of patch and substrate for each antenna designed at 433 MHz.

Table 3.4 Summary of Designed 433 MHz Patch Antennas

Antenna	Substrate Size	Patch Size	S11 @ 433 MHz	Realized Gain	Design Properties
<b>Patch Antenna 1</b>	29.7 cm x 21 cm	25.7 cm x 12 cm	-16.34 dB	6.27 dBi	<ul style="list-style-type: none"> <li>○ 1.28 mm RO3010, 3 mm airgap, 1.28 mm RO3010</li> </ul>
<b>Patch Antenna 2</b>	29.7 cm x 21 cm	12.5 cm x 12 cm	-11.90 dB	2.66 dBi	<ul style="list-style-type: none"> <li>○ 1.28 mm RO3010, 3 mm airgap, 1.28 mm RO3010</li> <li>○ 10 vias for short-circuit</li> </ul>
<b>Patch Antenna 3</b>	15.35 cm x 16 cm	12.3 cm x 13 cm	-11.42 dB	1.5 dBi	<ul style="list-style-type: none"> <li>○ 1.28 mm RO3010, 3 mm airgap, 1.28 mm RO3010</li> <li>○ Folded copper plate for short-circuit</li> </ul>

Patch antenna 3 is more compact than antenna 1 and 2 by 60.52% in terms of surface area.

### 3.4.2 433 MHz Directional Indoor Antenna Measurement Results

Patch antenna 1 and 3 that have been designed and simulated in section 3.4.1 are fabricated and their S11 measurement is completed and presented in this section.

### 3.4.2.1 S11 Measurement Result for the Fabricated 433 MHz Patch Antenna 1

Spacers of 3 mm height are used to create an air gap between the two pads. The spacers are manufactured using a high-resolution 3D printer. Amphenol SMA connector is used to feed the antenna. This connector is suitable for a 3-layer design since it has a 6-millimeter long input pin. Spacers and connectors are shown in Figure 3.49.

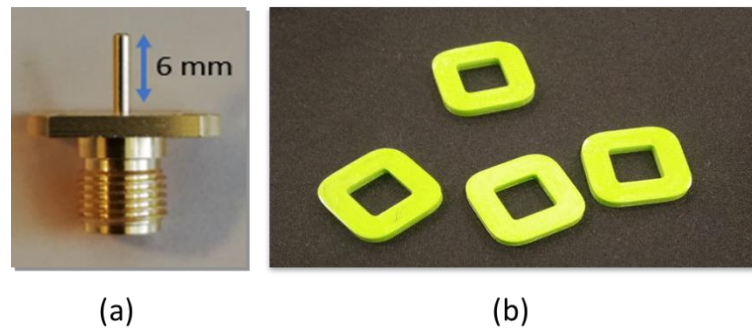


Figure 3.49 50-ohm SMA connector for pin-fed antennas and 3D printed spacers, in (a) and (b), respectively

The fabricated patch antenna for design 1 is presented in Figure 3.50. The conductive tape is used to increase the width of the antenna and to adjust the S11 of the antenna at the 433 MHz.

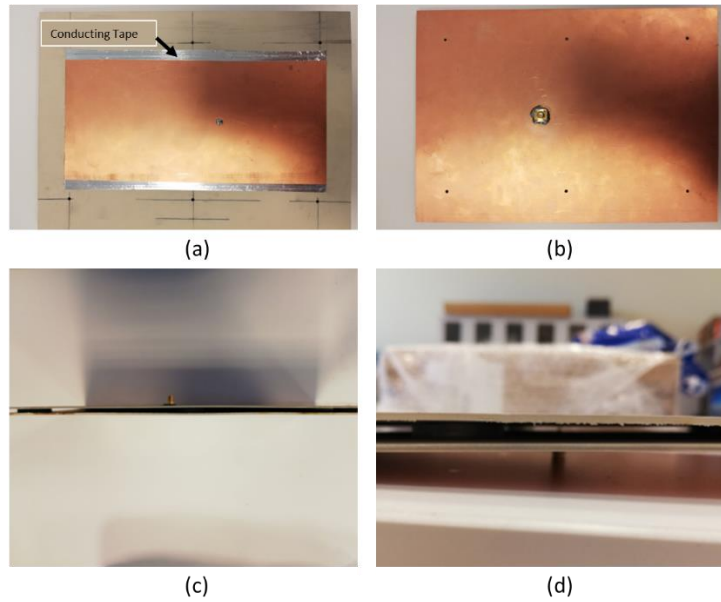


Figure 3.50 Antenna top, bottom, side, and cross-sectional views in (a), (b), (c)-(d), respectively

To adjust the antenna impedance and lower the S11 at 433 MHz, the conductive tape is applied in that the width of the antenna is extended. Measured values with and without the conductive tape that increases the width of the antenna 1 are provided in Figure 3.51 and Figure 3.52.

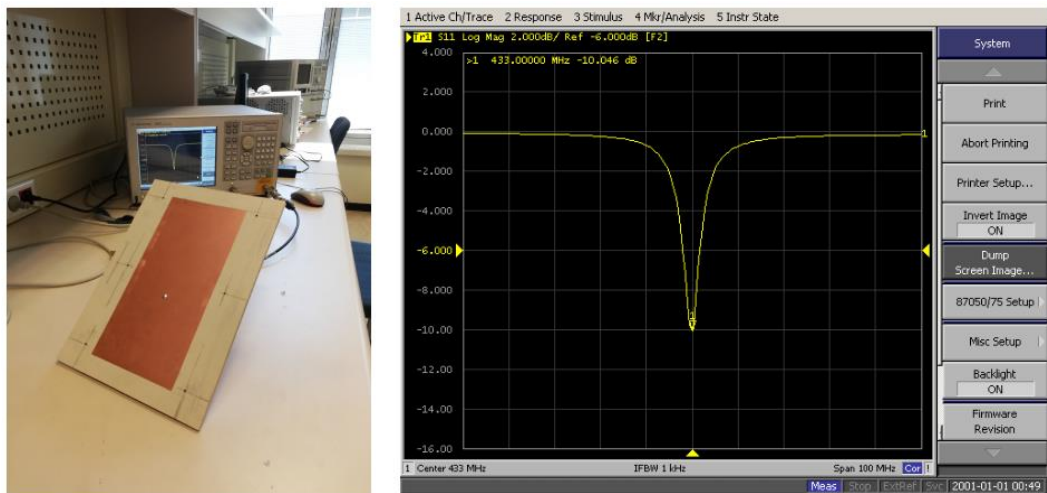


Figure 3.51 Antenna 1 with the dimensions determined in simulations

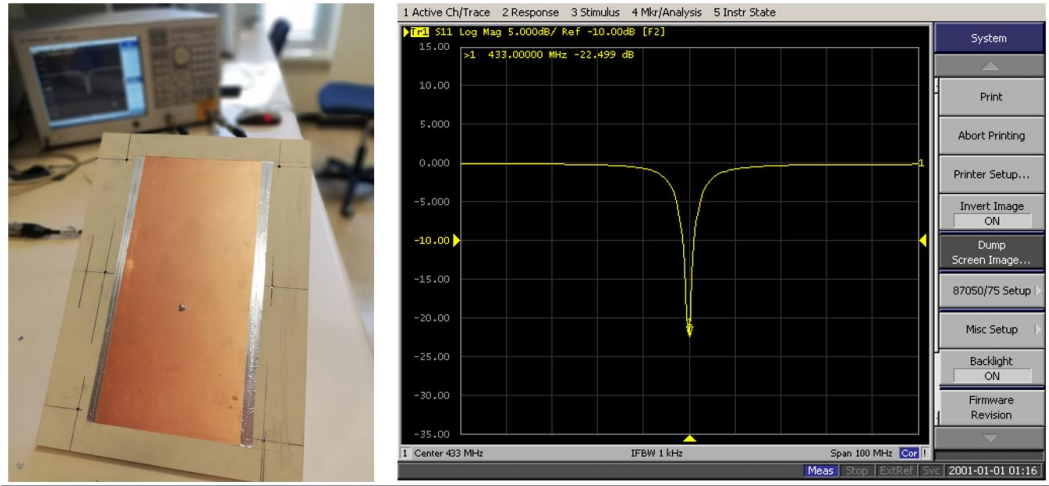


Figure 3.52 Antenna 1 with the copper tape to improve S11 at 433 MHz value by extending the width of the antenna

The antenna 1 fabricated with the dimensions determined in simulations reaches the S11 value of -10.046 dB at 433 MHz while it is less than -16 in the simulations. Therefore, the conductive tape is added to extend the width by 2 cm. As a result of extended width, the S11 value reaches to -22.499 dB at the frequency of 433 MHz.

However, this antenna and the antenna 2 proposed are not as compact as the patch antenna 3. Therefore, antenna 2 has not been fabricated as it is similar to antenna 1 in total sizes.

### 3.4.2.2 S11 Measurement Result for the Fabricated 433 MHz Patch Antenna 3

Patch antenna 3 has the smallest values in length and width. Besides, it has an acceptable gain. For these reasons, this design is opted out for fabrication instead of the patch antenna 2 which has the same volume as patch antenna 1. To create the air gap between the layers, 3-millimeter spacers were used as in the patch antenna 1. The spacers are fabricated using 3D printer technology. Amphenol SMA connector with 6-millimeter connection pin length was used for the feeding of the antenna. The conductive tape is used as a folded

short-circuit connection to ground the patch. The conductive tape is also used to increase the length by 3 mm to adjust the S11 at 433 MHz. The fabricated antenna is demonstrated in Figure 3.53.

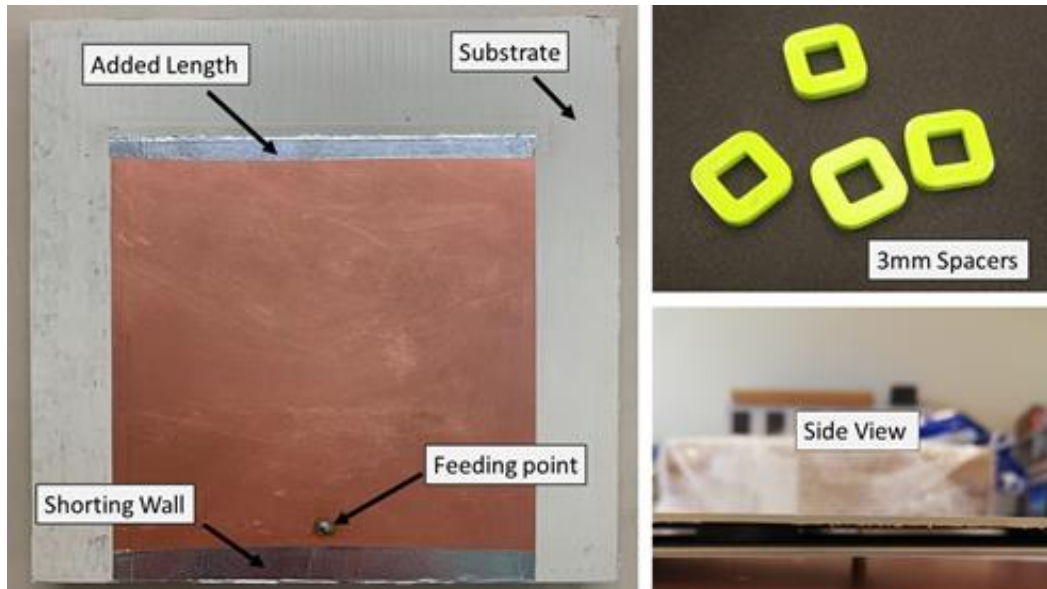


Figure 3.53 Fabricated patch antenna 3

The measured and simulated reflection coefficients are given in Figure 3.54 to compare the simulated design 3 with the fabricated antenna.

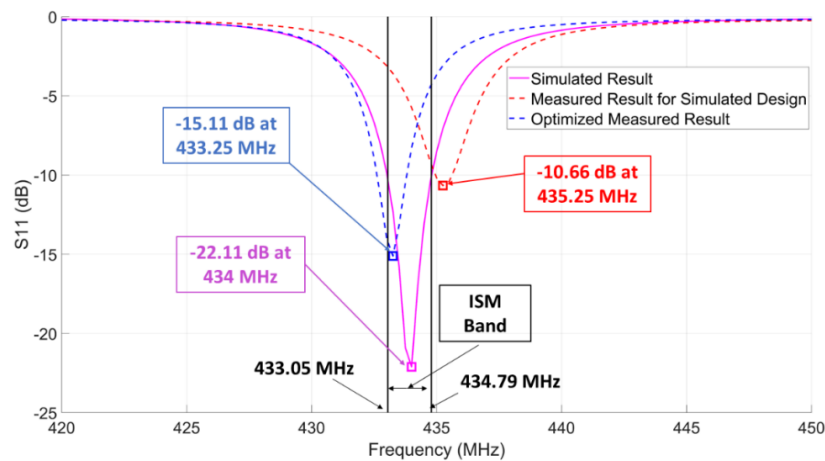


Figure 3.54 Simulated and Measured reflection coefficient for patch antenna 3

Designing an antenna to work in a very small bandwidth like 433 MHz ISM band is not a simple task as the resonance frequency can shift easily out of the band due to variations in dielectric parameters. The red curve shown in Figure 3.54 refers to the measurement of S11 for the fabricated antenna with the dimensions of the design in simulation (which is -10.66 dB at 435.25 MHz). A small copper tape of 3 mm is added to increase the length of the antenna so that the resonance frequency shifts down from 435.25 MHz towards 433 MHz. Extending the length, measured S11 of the optimized fabricated patch antenna 3 reaches -15.11 dB at 433.25 MHz as shown in Figure 3.54 (blue curve). Simulated S11 reaches -22.11 dB at 434 MHz.

### **3.5 Voltage Regulator for Repeater Hardware**

This block is a supporting block in the repeater hardware. The RF signal does not pass through this block, therefore, in this thesis, this block is referred to as a support block that provides DC voltages to the main three blocks, so-called directional outdoor GPS active antenna, down-converter, and signal power conditioner and filter blocks. Directional outdoor GPS active antenna needs 3.3 V DC over TB-JEBT-4R2GW+ bias tee, ADRF6820-EVALZ requires 6 V DC, TB-DAT31R5A-SP+ attenuator requires 3.3 V, and TB-1063-13LN+ LNAs requires 5 V DC. All these requirements are met by the voltage regulator for repeater hardware. Fabricated voltage regulator for repeater hardware is demonstrated in Figure 3.55.



Figure 3.55 Voltage regulator for repeater hardware

The linear voltage regulator chips used for the repeater hardware’s voltage regulator block are presented in Table 3.5. These components are selected considering thermal design terms and equations presented in [92].

Table 3.5 Circuit boards and Linear voltage regulator chips used to supply them with the required input voltage

Selected Regulator	Input Voltage	Output Voltage	The module to which the selected chip supplies DC Voltage
<b>L7806</b>	9 V	6 V	ADRF6820-EVALZ Evaluation Board
<b>UA78M05CDYRG3</b>	9 V	5 V	2x LNA TB-1063-13LN+
<b>UA78M33CDYR</b>	9 V	3.3 V	Attenuator TB-DAT31R5A-SP+
<b>UA78M33CDYR</b>	9 V	3.3 V	Bias Tee TB-JEBT-4R2GW+

The selection of these chips with thermal design considerations, schematic, and layout of the fabricated voltage regulator board are provided with more detail in Appendix A.

In the voltage regulator block of the receiver hardware, the same linear voltage regulator chips for the same output voltages are used. The required voltages in the

programmer/Controller over Wi-Fi block have been met within its design and the regulator chips on itself.

### **3.6 Programmer and Controller over the Wi-Fi**

In this section, the programmer and controller over the Wi-Fi block design is described briefly. This block is common in both repeater and the receiver hardware. This block is responsible for programming and setting ADRF6820 registers that are optimized for down-conversion of GPS signals from 1575.42 MHz to 433 MHz. This block also sets different attenuation values by controlling DAT-31R5A-SP+.

On the other hand, in the receiver hardware, it is responsible for programming ADRF6720-27 and controlling DAT-31R5A-SP+. Moreover, in the receiver hardware, it is also responsible for data transfer from the off-the-shelf GPS receiver EVK-M8T kit.

Therefore, the hardware of this block is designed in line with the needs of the down-converter and up-converter blocks, attenuation setting, and GPS data transfer from receiver to computer. The programmer and controller block contain ESP8266 module with wi-fi, STM32F102 MCU, and necessary voltage regulators that convert 9V input voltage to required DC voltages for the modules in programmer and controller board. ESP8266 acts as a Wi-Fi-UART bridge while STM32F102 is to program ADRF6820 and DAT-31R5A-SP + over SPI.

The programmer and controller hardware is explained with further details in Chapter 4 along with the design and fabrication details.



## **CHAPTER 4 RECEIVER HARDWARE OF THE INDOOR POSITIONING SYSTEM**

The receiver hardware of the proposed indoor positioning system comprises four main building blocks that the received GPS signal at 433 MHz indoors passes and are up-converted back to 1575.42 GPS signal frequency, and two additional blocks that support and control the operation of the main building blocks similar to the repeater hardware. Following is the four main building blocks of the repeater hardware:

- 433 MHz Receiver Antenna,
- Signal Power Conditioner and Filter,
- Up-Converter,
- An off-the-shelf GPS receiver and a computer for data processing with developed software.

In addition to these three blocks; the voltage regulator block and programmer/controller block over Wi-Fi serves as the supporting blocks. The voltage regulator block is responsible for providing required current and voltages to the main building blocks and components forming each main block while controller and programmer block is responsible to adjust attenuation level for signal power conditioning and setting the up-

converter register sets over Wi-Fi. Receiver hardware is demonstrated with building blocks in Figure 4.1.

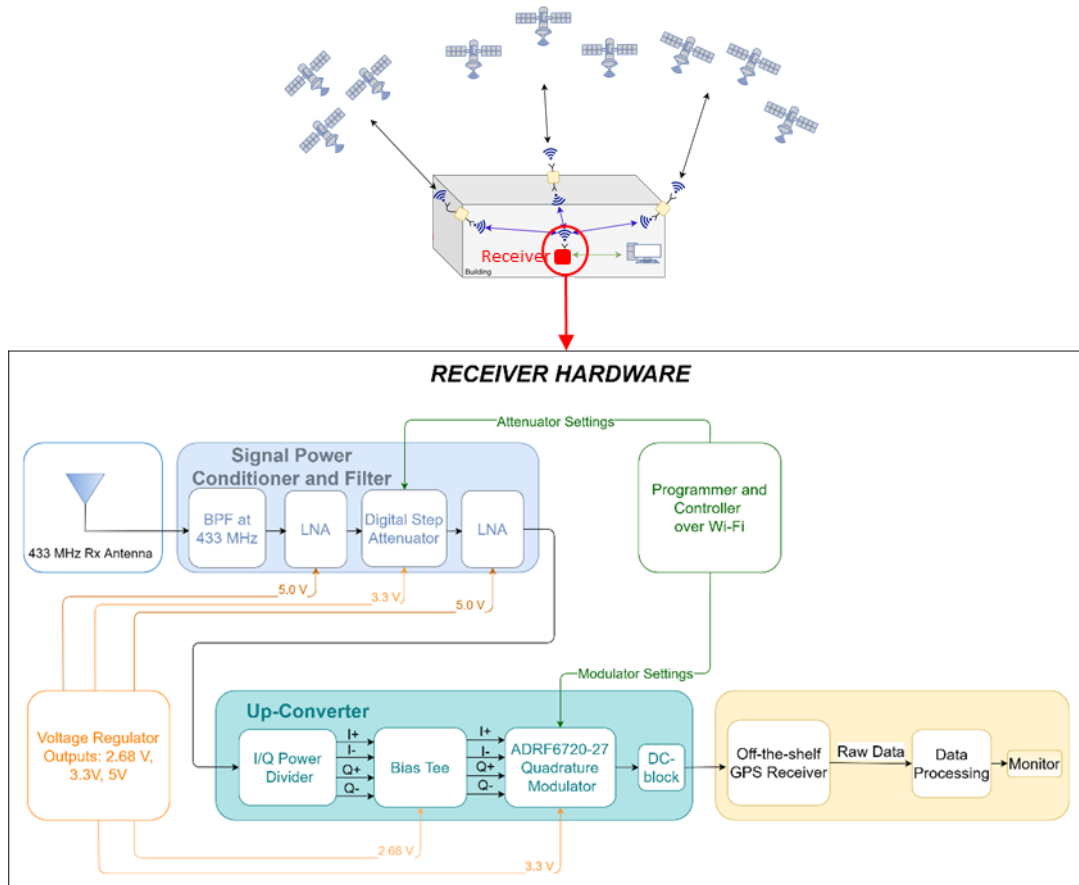


Figure 4.1 Receiver Hardware and Its Building Blocks

The active GPS antennas located outside the building picks up the GPS signals at 1575.42 MHz. The down-converter down-converts the signals at 1575.42 MHz to 433 MHz. The logic behind such an operation is to circumvent the legal restrictions on the GPS repeaters in 1575.42 MHz frequency, thus to be able to increase the coverage due to higher allowable power level and less path loss in the 433 MHz ISM band. The amplifiers in the signal power conditioner and filter block amplify the signal, and whenever it is necessary, the amplification level is reduced by the digital step attenuator up to 31.5 dB. Hence, the gain of the overall system may be set to different values. The directional 433 MHz antenna at each repeater, transmits the down-converted GPS signal indoors.

The passive 433 MHz receiver antenna of a receiver picks up the down-converted signals in an indoor environment. The received signal is filtered and then amplified in the signal power conditioner and filter block. The gain of this stage is also variable due to the digital step attenuator. After the signal power level is set, the GPS signal in 433 MHz is up-converted back to 1575.42 MHz to be delivered to an off-the-shelf receiver. Then, the raw data is extracted from the receiver and processed in MATLAB® by the indoor positioning algorithms developed.

An overview of modules in receiver hardware is provided in Table 4.1

Table 4.1 Overview of Receiver Hardware Modules

<b>Block</b>	<b>Operation</b>	<b>Properties</b>
<b>433 MHz Receiver Antenna</b>	Receives indoor positioning signals at 433 MHz	<ul style="list-style-type: none"> <li>• AEACAC053010-S433 manufacturer coded antenna from Abracon LLC is used. <ul style="list-style-type: none"> <li>○ Monopole antenna</li> <li>○ Operating frequency is 433 MHz</li> <li>○ Gain is 2 dBi</li> </ul> </li> <li>• or Dipole antenna in Appendix C can be used</li> </ul>
<b>Signal Power Conditioner and Filter</b>	Amplifies 433 MHz positioning signals by 11.7 dB to 43.2 dB and filters at 433 MHz	<ul style="list-style-type: none"> <li>• Cascaded topology of <ul style="list-style-type: none"> <li>○ Band Pass Filter DBP.433.T.A.30 at 433 MHz,</li> <li>○ Low Noise Amplifier LHA-13LN+</li> <li>○ Digital Step Attenuator DAT-31R5A-SP+</li> <li>○ And another Low Noise Amplifier LHA-13LN+</li> </ul> </li> <li>• Band pass filter has 19 MHz measured bandwidth from 426 to 445 MHz. The insertion loss of BPF is <ul style="list-style-type: none"> <li>○ -1.7 dB at 433 MHz,</li> <li>○ -1.9 dB at 431 MHz,</li> <li>○ -1.63 dB at 435 MHz.</li> </ul> </li> <li>• LNA gain is measured as 22.43 dB <ul style="list-style-type: none"> <li>○ LNA noise figure is 0.9 dB,</li> <li>○ LNA IP3 is 38.3 dB</li> </ul> </li> <li>• Digital Step Attenuator is variable.</li> </ul>

- Attenuation can vary from 0 to 31.5 dB by 0.5 dB step size
- The attenuator is programmed over SPI from the Controller/Programmer block.

<b>Up-Converter</b>	Up-converts positioning signals from 433 MHz back to 1575.42 MHz GPS signals	<ul style="list-style-type: none"> <li>● I/Q power divider designed and fabricated to provide quadrature RF inputs required for ADRF6720-27-EVALZ</li> <li>● Bias tees are designed and fabricated to provide DC voltage superimposed on quadrature RF signals required at RF input pins of ADRF6720-27</li> <li>● ADRF6720-27 quadrature modulator is used to up-convert previously down-converted GPS signals at 433 MHz back to 1575.42 MHz frequency <ul style="list-style-type: none"> <li>○ ADRF6720-27 is programmed over SPI from Programmer/Controller block</li> <li>○ ADRF6720-27 register sets are optimized for 433 MHz to 1575.42 MHz up-conversion and less loss</li> <li>○ ADRF6720-27 hardware has undergone minor changes</li> </ul> </li> <li>● DC-Block is connected at the output of ADRF6720-27-EVALZ to prevent DC voltage that may be supplied by the off-the-shelf GPS receiver.</li> <li>● The total loss caused by I/Q power divider, bias tees and ADRF6720-27 board, and insertion losses due to cables are measured as 1.2 dB.</li> </ul>
<b>Off-the-shelf GPS Receiver</b>		<ul style="list-style-type: none"> <li>● EVK-M8T evaluation kit with NEO-M8T uBlox chip is used to decode GPS signals provided by the up-converter.</li> </ul>

---

In the following sections, the 433 MHz Receiver antenna, the design of the signal power conditioning and filtering block, and its measurements, the design of the up-converter and its measurements are analyzed in detail.

The proposed receiver hardware that is explained in detail in the following sections is demonstrated with all the modules except the 433 MHz receiver antenna is demonstrated in Figure 4.2.

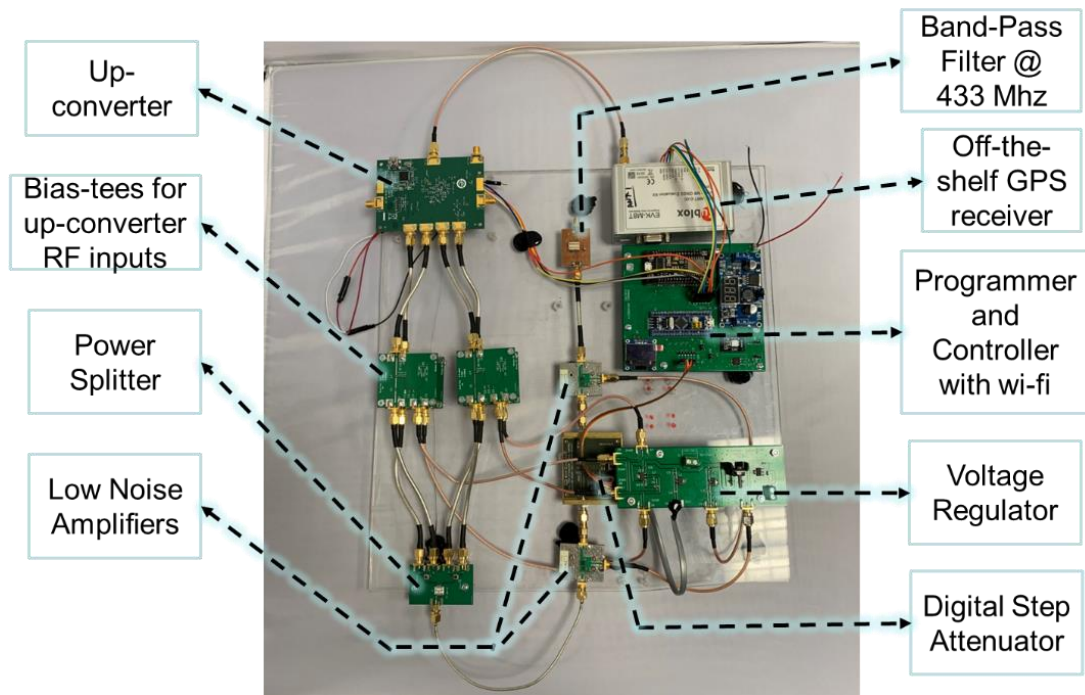


Figure 4.2 Repeater hardware excluding the 433 MHz directional antenna

#### 4.1 433 MHz Receiver Antenna

433 MHz receiver antenna is the stage by which the repeated indoor GPS signals at 433 MHz are picked up. An off-the-shelf 433 MHz antenna is opted out. The selected antenna is demonstrated in Figure 4.3.



Figure 4.3 433 MHz receiver antenna

Abracon LLC's antenna with AEACAC053010-S433 manufacturer number is selected as 433 MHz indoor receive antenna. It's a monopole antenna.

Antenna properties are provided in [93]. The properties of the antenna are summarized in Table 4.2.

Table 4.2 Some features of AEACAC053010-S433 [93]

<b>Antenna Parameters</b>	<b>Values</b>
<b>Operating Frequency</b>	433 MHz
<b>Bandwidth</b>	10 MHz
<b>VSWR</b>	$<2$
<b>Polarization</b>	Linear
<b>Gain</b>	2 dBi

The antenna length is 5.34 cm. The antenna is appropriate for a receiver application in the 433 MHz ISM band due to its small size. Besides, the antenna is not directional. For this reason, it may pick up the signal that will be used in the receiver to determine its position indoors from any direction.

## 4.2 Signal Power Conditioner and Filter

The signal power conditioner and filter block of the receiver is the third part of the receiver hardware and follows the 433 MHz indoor receive antenna. The input signal to this block is at 433 MHz. Similar to the repeater hardware, the RF signals at 433 MHz is amplified to the desired level by fixed-gain amplifiers and digitally controlled step attenuator modules in this block. By changing the attenuation level, the gain may be varied in this block to prevent the near-far effect as the same amplifiers and attenuators used in the repeater hardware are deployed in the receiver hardware as well. The gain is reduced with the digital step attenuator to prevent the near-far effect.

The modules in signal power conditioner and filter block of the receiver are listed as follows:

- Band Pass Filter at 433 MHz
- Low Noise Amplifier
- Digital Step Attenuator
- Low Noise Amplifier

These modules in the block are depicted in Figure 4.4. The first module is the BPF that amplifies the RF signal received by 433 MHz indoor antenna. The first module is followed by the LNA. Then the digital step attenuator and the second LNA are placed.

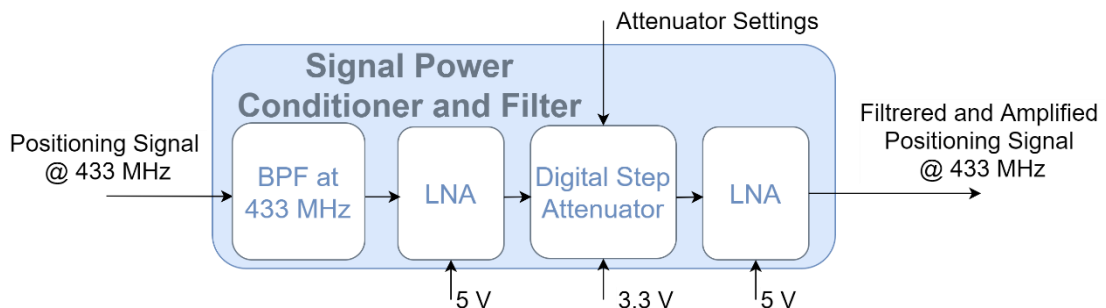


Figure 4.4 Modules in the signal power conditioner and filter block

In this block, two TB-1063-13LN + evaluation boards are used as low noise amplifiers, as in the repeater circuit, TB-DAT31R5A-SP+ as the digital step attenuator and DBP.433.T.A.30 as the band-pass filter for filtering. This block has the same modules used in the receiver hardware explained previously in Chapter 3. Therefore, modules are not explained again in this chapter individually. Instead, the design and the measurements are carried out with the complete cascaded topology is elaborated in the following section. The realized signal power conditioner and filter block is presented in Figure 4.5

According to the measurement results presented in the following section, this block may amplify the signal by 42.72 dB. Due to the variable attenuation in the range of 0-31.5 dB with the digital step attenuator, the amplification can be as low as 11.2 dB. These results differ by 0.5 dB from the signal power conditioner and filter block presented in Chapter 3 for the repeated. This small difference may be due to the existence of an extra 3-inc cable between the BPF and the first LNA or the fabrication of the filter board.

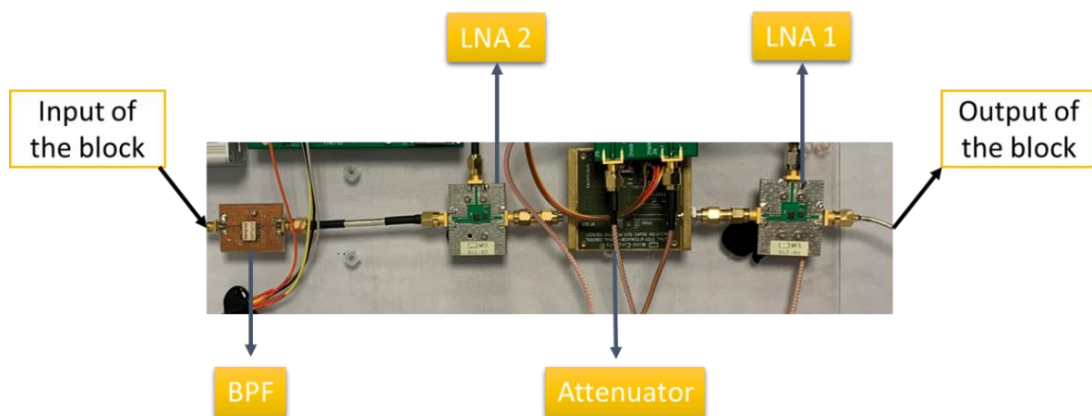


Figure 4.5 Realized signal power conditioner and filter block

#### 4.2.1 Signal Power Conditioner and Filter Design and S-Parameter Measurement

The topology of this block is formed by the cascaded band pass filter at 433 MHz, LNA, digital step attenuator, and another LNA. This topology is represented in the diagram Figure 4.6.

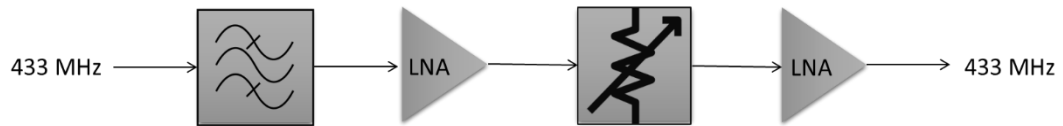
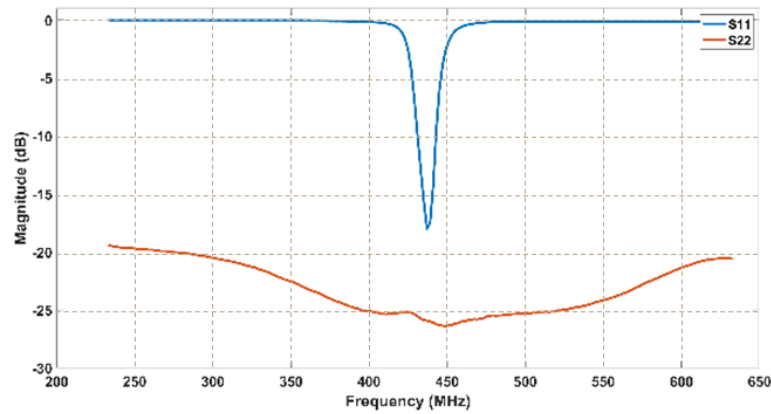


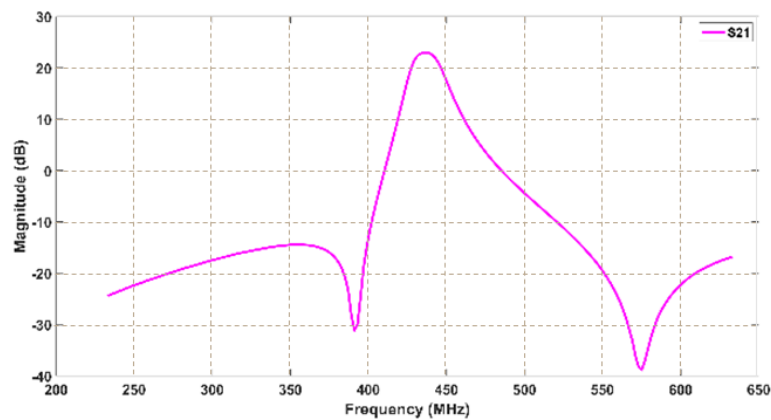
Figure 4.6 Cascaded BPF, LNA, attenuator, and LNA

S-parameters are measured with the Agilent E5062A S-Parameter Network Analyzer. Before the measurement, the analyzer is calibrated with the Agilent 85032E N-type calibration kit for the frequency between 200 MHz and 650 MHz.

S-parameters are measured when the attenuation of TB-DAT31R5A-SP+ is set as 20 dB. Measured S-parameters for the selected topology is provided in Figure 4.7.



(a)



(b)

Figure 4.7 (a) Reflection coefficient of the input port (S11) and output port (S22), (b) Gain (S21) Measurement Results

The S11 value measured at the input port of the block (filter's input port) is less than -10 dB between the 431 and 443 MHz. The S22 value measured at the output port (the output port of the amplifier located at the end) is less than -10 dB in for a much wider frequency range. The overall measured block gain when the attenuation is 20 dB is 22.72 dB at 433 MHz frequency. So, the maximum gain that this block may reach is 42.72 dB, and minimum gain achievable is 11.2 dB due to the variable attenuation in the range of 0-31.5 dB with the digital step attenuator.

### 4.3 Up-converter

The up-converter block is the third part of the receiver hardware and follows the signal power conditioner and filter that amplifies and filters the signal. The positioning signals that have already been down-converted and retransmitted indoors by repeaters are up-converted back to 1575.42 MHz GPS frequency to be delivered to the off-the-shelf GPS receiver. This block consists of 4 modules listed as follows:

- I/Q power divider,
- Bias tee,
- ADRF6720-27 Quadrature Demodulator,
- DC-block

These modules in the block are depicted in Figure 4.8. The first module is an I/Q power divider that provides I+, I-, Q+, and Q- RF signals to the inputs of the ADRF6720-27-EVALZ quadrature modulator. ADRF6720-27-EVALZ up-converts the previously down-converted GPS signals at 433 MHz back to 1575.42 MHz GPS frequency that an off-the-shelf receiver may decode. ADRF6720-27-EVALZ also requires 2.68 V DC at the RF inputs. Therefore, a bias tee is placed in between the I/Q power divider and each RF input port of ADRF6720-27-EVALZ. Since there are 4 RF inputs, 4 bias tees are used. A DC-block is placed at the output of this block to prevent a DC voltage may come from the off-the-shelf receiver.

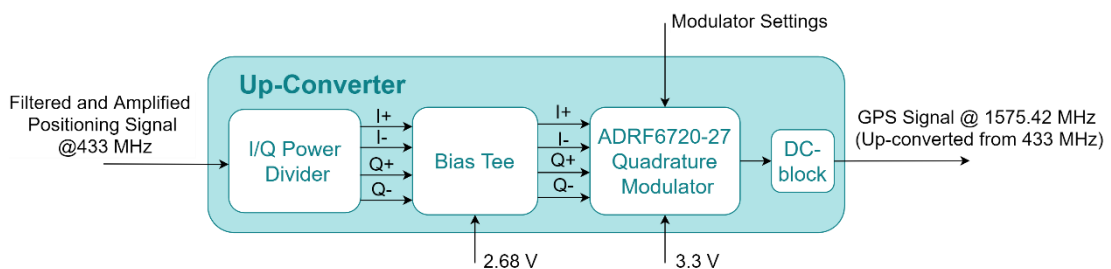


Figure 4.8 Modules in the up-converter block

Section 4.3.1 describes briefly the modules in the up-converter block and presents how they are brought together to build the block. Following that, in the next section optimization of register sets through the interface of the ADRF6720-27 is explained with the measurement result on this module in detail. In the next section, section 4.3.3 the overall performance of the up-converter with optimized settings is revealed with the measurements for the whole block. The measured loss of the up-converter block is found as 1.2 dB under Section 4.3.3.

### **4.3.1 Up-Converter Modules and Design**

As mentioned previously, the up-converter consists of an I/Q power divider, a bias tee for each RF input of ADRF6720-27-EVALZ, ADRF6720-27-EVALZ quadrature demodulator, and a DC-block.

Fabricated I/Q power divider is demonstrated in Figure 4.9a. In the design of the I/Q power divider, one QBA-07+ 90-degree hybrid power splitter, and two SBTCJ-1W+ 180-degree hybrid power splitters each of which is connected to one output port of QBA-07+ are used. The insertion losses of QBA-07+ and SBTCJ-1W+ are 0.5 dB and 0.7 dB, respectively [94], [95]. Using this power divider, a 180-degree phase difference is obtained between signals denoted with + and –, while the phase difference between I and Q signals is 90-degree. Since the RF signal is divided into 4, the power of the signal is reduced by approximately 6 dB at each output of the power divider. Each output of the power divider circuit is connected to a bias tee. Thus, RF signals are delivered from power divider to the RF inputs superimposed with 2.68 V required at the RF inputs of ADRF6720-27-EVALZ.

The bias tee module is demonstrated in Figure 4.9b. The simulation results for bias tee show that its a wideband bias tee and applicable for the work presented in the thesis and

S21 insertion loss value is around 0.142 dB at 433 MHz. A separate bias tee is installed for each I and Q channel, as shown in Figure 4.9c. For this reason, 4 bias tees are used. Two bias tees are mounted on top of each other with supports for space-saving purposes. Thus, the 2.68 Volt DC voltage from voltage regulator of receiver hardware and RF signals from I/Q channels are superimposed and delivered to the attributed input port of the Analog Devices company's ADRF6720-27 EVALZ board demonstrated in Figure 4.9d [96].

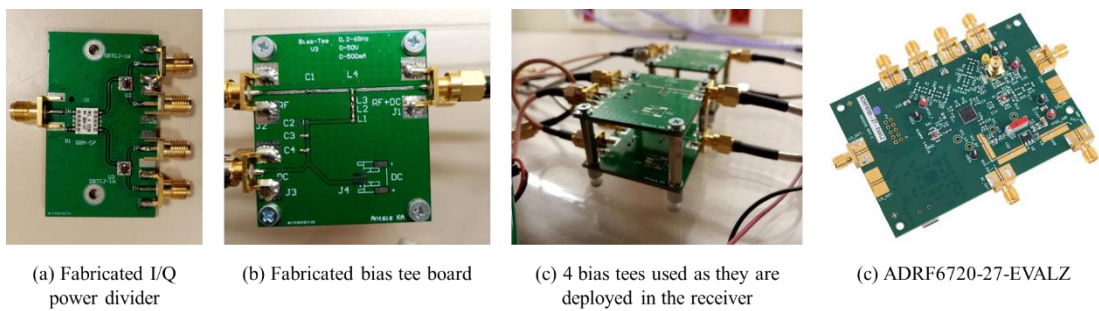


Figure 4.9 Modules used in the up-converter block

In addition to the 2.68 Volt DC voltage on the RF input ports, the ADRF6720-27-EVALZ also needs 3.3 Volts DC voltage. All DC voltages are supplied from the voltage regulator board designed and fabricated for the receiver hardware. ADRF6720-27-EVALZ may be programmed via Customer Evaluation Software with a computer using the USB port on it or via SPI connection from the programmer/controller board. ADRF6720-27-EVALZ board up-converts the 433 MHz signals back to 1575.42 MHz frequency. In this way, the system is aimed to operate with GPS receiver circuits (e.g. Ublox) which are widely used at the frequency of 1575.42 MHz.

With the DC block placed at the output of the frequency up-converter block, the DC voltage that may be generated by the off-the-shelf GPS receivers has been eliminated and the system has not been protected.

Connections between the I/Q power divider outputs and the RF input of bias tee circuits are provided by Crystek Company's CCSMA18-MM-141-5 manufacturer coded 5-inch-long coaxial cables. Connections between the RF+DC output of the bias tee circuits and

the I +, I-, Q +, Q- RF inputs of ADRF6720-27-EVALZ are provided with 4-inch long coaxial cables of Crystek Corporation with CCSMA18-MM-141-4 manufacturer code. The four modules in the up-converter block that up-converts positioning signals at 433 MHz back to 1575.42 MHz and deliver to the off-the-shelf receiver are depicted with connections among them in Figure 4.10.

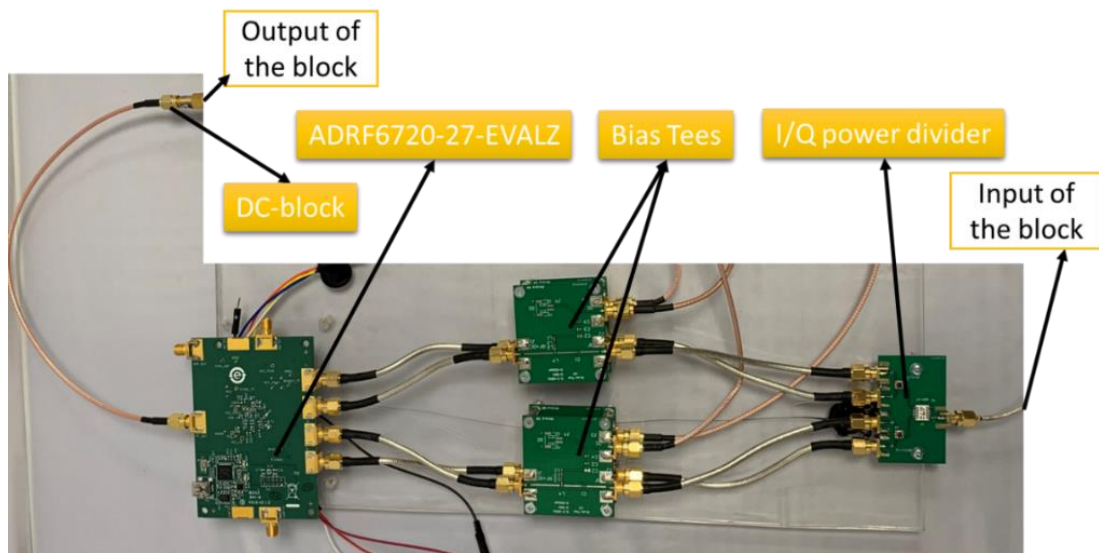


Figure 4.10 Up-converter block formed with the modules presented

#### 4.3.1.1 Bias Tee Design and Simulations

The bias tee in Figure 4.9b is designed using 4 capacitors and 4 inductors. The values of C1, C2, C3, and C4 capacitors are 36 pF, 1 uF, 0.1 uF, and 100 pF, respectively, while each inductor is of 15 nH. The EM simulation and post-layout simulation for the designed board are carried out using NI AWR software as shown in Figure 4.11.

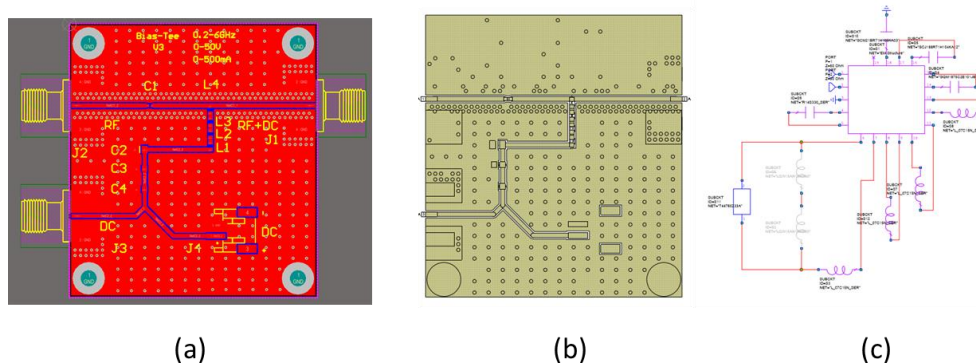


Figure 4.11 Layout in Altium (a), EM (b) & post-layout (b) simulations of bias tee in AWR

S-parameters obtained as a result of post-layout simulation justifies that the designed bias tee has very low insertion loss at the operation frequency. The results are provided in Figure 4.12.

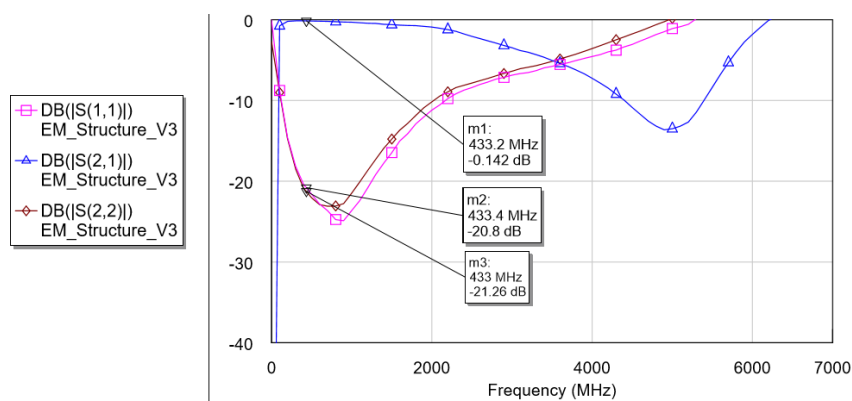


Figure 4.12 Post Layout Simulation Results for S-parameters

According to these results, when bias tee is designed with values selected for C1-4 and L1-4, S11 and S22 values are less than -20.8 and -21.26 dB, respectively, at 433 MHz frequency. S21 insertion loss value is around 0.142 dB. Based on these results, the circuit layout is confirmed and the board is fabricated. Four bias tees used in receiver hardware is shown in Figure 4.9c.

The next section presents the measurements carried out module-wise and through the overall up-converter block.

### **4.3.2 Up-Converter Optimizations**

The up-converter block is optimized through modifications in ADRF6720-27-EVALZ hardware and register setting of the ADRF6720-27 chip on the board. The hardware modifications in this block are not as extended as the modifications done on the ADRF6820-EVALZ board in the down-converter board.

#### **4.3.2.1 ADRF6720-27-EVALZ Hardware Modifications**

The optimization of this board has been carried out in terms of the register settings for 433 MHz indoor positioning system. The main change in the hardware of the evaluation board is the integration of an oscillator at 38.4 MHz frequency.

The only modification carried out is the integration of an oscillator that oscillates at 34.8 MHz. Similar to the ADRF6820-EVALZ used in the down-converter block, this component is necessary to generate the local oscillator (LO) input signal internally. For this reason, IQD Frequency Products' oscillator with the product number of LFTCXO070898REEL has been integrated into the Y2 region on the board.

#### **4.3.2.2 Setting ADRF6720-27-EVALZ Register Sets for the Optimized Performance for the Said Frequency Up-Conversion**

The ADRF6720-27-EVALZ evaluation board has been programmed via Customer Evaluation Rev 0.0.2 software and the final register sets that optimize the performance of

the circuit for up-conversion from 433 MHz to 1575.42 GPS frequency is obtained. The values shown in Figure 4.13 optimizes the performance of the system. Each value seen on the programming interface corresponds to some bits in the register sets which can be seen in the datasheet of ADRF6720-27. Then, these register sets are recorded and loaded into the ADRF6720-27 chip via the serial interface.

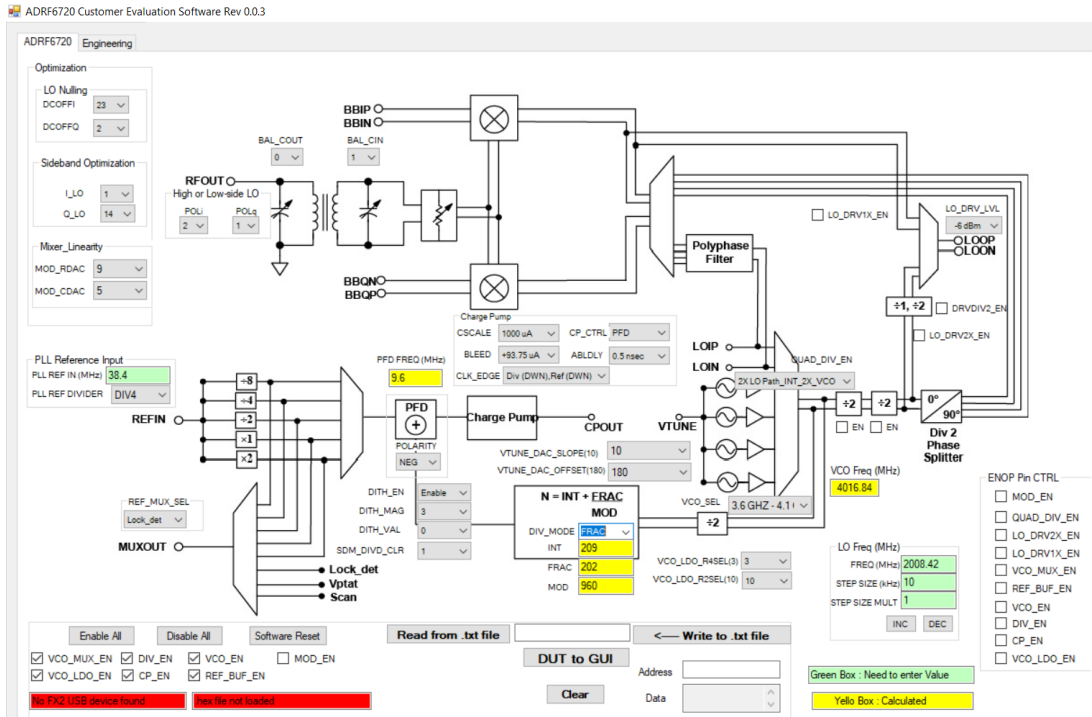


Figure 4.13 ADRF6720-27 customer evaluation software interface and the optimized values

Below explained how the values and settings presented in Figure 4.13 are determined in detail.

1. The LO frequency is set to 2008.42 MHz for the ADRF6720-27. The RF signal reaches this card with a frequency of 433 MHz. Similar to ADRF 6820, the channels are set to “normal” when POLI and POLQ are 2 and 1, respectively as summarized in [84].

2.

Table 4.3 LO polarity settings [84]

<b>Register Bits</b>	<b>Description</b>	<b>Setting (Binary)</b>	<b>Quadrature polarity</b>
<b>POL_Q</b>	Q channel	01	Inverted Q polarity
	polarity	10	Normal Q polarity
<b>POL_I</b>	I channel	01	Normal I polarity
	polarity	10	Inverted I polarity

Since both channels are at the normal polarity and Q channel is 90 degrees ahead of channel I (as previously explained in Chapter 3 for ADRF 6820 interface). The RF signal frequency ( $f_{RF}$ ) at the output of the mixer is lower than the LO frequency ( $f_{LO}$ ). This type of LO injection is called high-side LO injection. The signal at mixer output is at the frequency of 1575.42 MHz and also at 2441.42 due to the image frequency. However, the signal at 2441.42 MHz at mixer output is suppressed and the signal at the frequency of 1575.42 MHz is obtained at the mixer output.

The image frequency rejection is measured using Rohde & Schwarz FSH8 Spectrum Analyzer and Agilent E4437B ESG-DP Serial Digital RF Signal Generator. A 433 MHz signal is supplied with -15 dBm power to the ADRF6720-27 from I/Q power divider input. The measured signal at the output of ADRF6720-27 at 1575.42 MHz is -17.9 while it is -43.2 dBm at 2441.42 MHz. The measurement results are demonstrated in Figure 4.14. One should note that at the time of this measurement, not all the values are optimized. Therefore, the signal loss from 433 MHz to 1575.42 MHz does not represent the final obtained loss of the system. That measurement is presented later in this chapter. The image rejection calculated according to the measurement results is 28.2 dB.

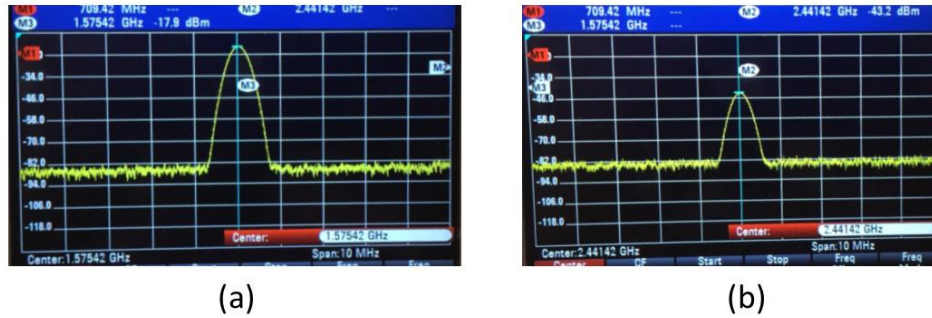


Figure 4.14 Output signal level at 1575.42 MHz and 2441.42 MHz, respectively, in (a) and (b)

3. As explained previously, there is 2.68 V DC voltage at each RF input of ADRF6720-27. The DC offset on I/Q channels may cause carrier feedthrough. Carrier feedthrough is nulled by setting appropriate values for DCOFFI and DCOFFQ parameters according to Figure 4.15.

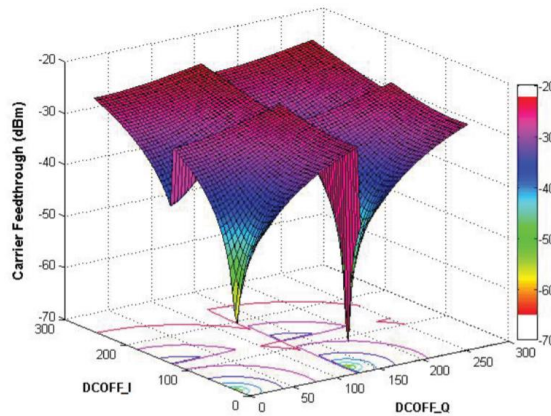


Figure 4.15 DCOFFI and DCOFFQ settings for carrier feedthrough nulling

Based on the graph presented in Figure 4.15, the carrier feedthrough is reduced to the lowest value (approximately -60 dBm) by setting DCOFFQ and DCOFFI, respectively, as 2 and 23.

4. Changing the BAL\_CIN and BAL\_COUT parameters, the capacitances parallel to balun may be varied so that the resonance frequency and the gain of the module can be adjusted [84]. Appropriate values for the output frequency of 1575.42 MHz are selected from the data provided in Figure 4.16.

BAL_CIN	BAL_COUT	Frequency Range (MHz)
0	0	$f_{RF} > 1730$
1	0	$1550 < f_{RF} < 1730$
2	0	$1380 < f_{RF} < 1550$
3	0	$1250 < f_{RF} < 1380$
4	0	$1170 < f_{RF} < 1250$
8	0	$1100 < f_{RF} < 1170$
9	0	$1020 < f_{RF} < 1100$
10	0	$970 < f_{RF} < 1020$
11	0	$930 < f_{RF} < 970$
12	0	$890 < f_{RF} < 930$
13	0	$840 < f_{RF} < 890$
14	0	$820 < f_{RF} < 840$
15	0	$780 < f_{RF} < 820$
15	3	$730 < f_{RF} < 780$
15	8	$680 < f_{RF} < 730$
15	11	$630 < f_{RF} < 680$
15	15	$f_{RF} < 630$

Figure 4.16 Optimum balun setting for the desired frequency of 1575.42 MHz is highlighted in red rectangle

Therefore, the BAL\_CIN value is set to 1, and the BAL\_COUT value is set to 0 so that the balun operation is optimized for 1575.42 MHz RF output.

- By changing the I\_LO and Q\_LO values in ADRF6720-27, it is possible to suppress undesired sideband signals [84]. The optimization plot is provided in [84] for LO frequency of 2140 MHz.

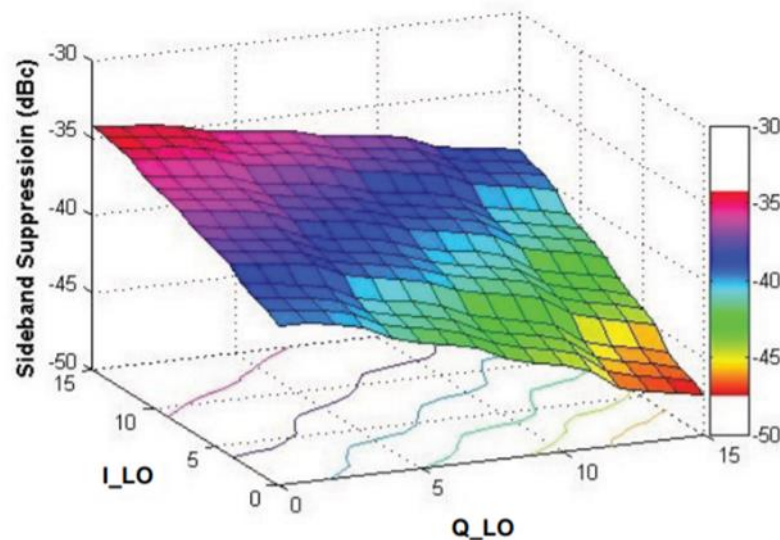


Figure 4.17 I\_LO and Q\_LO setting for sideband suppression [84]

The graphic in Figure 4.17 has been given for LO at 2140 MHz. Although the frequency of LO that is opted out is 2008.42 MHz in this thesis, the presented graphic is adequate for an estimation. In the end, I\_LO and Q\_LO values are determined as 1 and 14, respectively. Thus, the suppression of sideband signals is expected to be more than -45 dBc.

Thus, the ADRF6720-27 evaluation board has been optimized. According to the determined I/Q polarity, module connections are completed. In the next chapter, the measurement results for the whole up-converter block is presented.

### **4.3.3 Up-Converter Measurement Results**

After ADRF6820-27-EVALZ optimized and connections between modules are completed considering I/Q polarities, S-Parameter measurement of I/Q divider module and the whole blocks loss measurements are carried out.

#### **4.3.3.1 I/Q Power Divider S-Parameter Measurements**

The phase difference between the input port and each quadrature output port is measured for the fabricated I/Q power divider with the Agilent E5062A S-parameter network analyzer. Moreover, the magnitude of S-parameter from the input to quadrature outputs is measured. The results are presented, respectively, in Figure 4.18 and Figure 4.19. Before the measurements, the analyzer has been calibrated with the Agilent 85032E N-type calibration kit.

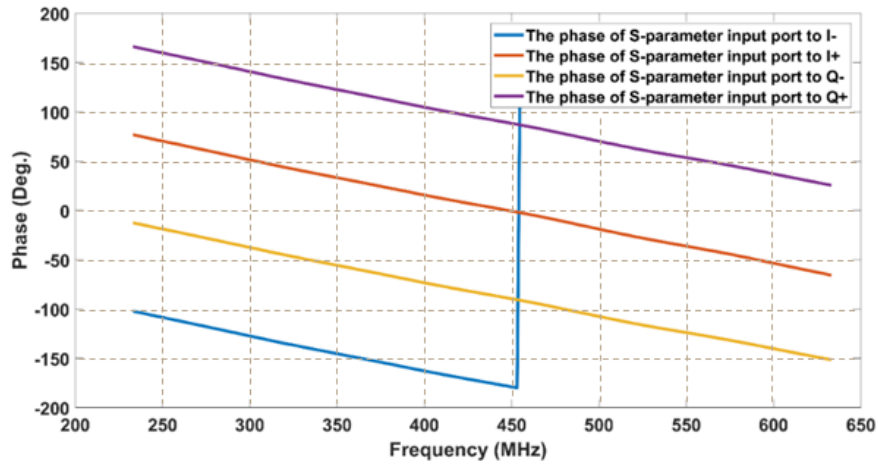


Figure 4.18 Phase difference between input and quadrature outputs on I/Q power divider board

The phase difference measured between the input and Q+, Q-, I+, I- ports of the fabricated I/Q power divider are 93.8, -84.14, 4.87, and -173.5 degrees, respectively. Thus, an approximately 90-degree phase difference is achieved between the Q and I signals.

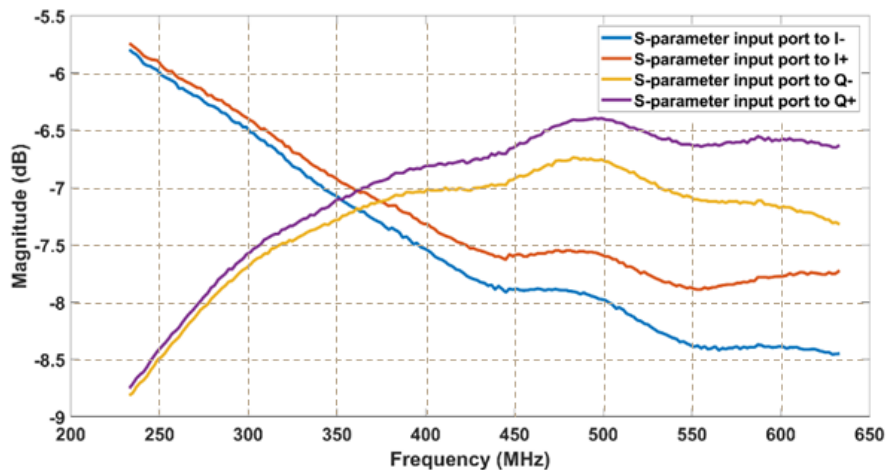


Figure 4.19 Magnitude of S-parameters from input to each quadrature outputs on I/Q power divider

The signal at the input is weakened by 6.74 dB at Q+ output, 6.99 dB at Q- output, 7.561 dB at I+ output, and 7.83 dB at I- output. These values correspond to the insertion loss between input and output ports. Since the signal is divided into 4, the loss of 6 dB must be there. The measured values are higher than 6 dB due to an imbalance between output ports of the deployed components on the board and additional board losses.

### 4.3.3.2 Measurement Results for Up-Converter Block

All system modules are brought together, and the board loss measured from the input of the I/Q modulator to the output of the ADRF6720-27-EVALZ evaluation board. A 433 MHz RF signal provided to the input of the block, passes through I/Q power divider, bias tee and ADRF6720-27-EVALZ and up-converted to 1575.42 MHz. It is important to know the loss of the circuit. Connections between the I/Q power divider board and bias tees are provided by Crystek Company's CCSMA18-MM-141-5 manufacturer coded 5-inch-long coaxial cables. Connections between the RF+DC output of the bias tees and the I +, I-, Q +, Q- RF inputs of the ADRF6720-27-EVALZ are provided by Crystek Corporation's CCSMA18-MM-141-4 manufacturer coded 4-inch long coaxial cables. The complete up-converter is shown in Figure 4.20.

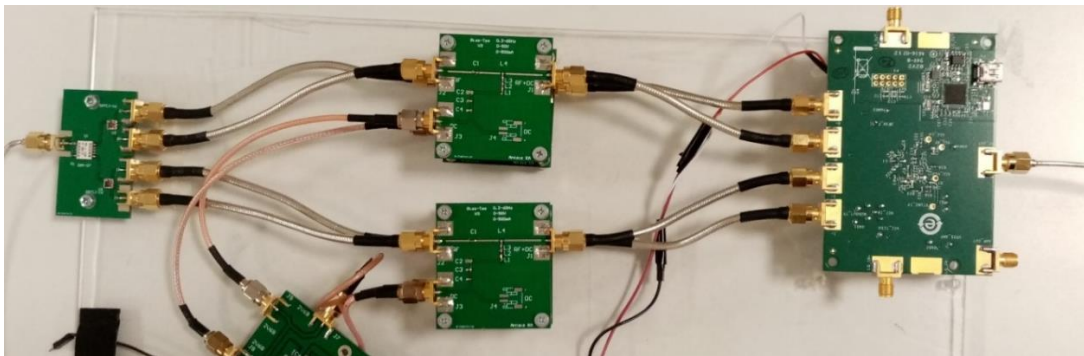


Figure 4.20 Complete up-converter block with I/Q power combiner, bias tees and ADRF6720-27 from left to right

The register sets of ADRF6720-27 are set with the optimized values for each parameter. The measurement is carried out with Rohde & Schwarz FSH8 Spectrum Analyzer and Agilent E4437B ESG-DP Serial Digital RF Signal Generator. The input signal at 433 MHz has -21.1 dBm power. The output power is measured through a coaxial cable with a loss of 0.6 dB. In this case, the power level measured at the output of this block is provided in Figure 4.21. The power level at the output is measured as -22.9 dB.

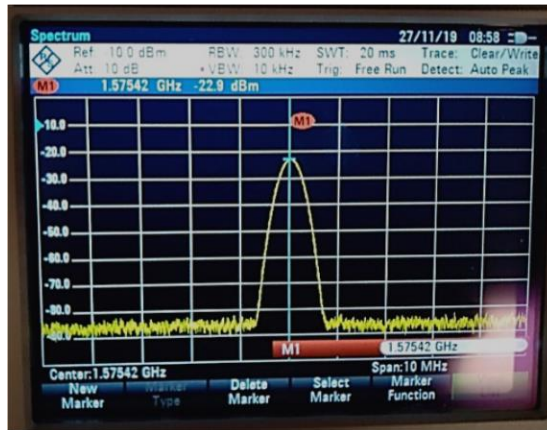


Figure 4.21 Signal power measured at the output of the up-converter block when the input signal is -21.1 dBm

Therefore, the output power at the output port of block is -22.3 dB, excluding the connection cable from the up-converter to the spectrum analyzer. Given that the input power is -21.1 dBm and output power is -22.3 dBm, the loss of the up-converter block is found to be 1.2 dB. This loss is due to board and cable losses and conversion gain/loss on the ADRF6720-27 evaluation board.

#### 4.4 Off-the-shelf GPS Receiver

Ublox EVK-M8T evaluation kit is used to decode GPS signals provided by the up-converter. This kit features sophisticated RF architecture and anti-interference technology to provide the highest performance with u-blox NEO-M8T positioning technology. This receiver has a dual-frequency RF frontend that can receive GLONASS, Galileo, BeiDou, QZss, and SBAS signals.

The selected GPS receiver is supported by the GNSS evaluation software “U-Center”. This software is used to control the entire Ublox kit and to view the receiver location, Doppler effects calculated by Ublox, pseudo ranges from each satellite, satellite positions,

C/N ratio for signals received from each satellite, and so on. The user interface and off-the-shelf receiver are shown in Figure 4.22.

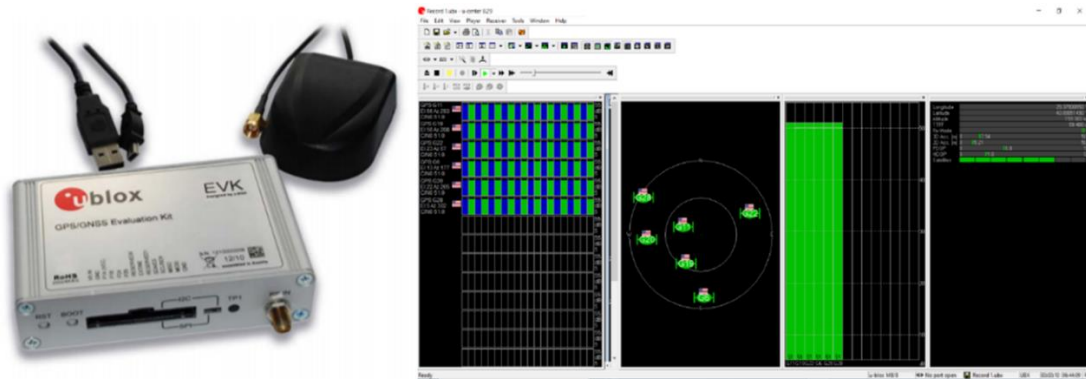


Figure 4.22 EVK-M8T evaluation kit and u-Center 8.29 interface

#### 4.5 Voltage Regulator for Receiver Hardware

This block is a supporting block in the receiver hardware and similar to the voltage regulator block of the receiver hardware. The RF signal does not pass through this block, therefore, in this thesis, this block is referred to as a support block that provides DC voltages to the signal power conditioner and filter block and up-converter block. ADRF6720-EVALZ requires 3.3 V DC and 2.68 V at I/Q RF inputs. TB-DAT31R5A-SP+ attenuator requires 3.3 V, and TB-1063-13LN+ LNAs requires 5 V DC. All these requirements are met by the voltage regulator for receiver hardware. Among these voltages, 2.68 V for each I/Q rf input is supplied from voltage regulators over bias tees to the ADRF6720-27-EVALZ.

Fabricated voltage regulator for repeater hardware is demonstrated in Figure 4.23.

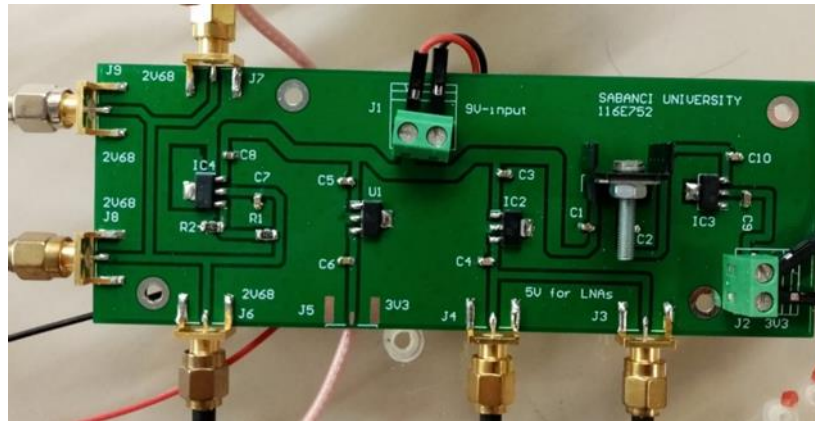


Figure 4.23 Voltage regulator for receiver hardware

The linear voltage regulator chips used for the receiver hardware’s voltage regulator block are presented in Table 4.4. These components are selected considering thermal design terms and equations presented in [92].

Table 4.4 Circuit boards and Linear voltage regulator chips used to supply them with the required input voltage

Selected Regulator	Input Voltage	Output Voltage	The module to which the selected chip supplies DC Voltage
<b>L7806</b>	9 V	6 V	LD1117AS33TR voltage regulator
<b>LD1117AS33TR</b>	9V	3.3V	ADRF6720-27-EVALZ Evaluation Board
<b>UA78M05CDYRG3</b>	9 V	5 V	2x LNA TB-1063-13LN+
<b>UA78M33CDYR</b>	9 V	3.3 V	Attenuator TB-DAT31R5A-SP+
<b>AMS1117ADJ</b>	9 V	2.68 V	Bias Tee (for ADRF6720-27 RF Inputs)

The selection of these chips with thermal design considerations, schematic, and layout of the fabricated voltage regulator board are provided with more detail in Appendix B.

In the voltage regulator block of the receiver and repeater hardware, the same linear voltage regulator chips for the same output voltages are used. The required voltages in

the programmer/Controller over Wi-Fi block have been met within its design and the regulator chips on itself.

## **4.6 Programmer and Controller over Wi-Fi**

In this section, the programmer and controller over the Wi-Fi block design is explained in detail. This block is common in both repeater and receiver hardware as mentioned under Chapter 3. This block is responsible for programming and setting ADRF6720-27 registers that are optimized for up-conversion of 433 MHz GPS signals back to 1575.42 MHz. This block also sets different attenuation values by controlling DAT-31R5A-SP+. These two functions are used in both repeater and receiver. Besides, in the receiver hardware data transfer from the off-the-shelf GPS receiver EVK-M8T kit is possible through this block. Raw data retrieved from the off-the-shelf receiver indoors can also be transferred to a central computer over wi-fi.

### **4.6.1 Programmer and Controller Design and Fabrication**

This block is designed in line with the needs of the down-converter and up-converter blocks, attenuator settings, and GPS data transfer from the receiver to a computer. This block contains the ESP8266 module, STM32F102 MCU, and voltage regulators. ESP8266 acts as a wifi-UART bridge. STM32F102 programs ADRF6820/6720-27 and controls DAT-31R5A-SP + over SPI. The block architecture is shown in Figure 4.24.

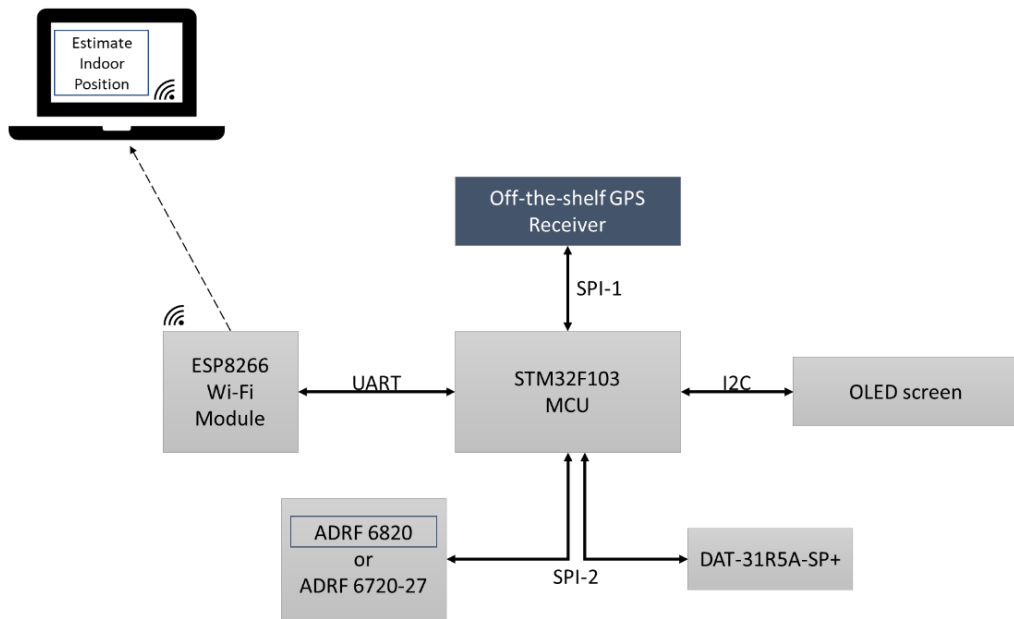


Figure 4.24 Architecture of the programmer and controller block

The experimental setup of the system depicted in Figure 4.24 is set up as shown in Figure 4.25. Esp-link software is installed on Nodemcu, ESP8266. Network and IP settings are done and the TCP client code is written on MATLAB. EVK-M8T GPS kit is tested with the u-Center program and SPI is set as the serial communication unit. UBX format is chosen instead of the NMEA format for the EVK-M8T kit.

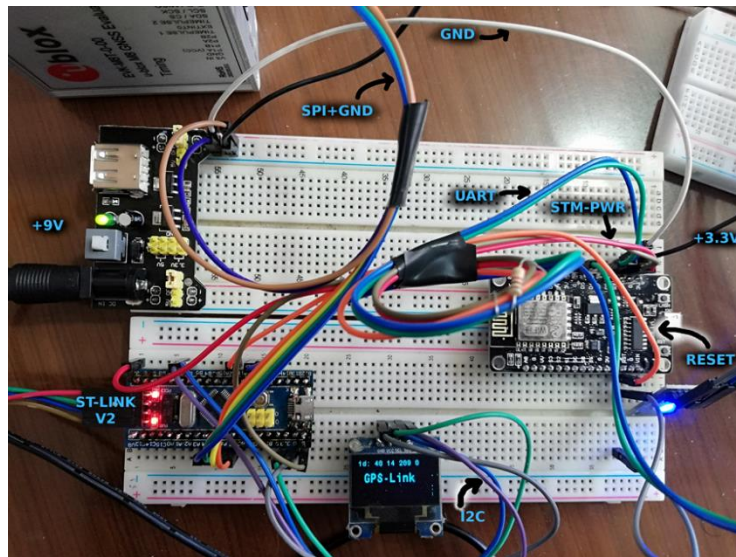


Figure 4.25 Experimental setup of Programmer and Controller Block

Nodemcu is used as a server connected to Wi-Fi. The message packets from the central computer are sent to ESP8266 which is connected to wi-fi, and from ESP8266 to STM32F103 via UART. Therefore, the ESP8266 module is used for the WiFi-UART bridge. Depending on the type of packages coming to STM32, a suitable package is sent to the target device from STM32 by switching between SPI-1 and SPI-2.

As a result, a bridging is developed that parses the message packets coming from the user interface (GUI) developed on MATLAB and sends them to the appropriate device.

After the experimental circuit operation is verified, the pin diagram is drawn and the schematic design of the circuit is completed. The schematic design of the programmer and controller block is presented in Figure 4.26.

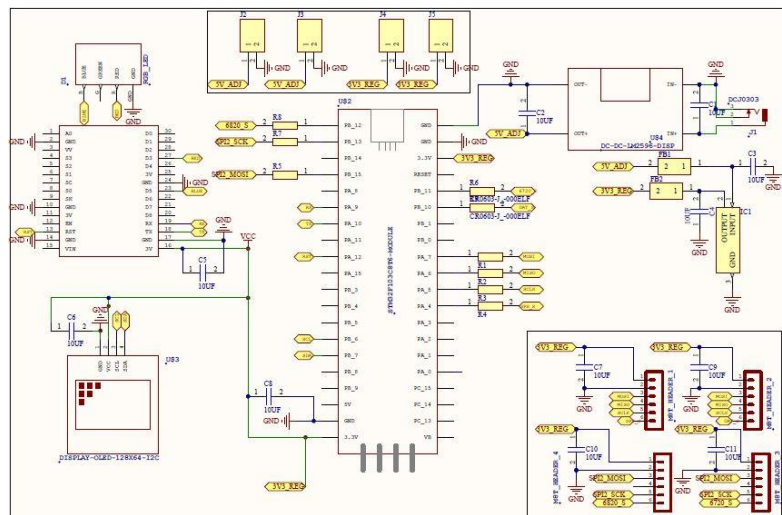


Figure 4.26 The schematic design of the programmer and controller block

After the schematic design is checked and verified, its layout is carried out in order to fabricate the circuit board. The layout of the circuit is shown in Figure 4.27. The circuit board is fabricated according to the given layout and the components are integrated. After STM32 MCU and ESP8266 nodemcu are programmed, the DC input is supplied. The fabricated control card is shown in Figure 4.28. In this way, a control block, which carries

out the programming of the modules in the receiver and repeater and transfers the GPS data, has been realized.

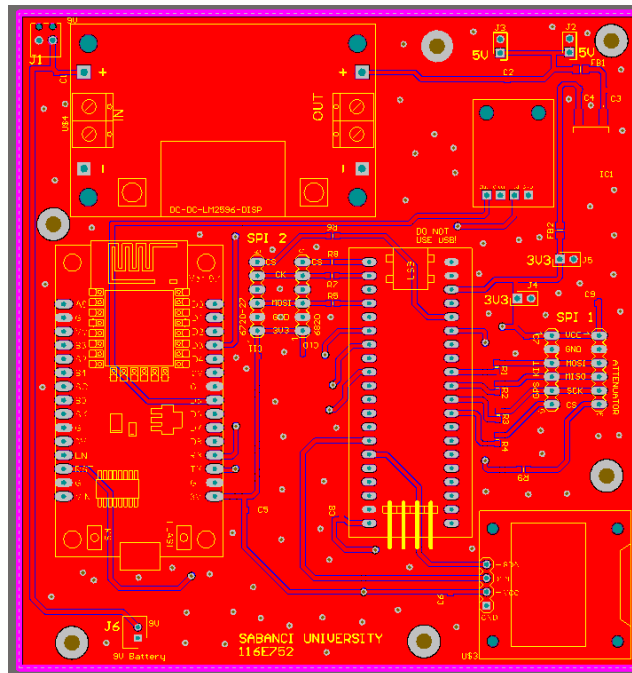


Figure 4.27 The layout of the programmer and controller block

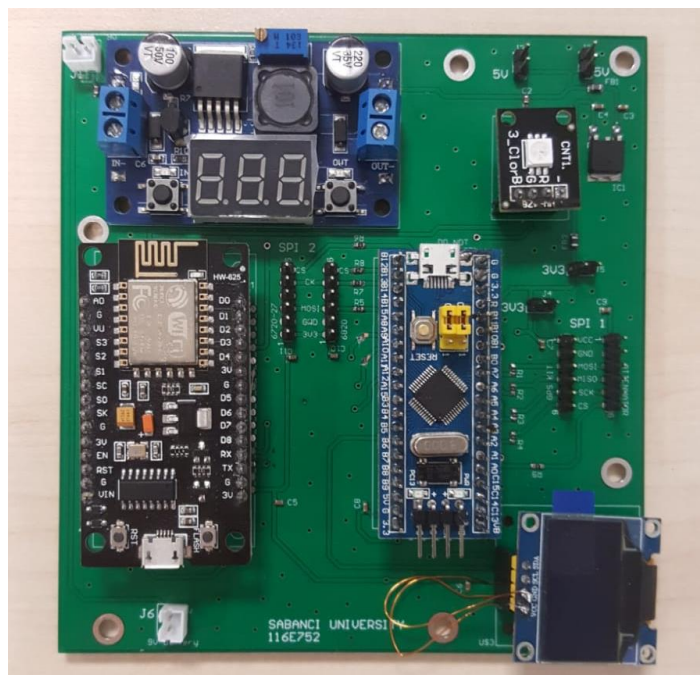


Figure 4.28 Fabricated programmer and control block

The OLED connections are reversed by cabling as the layout of the component does not match with the received component.

#### **4.6.2 Programmer and Controller Block Tests**

In this section, the test results of the programmer and controller block for programming ADRF6820-EVALZ card and controlling DAT-31R5A-SP+ digital attenuator are provided. The tests for ADRF6720-27-EVALZ is excluded as it is programmed in a very similar way. The only difference is in the register sets.

ADRF6820-EVALZ functions in the frequency down-converter block. While testing the programmer and controller block, 6 V DC voltage is provided to the ADRF6820-EVALZ board with current limited at 450 mA. Also, while changing the settings of ADRF6820 with the optimized values, the bit values in every register set are checked.

Then the steps listed below are followed to program ADRF6820:

1. USB-ADRF6820 communication during ADRF6820-EVALZ is being programmed using a computer and customer software is viewed and recorded with Logic analyzer as seen in Figure 4.29.

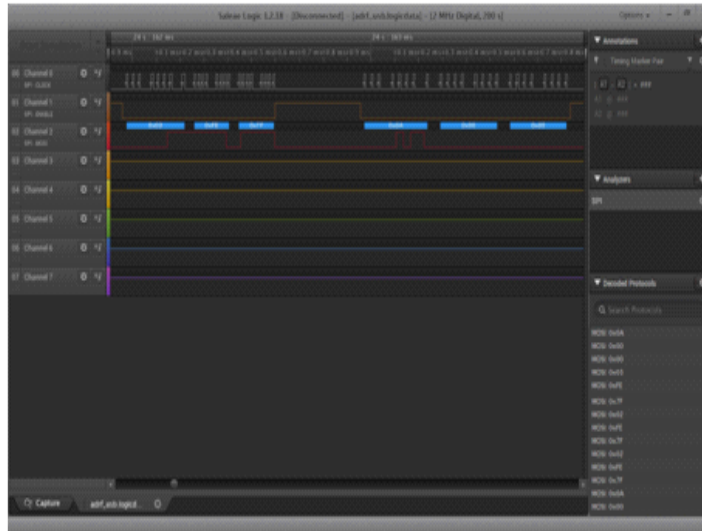


Figure 4.29 USB-ADRF6820 communication viewed by a logic analyzer

2. When ADRF 6820 Customer Evaluation software programs the ADRF6820-EVALZ, incoming and outgoing packets have been listened with a logic analyzer. These messages are added to prepared STM32 software.
3. The USB interface on the ADRF6820-EVALZ evaluation board is disconnected by removing the resistors R9, R10, and R24 0 ohms.
4. The register reading and writing operations of ADRF6820 is carried out healthily with STM32.
5. The required register values for the optimized values in the repeated hardware design are added to the STM32 software and the ADRF6820 chip is programmed according to these register sets over SPI.
6. After the ADRF6820 chip is programmed over SPI by the programmer and controller block, all registers of ADRF6820 are read for checking if all the register set values are written correctly. As a result of the reading operation, it is determined that the written values are set correctly for optimized settings. The register sets for the optimized settings after programming with the fabricated programmer and controller block are read and demonstrated in Figure 4.30.

Name	Value	Type
sBuffToTxCnt	<cannot evaluate>	uchar
sRxBuff	<cannot evaluate>	uchar
sRxBuff	<cannot evaluate>	uchar
adrf6820	0x20000068 &adrf6820	struct ADRFData
reg01	0xFE7F	ushort
reg02	0x0034	ushort
reg03	0x0889	ushort
reg04	0x0F00	ushort
reg10	0xFE7F	ushort
reg20	0x0C26	ushort
reg21	0x0009	ushort
reg22	0x0002	ushort
reg23	0x0000	ushort
reg30	0x0022	ushort
reg31	0x1525	ushort
reg32	0x09F3	ushort
reg33	0x1702	ushort
reg34	0x0E00	ushort
reg40	0x0030	ushort
reg42	0x000E	ushort
reg43	0x0001	ushort
reg44	0x0002	ushort
reg45	0x0000	ushort
reg46	0x0010	ushort
reg47	0x0000	ushort
reg48	0x0000	ushort
reg49	0x16BD	ushort
reg60	0x0000	ushort
reg7E	0x0002	ushort
reg7F	0x1003	ushort

Figure 4.30 Register sets for the optimized settings are read from ADRF6820 after programming with realized programmer and controller block

7. The same 6 steps described above followed for ADRF6720-27-EVALZ.
8. Both ADRF6820-EVALZ and ADRF6720-27 boards are programmed correctly with the programmer and controller board.

The designed controller and programmer board is capable of controlling the attenuation in the signal power conditioner and filter blocks in both repeater and receiver hardwares. Thus, the amplification level of the RF signal can be varied as explained previously. DAT-31R5A-SP + digital step attenuator provides attenuation in RF signal from 0 dB to 31.5 dB with 0.5 dB step size.

According to the data provided for DAT-31R5A-SP+ in its datasheet, communication pins and functions are defined on STM32 (Figure 4.31). The connections over the serial interface of the attenuator are completed and tests are performed for each attenuation level

from 0 dB to 31.5 dB. According to the test results, the attenuator is successfully programmed. One of the measurement S21 results for the attenuator module is provided in Figure 4.32 when the attenuation is set to 8 dB using the programmer and controller block.

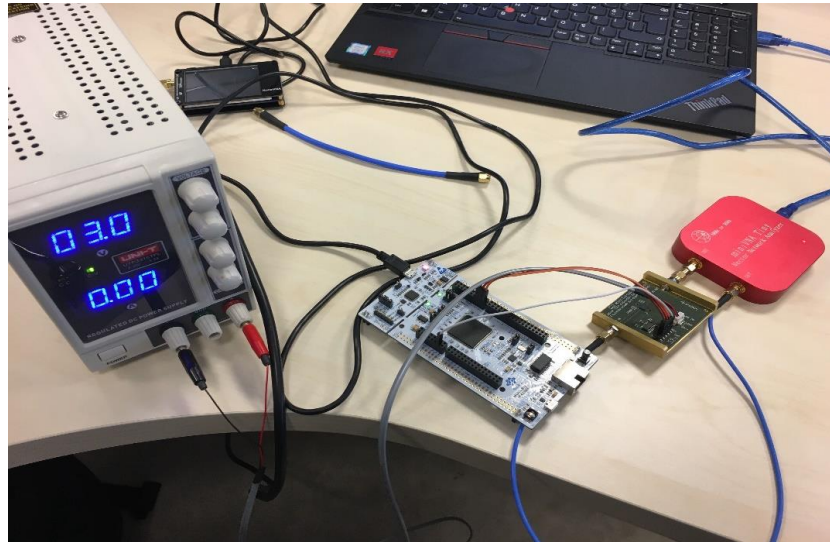


Figure 4.31 Testing written software code on the attenuator

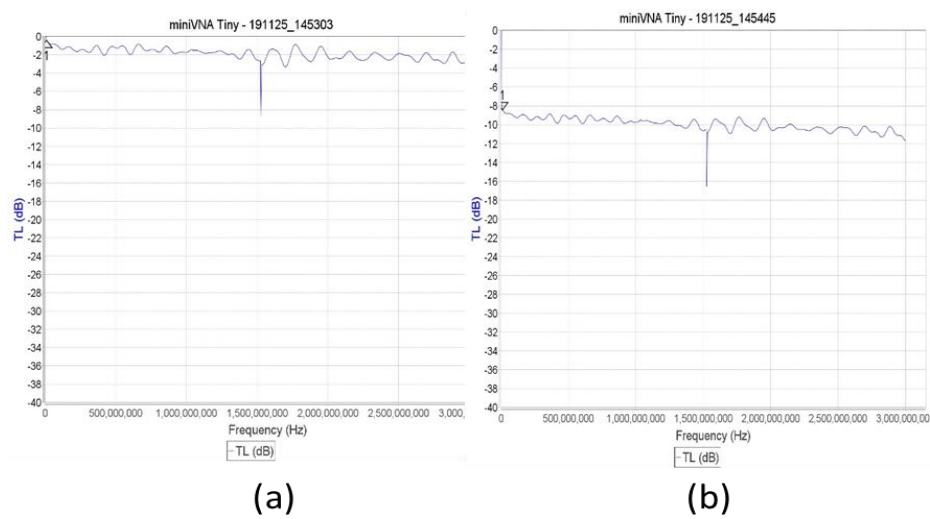


Figure 4.32 (a) Measurement with 0 dB attenuation and (b) Measurement with 8 dB attenuation after setting with programmer and controller block

Thus, the attenuator module has also been successfully programmed with the programmer and controller block.

## **CHAPTER 5 MEASUREMENT OF INDOOR POSITIONING SYSTEM**

The previous chapters describe the indoor positioning system that consists of the repeater and the receiver hardware. The repeater and receiver hardware are explained with details in chapters 3 and 4, respectively.

In this chapter, both receiver and repeater hardware are used for several tests and measurements. First of all, all system modules and blocks are tested together. The loss of each repeater and receiver hardware measured from input to output. The loss of each module and block is also measured.

Then, a repeater and receiver are brought together with an RF cable. A measurement from the input of the system to the output of the system is carried out to check if GPS signal integrity is preserved after down and up-conversion and amplification. After boards are tested by connecting an RF cable in between a repeater and receiver, it is concluded that a GPS signal transmitted within down-conversion and up-conversion scheme still preserves its integrity so that such a system can be used to determine the position.

Finally, 1D indoor positioning is achieved with 2 repeaters and 1 receiver. During measurements, it is noticed that the carrier to noise ratio (CNO) of the retransmitted signals changes in the off-the-shelf receiver. It is observed that, when the CNO ratio is

maximized at the output of repeater(s), the position of the receiver in terms of the distance to each repeater is found accurately.

## **5.1 End-to-end loss measurements in Repeater and Receiver Boards**

In this section, the loss of the signal power has been measured from input to the output of both repeater and receiver hardware separately. Then, connecting a repeater with a receiver with an RF cable, the end-to-end power measurements are carried out for the calculation of the overall board loss. Then, a GPS signal with a known power is provided to the input of the repeater by a GPS signal generator. The power level of the GPS signal is measured at the output of some modules and the output port of the receiver hardware. Thus, the effects of the modules and blocks formed in Chapter 3 and 4 on a GPS signal is observed.

The power levels between two consecutive modules in the repeater hardware are measured first. From these measurements, each module's gain and loss have been calculated. A signal with the input frequency of 1575.42 MHz is down-converted to 433 MHz with the frequency down-converter block on the repeater side. Power level measurements on the transmitter demo system are carried out with the Rohde & Schwarz FSH8 Spectrum Analyzer and Agilent E4437B ESG-DP Serial Digital RF Signal Generator.

An input signal of -21.7 dBm at the input of the down-converter at 1575.42 MHz is supplied by the signal generator. The signal is not provided using bias tee as its loss is very low and due to the protection purposes of the signal generator. The power levels at each module's input and output for the repeater are given in Figure 5.1.

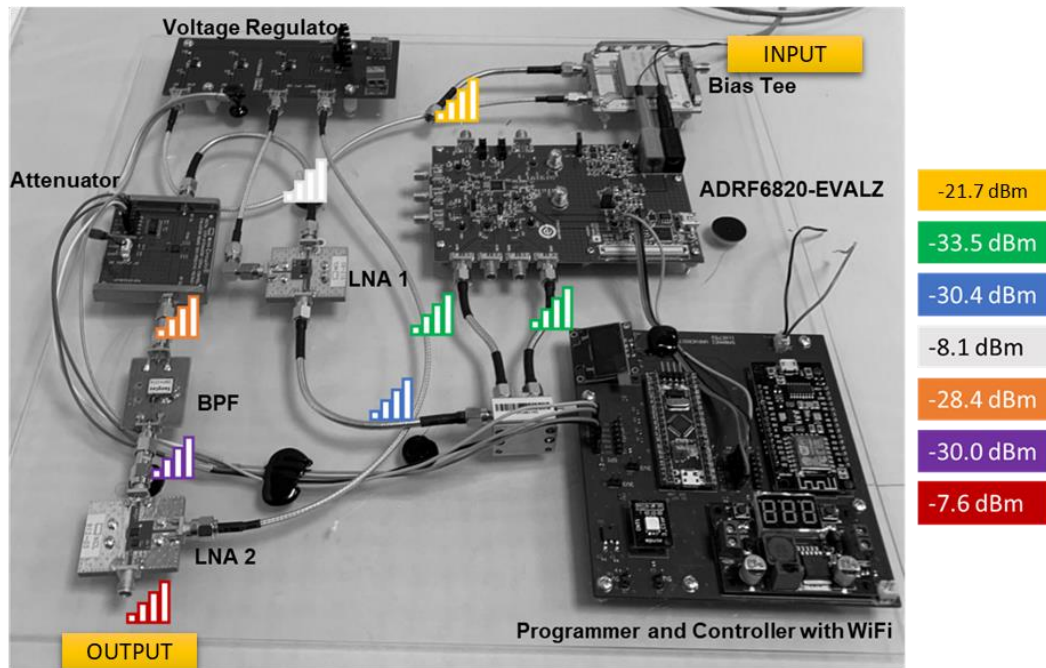


Figure 5.1 Signal power levels between modules of the repeater

Measured power levels and calculated the loss or gain of each module is summarized as follows:

- According to the measurement results, the signal at the frequency of 1576.42 MHz, whose input level is -21.7 dBm, is down-converted to 433 MHz at the I + and Q + outputs of the ADRF6820-EVALZ board, and the power level of the signal drops to -33.5 dBm at each output of the ADRF6820-EVALZ.
- I+ and Q+ signals are summed by a 90-degree hybrid combiner and the signal power level rises to -30.3 dBm as a result of the summation. One should conclude that the down-converter block has a loss of 8.7 dB ( $-21.7 - (-30.4) = 8.7$ ). as previous block-level measurements have also proven.
- The power at the output of the low-noise amplifier following the 90-degree power combiner is measured as -8.1 dBm. Therefore, the gain of the amplifier is 22.3 dB ( $-30.4 - (-8.1) = 22.3$ ). This result is in line with the S-parameter measurements of the low-noise amplifier.

- The attenuation is set as 20 dB. Due to the 20 dB of attenuation, the signal power level drops to -28.4 dBm at the output of the digital step attenuator. The additional 0.3 dB of loss is due to cable losses and insertion loss.
- The power level of the signal at 433 MHz is measured as -30.0 dBm at the output of the subsequent band pass filter. Therefore, the insertion loss of the filter is 1.6 dB ( $-28.4 - (-30.0) = 1.6$ ). This result is in line with the S-parameter measurement of the filter.
- The power of the 433 MHz signal is measured as -7.6 dBm at the output of the last low noise amplifier. Therefore, its gain is 22.4 dB ( $-30.0 - (-7.6) = 22.4$ ). This result is compatible with S-parameter measurement results.

Consequently, the repeated system performs frequency down-conversion as expected when the system modules are brought together. The signal power has also been regulated as expected.

Secondly, the signal power at the input and output of each module in the receiver hardware is measured to calculate the loss and gain of the modules that contribute to the overall gain and loss of receiver hardware. Power level measurements on the repeater are carried out with the Rohde & Schwarz FSH8 Spectrum Analyzer and Agilent E4437B ESG-DP Serial Digital RF Signal Generator.

An RF signal whose frequency is 433 MHz is fed to the receiver with -21.7 dBm power. The power levels at each module's input and output for the repeater are given in Figure 5.2.

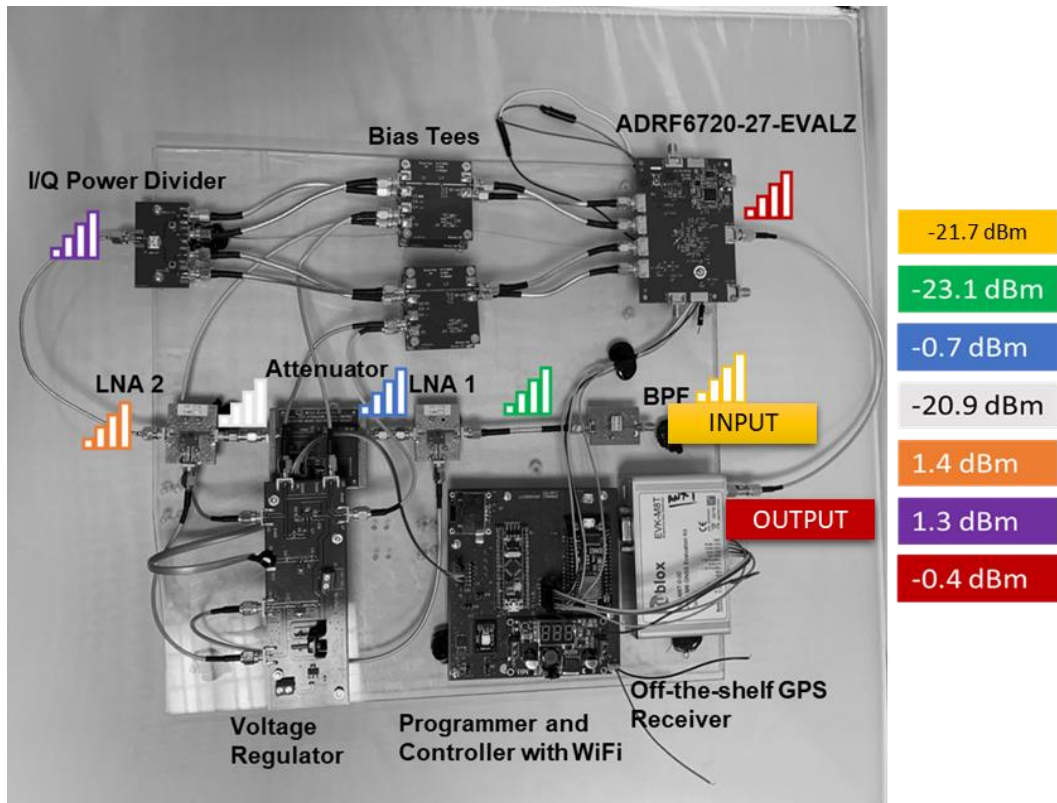


Figure 5.2 Signal power levels between modules of the receiver

.Measured power level and calculated the loss or gain of each module is summarized as follows:

- The signal with a power level of -21.7 dBm is given to the first module, the filter, input and the measured power level at the output of the filter is -23.1 dBm. Therefore, the loss of the filter is calculated as 1.4 dB  $(-21.7 - (-23.1))$ . At this point, there is a difference of 0.2 dB from the S-parameter measurement. However, this variation from the measured value may be due to the fact that the filters are soldered onto the in-house fabricated boards.
- At the output of the low noise amplifier, the signal power level is measured as -0.7 dBm. The gain of the amplifier used here is calculated as 22.4 dB as expected  $(-0.7 - (-23.1) = 22.4)$ .
- There is a digital step attenuator set to 20 dB attenuation after the low noise amplifier. At the output of the attenuator, the power level of the signal drops to -

20.9 dBm. The variation of 0.2 dB may derive from the connections between the modules and the spectrum analyzer.

- At the output of the low noise amplifier following the digital step attenuator, the power level is measured as 1.4 dBm. The gain of the amplifier located here is found as 22.3 dB ( $1.4 - (-20.9) = 22.3$ ).
- Then, a connection to the signal power conditioner and filter block is provided by an RF cable. Due to this connection, the signal level coming to the frequency amplification and filtering block is 1.3 dBm.
- The power level at up-converter output, which operates with very little loss, is -0.4 dBm. Therefore, the power loss in this block is calculated as 1.7 dB ( $1.3 - (-0.4) = 1.7$ ). In chapter 4, the loss in this block has been found as 1.2 dB. However, connections have been varied in this measurement and 0.5 dB derivation from different measurements can be viewed as an error margin.

In Chapters 3 and 4, the repeater and the receiver sides are explained with the novelty of the approach being the propagation of GPS signals in the 433 MHz ISM band. In the third measurement, GPS signal at 1575.42 MHz with -81.6 dBm power is supplied to the input of the repeater from the Rohde & Schwarz SMBV100A vector signal generator. The output signal power is measured with Rohde & Schwarz FSH8 Spectrum Analyzer for 300 kHz resolution and 20 MHz channel bandwidth. The measurement setup is shown in Figure 5.3.

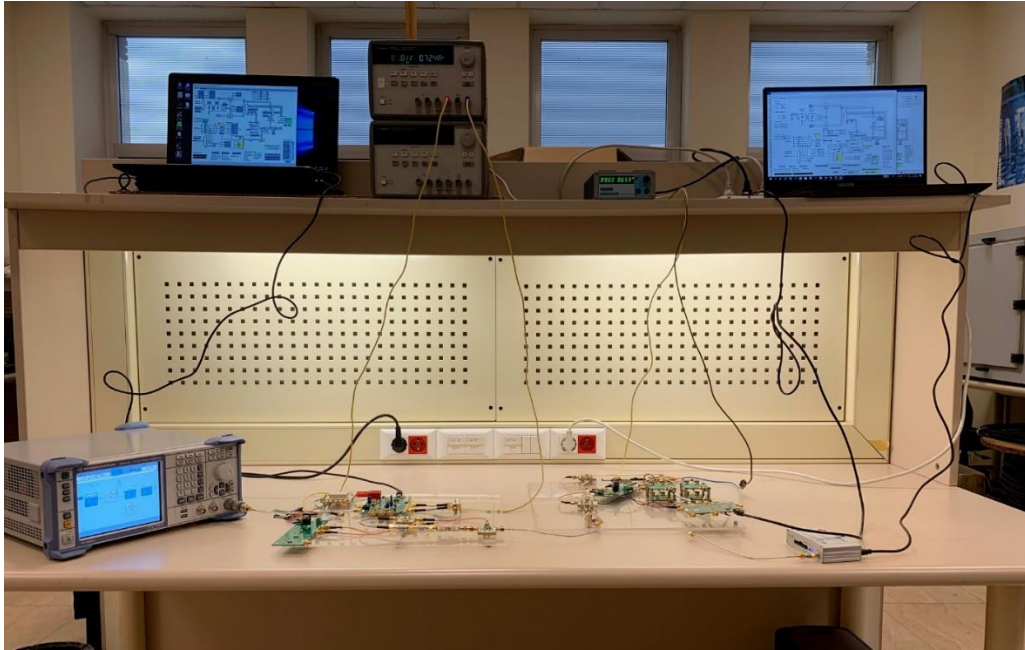


Figure 5.3 End-to-end power measurement of GPS signals in the designed system

During this measurement, the controller and programmer boards and digital step attenuators have been excluded as the integration of these modules has not been fully developed at that stage of the measurement. Instead, 2 computers to program up and down-converters and 20 dB fixed attenuators to mimic the digital step attenuator is deployed. The off-the-shelf receiver is connected to the output of the receiver. MATLAB® software is run on one of the computers to collect the raw data from the off-the-shelf receiver. The DC voltage of 9V is supplied to the voltage regulators.

In this test, the frequency of the GPS signal given from the GPS signal generator is 1575.42 MHz. GPS signal from the GPS signal generator is down-converted in the repeater and changed to 433 MHz. The signal is then amplified passing through the cascaded LNA, 20-dB attenuator, BPF, and LNA modules. Effectively, the power of the signal is amplified by only 1 LNA while the gain of the other amplifier is neutralized by balancing the filter's insertion loss and attenuation introduced. The GPS signal, whose frequency is down-converted to 433 MHz in the repeater system, is connected to the receiver circuit via an RF cable.

GPS signal at 433 MHz has passed through the filter, LNA, 20 dB power attenuator and LNA, respectively, and amplified. This signal is then up-converted back into the frequency of 1575.42 MHz by the frequency up-converter. The uBlox GPS evaluation kit is deployed at the end of the receiver. RF repeater and receiver with off-the-shelf GPS receiver, connections between modules, and the path that GPS signals followed from the GPS signal generator to the GPS evaluation kit through designed hardwares, excluding controller and programmer board and the digital step attenuator, are shown and indicated by arrows in Figure 5.4.

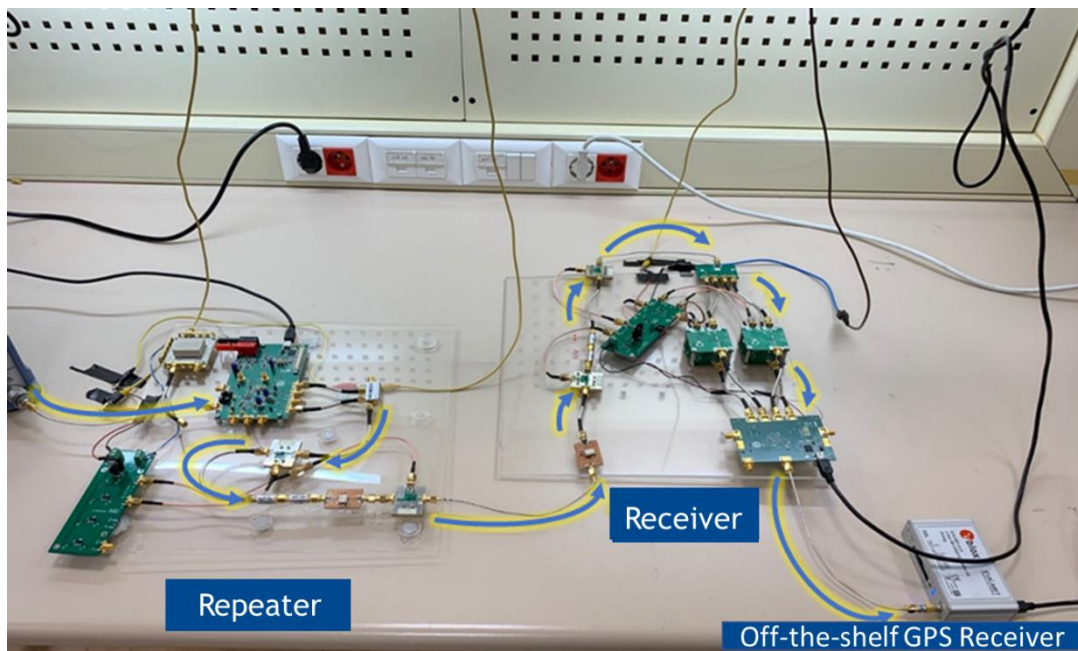


Figure 5.4 One of the repeaters and the receiver hardware for indoor positioning system based on down and up-conversion of GPS signals

In this test, the power of the GPS signal is set as  $-80$  dBm in the GPS signal generator. The resolution bandwidth of the spectrum analyzer is set to 300 kHz (RBW = 300 kHz). The channel bandwidth is set to 20 MHz, and power within this bandwidth is measured.

GPS signal at the output of the GPS signal generator is measured and shown in Figure 5.5.



Figure 5.5 GPS signal supplied to the system input from the GPS signal generator

The GPS signal is measured at the output of the repeater hardware. The GPS signal level at 433 MHz frequency is shown in Figure 5.6. The power of the down-converted GPS signal measured within 20 MHz bandwidth is -66.7 dBm.



Figure 5.6 Power of the down-converted GPS signal at the output of the repeater

The GPS signal power at the frequency of 1575.42 MHz is measured as -45.9 dBm in 20 MHz bandwidth. The measurement result is presented in Figure 5.7.



Figure 5.7 Power of the GPS signal after up-conversion at the output of the receiver hardware

The measurement results are summarized in Table 5.1. Using the measured power value and peak power spectral density values, the power level at the peak in the 300 kHz bandwidth resolution was calculated and is also given in Table 5.1.

Table 5.1 End-to-end measurement results with GPS signal generator

Measured Output	Power Levels		
	<i>Power over 20 MHz channel (dBm)</i>	<i>Peak (dBm/Hz)</i>	<i>Gain (dB)</i>
<b>Signal Generator</b>	-81.6	-144.3	-
<b>Repeater with 20 dB attenuator</b>	-66.7	-131.8	14.9
<b>Receiver with 20 dB attenuator</b>	-45.9	-111.3	20.8

## 5.2 Evaluating the Effect of Down and Up-Conversion Method on GPS Signals

The same setup presented in the previous section in Figure 5.4 has been used with GPS signal generator input of -100 dBm. In the real world, GPS signals reach at around -100

dBm to the input of the down-converter block after passing through the directional active GPS antennas. Therefore, the power of GPS signals from a GPS signal generator is set to -100 dBm. In this measurement, the aim is to show the effect of deploying such hardware between a GPS antenna and an off-the-shelf receiver.

Firstly, the location information provided by the GPS signal generator is recorded as the reference point. Then the GPS signal generator is directly connected to the off-the-shelf GPS receiver. The latitude and longitude information from the positioning signal provided by the GPS signal generator is decoded by the off-the-shelf receiver and recorded.

Then the repeater and receiver hardware are deployed as shown in Figure 5.4 between GPS signal generator and off-the-shelf receiver. The attenuators of 20 dB are used in both repeater and receiver. The raw data from the off-the-shelf receiver has been recorded and stored in MATLAB®. When the GPS signal level is -100 dBm at the input of the system shown in Figure 5.4, the estimated location using the algorithms in [4] is found. The results are presented in Figure 5.8.

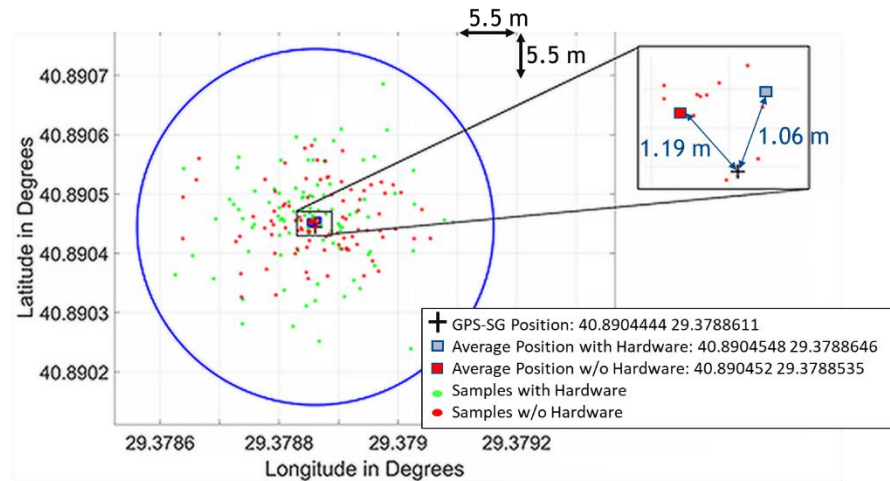


Figure 5.8 Performance of the proposed repeater and receiver hardware along with the positioning algorithms on GPS signals

The estimated location with repeater and receiver hardware is signified with the green stars. The center of the circle is the reference location provided by the GPS signal

generator. The red stars represent the location found when the GPS signal generator is connected directly to the off-the-shelf GPS receiver.

With hardware, the circular error probable is 8.53 meters from the estimated average position while it is 8.97 meters from the position provided by GPS signal. Distance from each point to the estimated average position and the position provided by GPS signals are shown in Figure 5.9 and Figure 5.10.

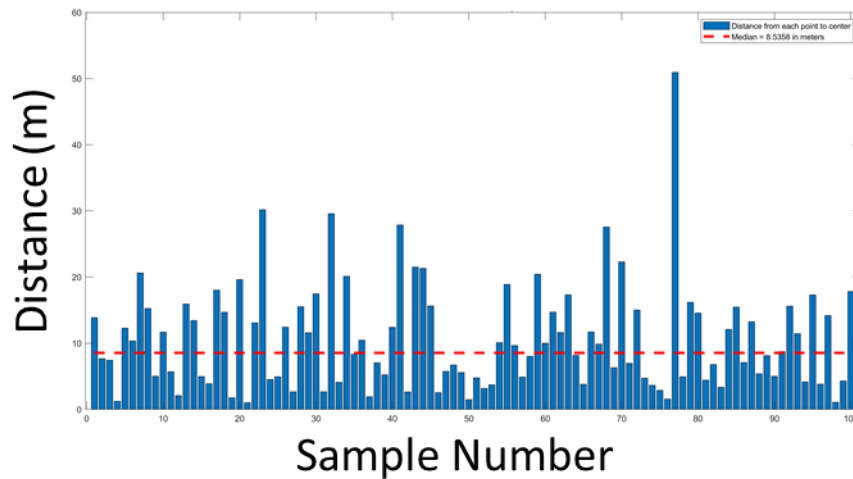


Figure 5.9 Distance of each sample to the average estimated position when the receiver and repeater hardware are inserted between the GPS signal generator and off-the-shelf receiver

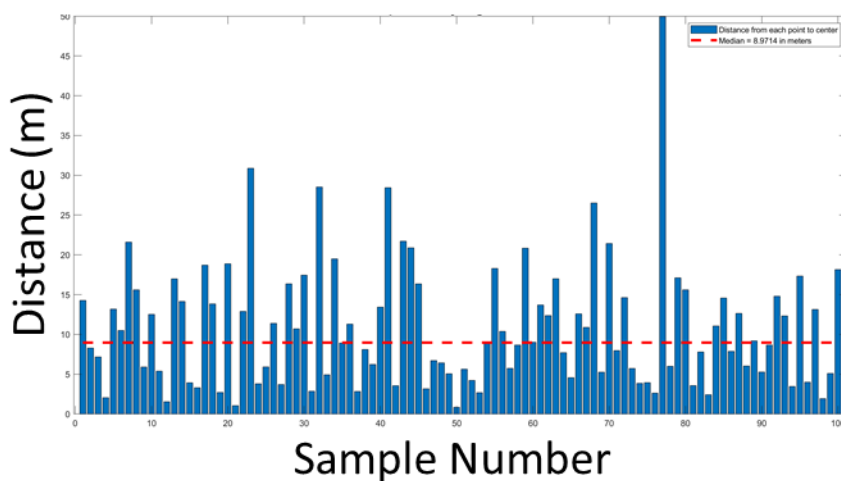


Figure 5.10 Distance of each sample to the reference position provided by the GPS signal generator when the receiver and repeater hardware are inserted between the GPS signal generator and off-the-shelf receiver

Averaging over 100 samples, the error obtained with and without hardware are 106 cm and 119 cm, respectively. The obtained results are summarized in Table 5.2.

	<i>Latitude</i>	<i>Longitude</i>	<i>Distance from the reference</i>
<b>Reference</b>	40.8904444	29.3788611	0 cm
<b>without Hardware (average)</b>	40.8904548	29.3788646	119 cm
<b>with Hardware (average)</b>	40.8904520	29.3788535	106 cm

The difference between the estimated calculation with the insertion of repeater-receiver hardware and without the insertion of repeater-receiver hardware is only 39 cm. The locations with and without repeater-receiver hardware are shown on the map in Figure 5.11.



Figure 5.11 Estimated position with and without the repeater-receiver hardware

The proposed repeater and receiver system can be used for indoor applications as GPS signal integrity is preserved after passing through the system. It allows the use of

customary GPS receivers and existing algorithms in [4] with a modification to include NLOS effects. This system is not bounded by the regulatory framework for the use of GNSS repeaters as the system works at 433 MHz in the ISM band. Lower path loss that the signal is exposed is another advantage of the system.

### **5.3 1D Positioning**

1D positioning refers to the detection of receiver position with respect to only 2 repeaters located on the opposite sides of a linear path such as a long corridor. In this type of positioning, the location of the receiver is detected in terms of the distance between the receiver to the repeaters. To detect the exact location, one can use the triangulation method and 3 repeaters. Within the scope of this thesis, proof of 1D positioning is provided.

#### **5.3.1 1D Positioning Algorithm**

The MATLAB® algorithm of 1D positioning is based on the cancellation of the clock bias of the receiver as a single receiver is used for the reception of different GPS signals retransmitted simultaneously from 2 repeaters. Note that only 1 GPS satellite from each repeater is accepted for the position calculation by the receiver by selecting those satellites that are within the directional outdoor GPS antenna's viewing angles and having the best carrier to noise ratio.

Before starting the 1D positioning, the following 3 steps are completed to establish relations between the satellite and repeater positions:

- The satellite positions with the time solved are obtained correctly by connecting the off-the-shelf GPS receiver u-blox to outdoor GPS antennas.
- GPS repeaters are located on the two opposite sides of the indoor corridor. Each repeater position is noted.
- Then, with known GPS repeater positions and satellite positions, the difference between each satellite and repeater is calculated with the distance formula.

The workflow for 1D positioning algorithm is as follows:

Step 1: 1<sup>st</sup> repeater selects the satellites that are within the antenna view boundaries (Figure 5.12).

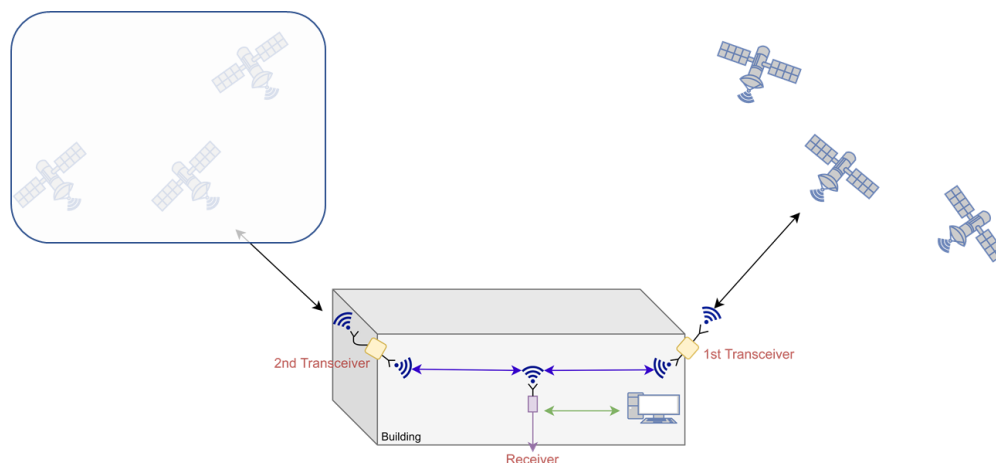


Figure 5.12 Satellites represented within the directional antenna's angle of view

Step 2: For the 1D positioning calculations, the satellite with the highest carrier to noise (CNO) ratio or closest to the beam center from that repeater is opted out in the algorithm (Figure 5.13).

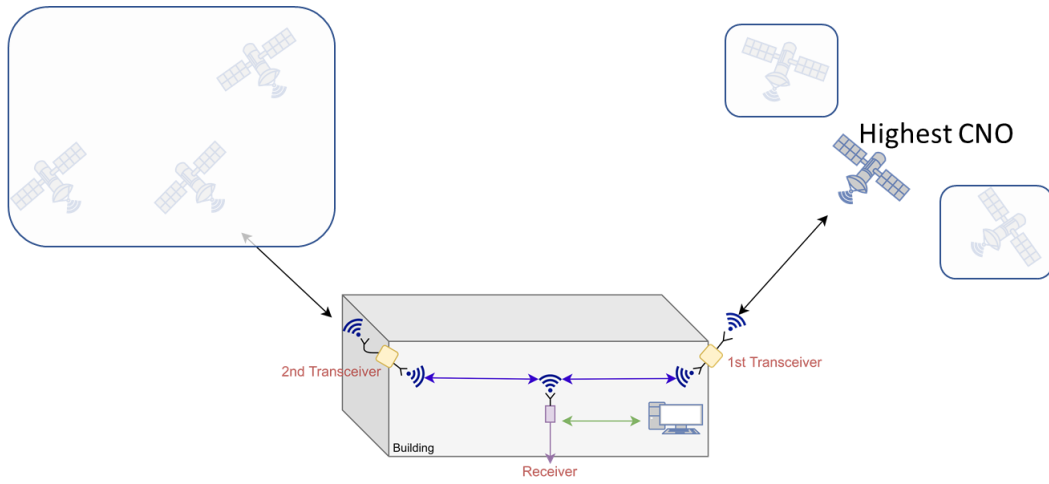


Figure 5.13 Satellite represented with the highest CNO in the directional antenna's angle of view

Step 3: Pseudorange PR1 is recorded (Figure 5.14).

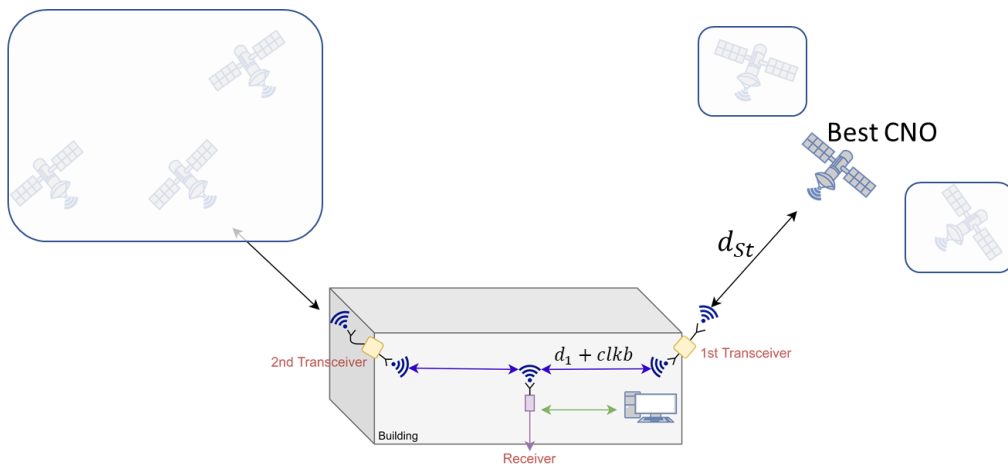


Figure 5.14 Terms contributing to measured pseudorange

The relation between PR1 and indoor distance ( $d_1$ ), clock bias ( $clkb$ ), and distance between repeater 1 and chosen satellite are given in Eq. 5.1.

$$PR1 = d_{st} + d_1 + clkb \quad (5.1)$$

where  $clk_b$  denotes the clock biases,  $d_1$  denotes the distance between 1<sup>st</sup> repeater and indoor receiver, and  $d_{st}$  denotes the distance between 1<sup>st</sup> repeater and the chosen satellite.  $d_{st}$  is calculated using the distance formula as both satellite and repeater positions are known.

Step 4: Calculated  $d_{st}$  is subtracted from measured pseudorange PR1. The resulting term PR1' is the summation of indoor distance  $d_1$  and clock bias term due to receiver as given in Eq. 5.2.

$$PR1' = PR1 - d_{st} = d_1 + clk_b \quad (5.2)$$

Step 5: The first 4 steps are repeated for 2<sup>nd</sup> repeater (Figure 5.15).

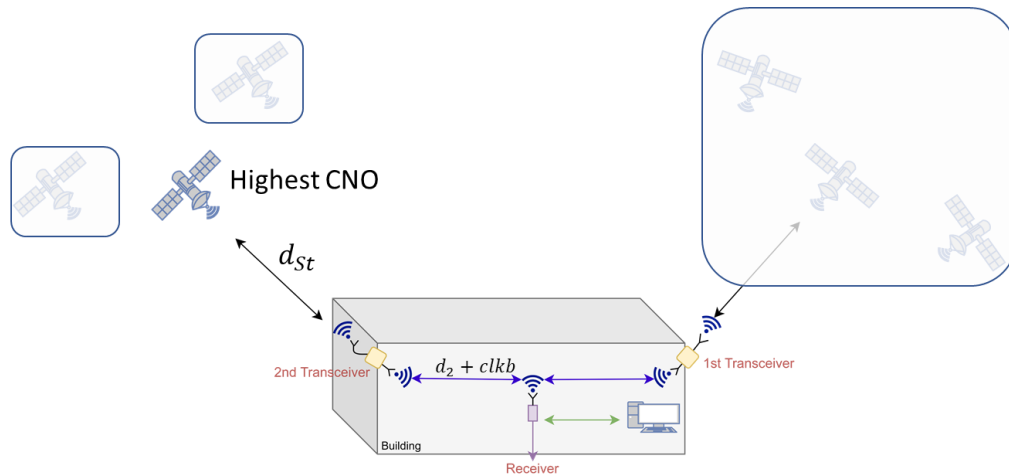


Figure 5.15 2<sup>nd</sup> repeater position and pseudorange

Similar to 1<sup>st</sup> repeater, 2<sup>nd</sup> repeater also selects the satellites that are within the antenna view boundaries defined. Then, the satellite with the highest CNO from 2<sup>nd</sup> repeater is opted out. Next, the pseudorange PR2 is recorded as given in Eq. 5.3.

$$PR2 = d_{st} + d_2 + clk_b \quad (5.3)$$

where  $clkb$  denotes the clock biases,  $d_1$  denotes the distance between 2<sup>nd</sup> repeater and indoor receiver, and  $d_{st}$  denotes the distance between the 2<sup>nd</sup> repeater and the chosen satellite.  $d_{st}$  is calculated using the distance formula as both satellite and repeater positions are known.

Step 6: Calculated  $d_{st}$  is subtracted from measured pseudorange PR2. The resulting term PR2' is the summation of indoor distance  $d_2$  and clock bias term due to receiver as given in Eq. 5.4.

$$PR2' = PR2 - d_{st} = d_2 + clkb \quad (5.4)$$

Note that  $clkb$  terms in Eq. 5.2 and Eq. 5.4 are the same terms.

Subtracting Eq. 5.2 from Eq. 5.4,  $clkb$  terms cancel each other out. The resulting term is the difference between  $d_1$  and  $d_2$  as provided in Eq. 5.5.

$$PR2' - PR1' = d_2 - d_1 \quad (5.5)$$

The summation of  $d_1$  and  $d_2$  corresponds to the indoor distance between two repeaters as provided in Eq. 5.6.

$$d_{r1r2} = d_2 + d_1 \quad (5.6)$$

where  $d_{r1r2}$  represents the indoor distance between two repeaters. The distance between repeaters ( $d_{r1r2}$ ) is known as the repeater locations are known.

One can conclude that Eq. 5.5 and Eq. 5.6 forms a system of equations of 2 unknowns and can be solved. The system of equations is depicted in Figure 5.16. Solving both equations results in  $d_1$  and  $d_2$ , which are the distance between repeater 1 and receiver, and the distance between repeater 2 and receiver. Thus, 1D positioning can be completed.

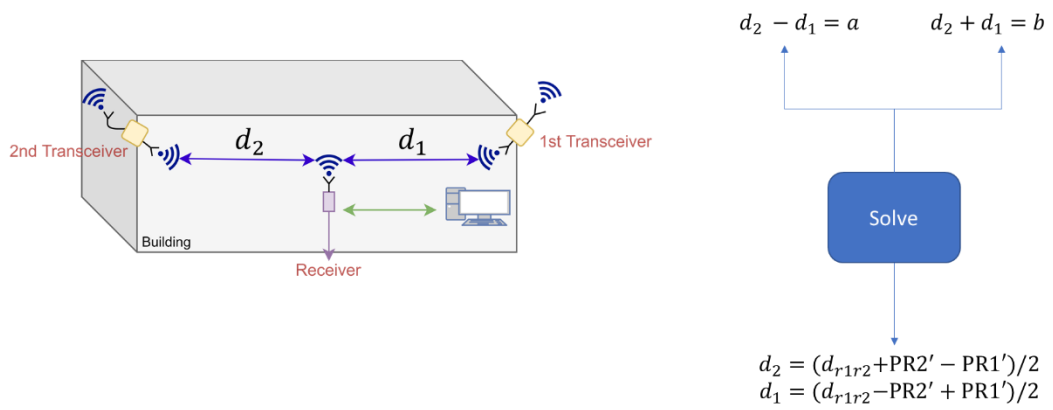


Figure 5.16 Solution to the system of two equations for 1D positioning

Note that repeaters are shown as transceivers in Figure 5.12-16 in this section.

### 5.3.2 1D Positioning Test Setup

The 65-meter long corridor in the Faculty of Engineering and Natural Sciences building in Sabanci University is selected for the measurements. The 2 repeaters are located on the opposite sides of the corridor while the receiver is kept on the line that passes through the deployed repeaters. The test scenario is visualized in Figure 5.17.

The receiver is located 29 meters away from repeater 1 and 36 meters away from repeater 2. They are all located on the same line along the 65m-long corridor. The longitude and latitude of repeater 1 and repeater 2 are detected as (29.378730, 40.890794) and (29.379485, 40.890944), respectively.

The directional outdoor GPS antenna of the repeater 1 is located on  $270^0$  in azimuth with the elevation of  $45^0$  from the horizontal plane while the directional outdoor GPS antenna of the repeater 2 is located on  $40^0$  in theta with the elevation of  $45^0$  from the horizontal plane. The beamwidth of the directional outdoor GPS antenna is taken as  $100^0$  in azimuth

and  $50^\circ$  in elevation. The regions that are visible to the outdoor GPS antennas are shown in Figure 5.18 with the satellite constellation during the measurement time.

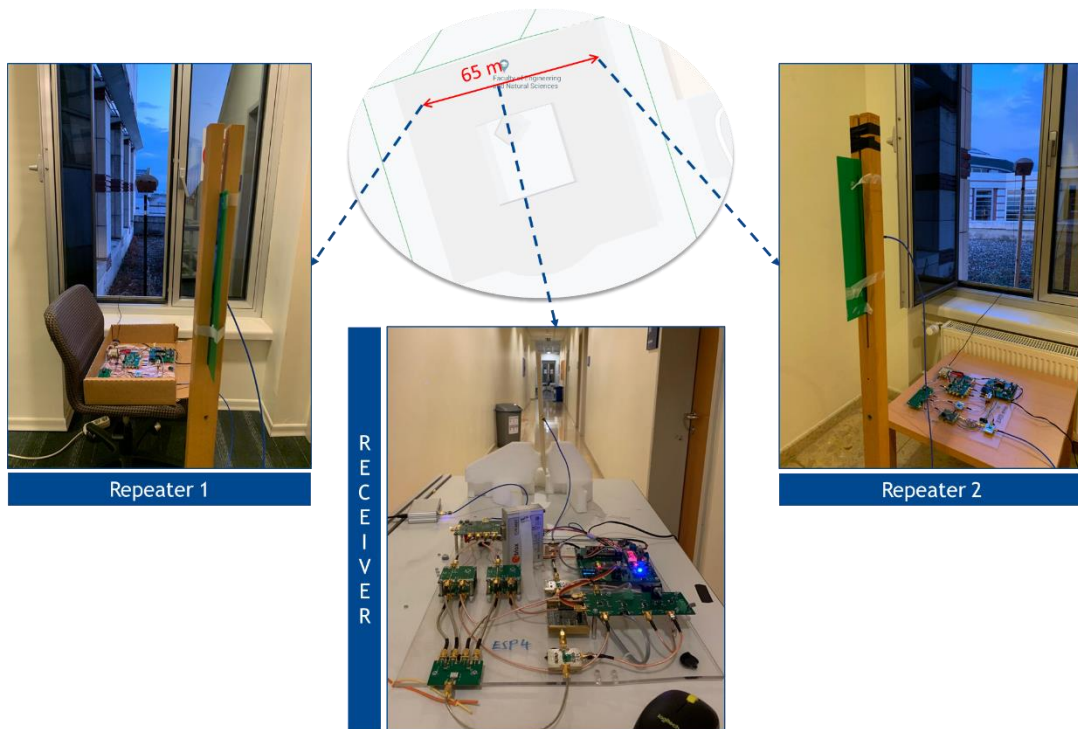


Figure 5.17 Test setup for 1D Positioning

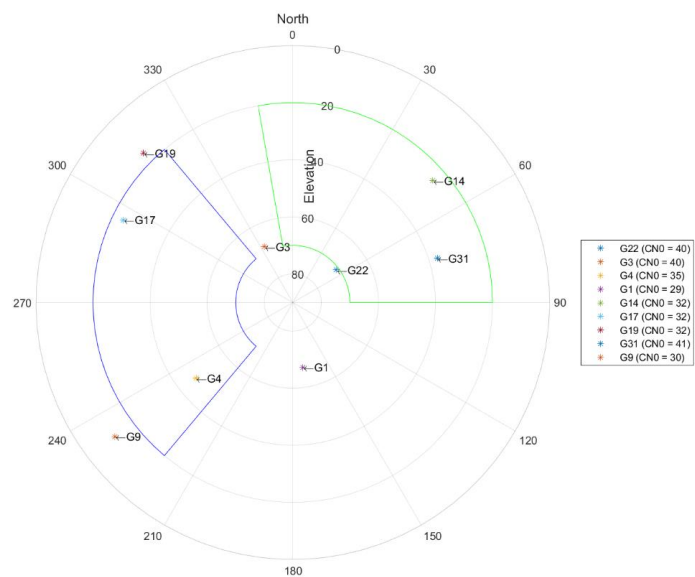


Figure 5.18 The region surrounded by the blue curve corresponds to the visible region by repeater 1 while the green curve surrounds the region visible to repeater 2

According to the satellite constellation and satellites that can be picked up by the repeaters, it is seen that G4, G17, G14, and G31 are seen by the repeater for each sample collected. Therefore, analysis in the rest of this study is conducted with these satellites.

The 1D positioning tests are conducted with the repeater and receiver hardware explained in Chapters 3 and 4. The indoor 433 MHz antennas are dipole antennas provided in Appendix C for a less complex deployment. One can also use the indoor 433 MHz antennas provided in Chapters 3 and 4 to increase the directivity of the repeaters. 1D position estimations are conducted with the different satellite combinations provided in Table 5.3.

Table 5.3 1D Positioning Tests and Selected Satellites

	<i>Repeater 1</i>	<i>Repeater 2</i>
<b>Test 1</b>	Satellite G4	Satellite G14
<b>Test 2</b>	Satellite G17	Satellite G31
<b>Test 3</b>	Satellite G4	Satellite G31

### 5.3.3 1D Positioning Test Results

The collected results are processed with MATLAB® algorithm proposed for 1D positioning. The results are correct for samples where the CNO ratio is maximum. The distances from repeater 1 to receiver are plotted in the following sub-sections.

In this test, the attenuator's attenuation level in each repeater and receiver is set to 0 dB. There are 2 satellites seen by each repeater separately as shown in Figure 5.19. In this

test, 3 combinations of satellites are used for 1D indoor positioning keeping attenuations at 0 dB. These combinations are as follows:

1. The first satellite combination is the pair of G4 down-converted and retransmitted by repeater 1 and G14 down-converted and retransmitted by repeater 2
2. The second satellite combination is the pair of G17 down-converted and retransmitted by repeater 1 and G31 down-converted and retransmitted by repeater 2
3. The third satellite combination is the pair of G4 down-converted and retransmitted by repeater 1 and G31 down-converted and retransmitted by repeater 2

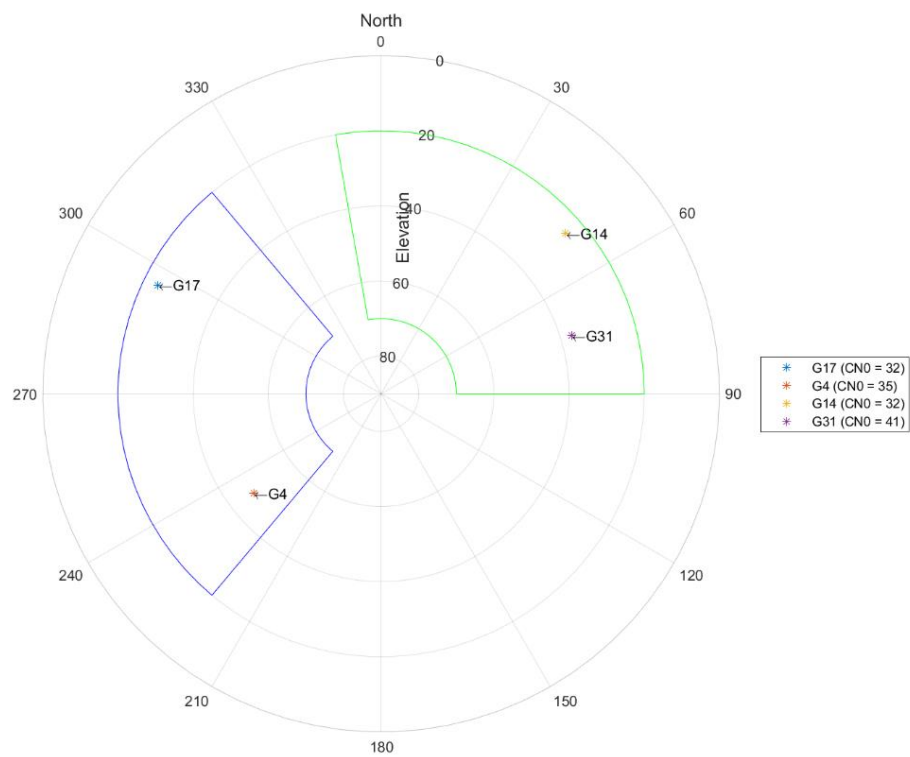


Figure 5.19 Satellite constellation within the directional antenna's angle of view

To show how intermediate values calculated in the algorithm behaves for G4 and G14, Figure 5.20 and Figure 5.21 are provided, respectively, for repeater 1 and repeater 2.

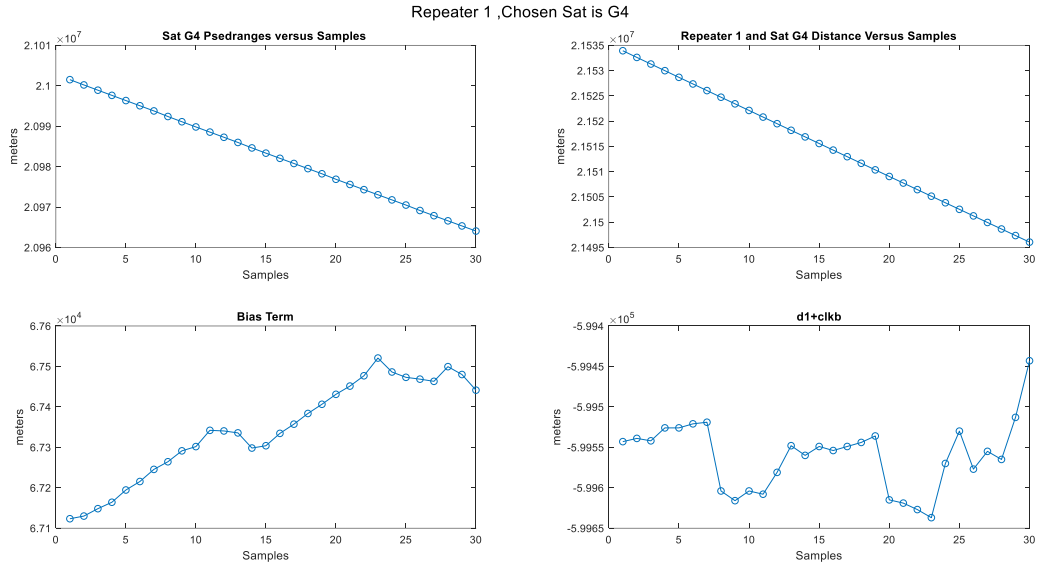


Figure 5.20 PR1, clkb, dst, and d1+clkb terms when G4 is selected from repeater 1

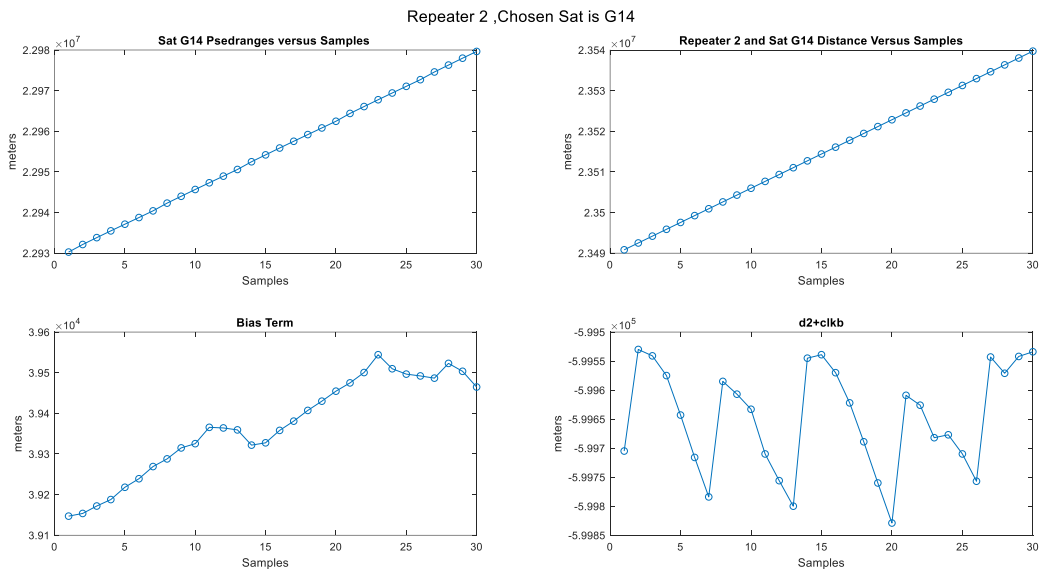


Figure 5.21 PR2, clkb, dst, and d2+clkb terms when G14 is selected from repeater 2

Using intermediate values and the algorithm proposed, the results for each sample is calculated. Each sample is collected when the receiver is stationary and 29 m away from repeater 1 and 36 m away from repeater 2.

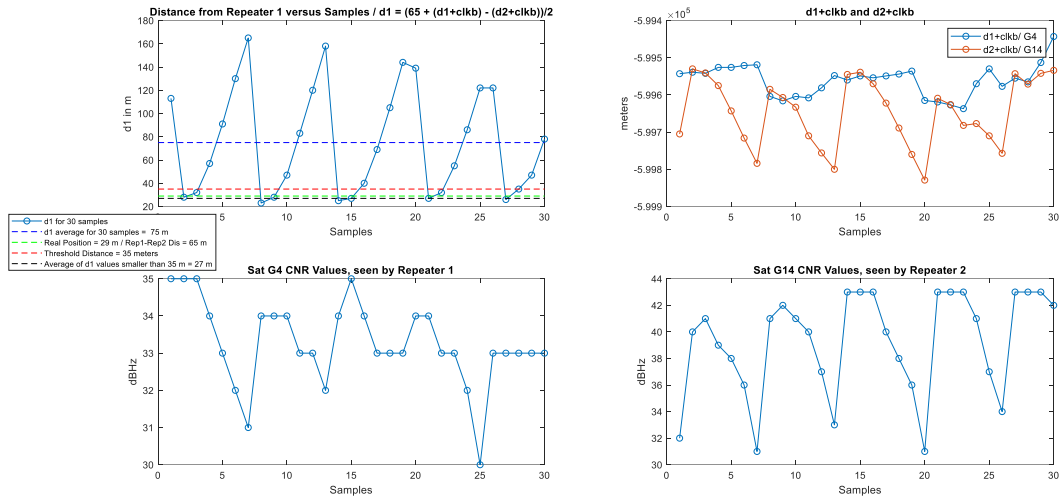


Figure 5.22  $d1$  distance,  $d1+clkb$  and  $d2+clkb$  and CNO ratios for G4 and G14

Figure 5.22 shows that the CNO ratio of the G14 signal retransmitted from repeater 2 varies between 43 dB and 31 dB while the variation is much less for the G4 signal retransmitted from repeater 1. Due to high variation, the  $d2+clkb$  term varies and the solution for  $d1$  and  $d2$  diverts from the real values.

It is shown that for the values where  $d1+clkb$  and  $d2+clkb$  are the closest, the solution to  $d1$  yields to 29 meters. 10 samples out of 30 samples yield a  $d1$  result that is less than 35 meters. The average of these 10 minimum samples yields a distance of 28.3 meters. It is also seen that  $d1+clkb$  and  $d2+clkb$  terms are closest when the CNO ratios are maximized.

Calculated distances with  $\pm 6$  meters accuracy to the actual distance value between repeaters and receiver are provided in Table 5.4. The listed samples in Table 5.4 have resulted in  $\pm 6$  meters to the actual values. These samples correspond to the cases where the carrier to noise ratio of the retransmitted signals from the selected satellites G4 and G14 are higher compared to the rest in the test 1.

Table 5.4 Calculated distances from receiver to repeaters 1 and 2 in test 1

<b>Sample Number</b>	<b>Calculated Distance to Repeater 1 (d1)</b>	<b>Actual Distance to Repeater 1 (d1)</b>	<b>Calculated Distance to Repeater 2 (d2)</b>	<b>Actual Distance to Repeater 2 (d2)</b>
2	28 m	29 m	37 m	36 m
3	32 m	29 m	33 m	36 m
8	23 m	29 m	43 m	36 m
9	28 m	29 m	37 m	36 m
14	25 m	29 m	40 m	36 m
15	27 m	29 m	38 m	36 m
21	27 m	29 m	38 m	36 m
22	32 m	29 m	33 m	36 m
27	26 m	29 m	39 m	36 m
28	35 m	29 m	30 m	36 m

In the test 2, satellites G17 and G13 are selected. When the selected satellites are G17 and G31, the intermediate values calculated in the algorithm are shown in Figure 5.23 and Figure 5.24, respectively, for repeater 1 and repeater 2.

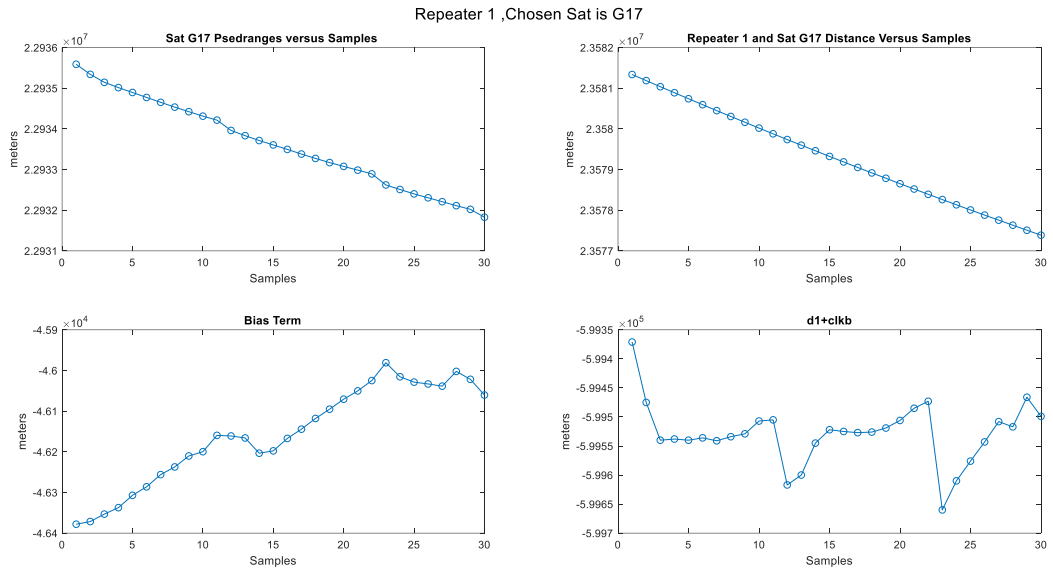


Figure 5.23 PR1, clk, dst, and d1+clk terms when G17 is selected from repeater 1

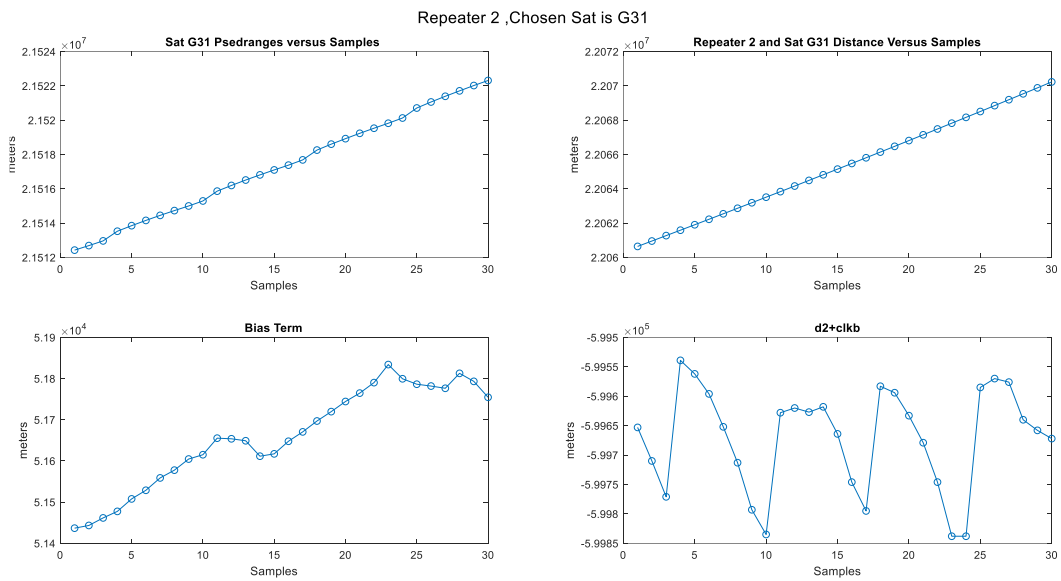


Figure 5.24 PR2, clk, dst, and d2+clk terms when G31 is selected from repeater 2

Using intermediate values and the algorithm proposed, the results for each sample is calculated. Each sample is collected when the receiver is stationary and 29 m away from repeater 1 and 36 m away from repeater 2.

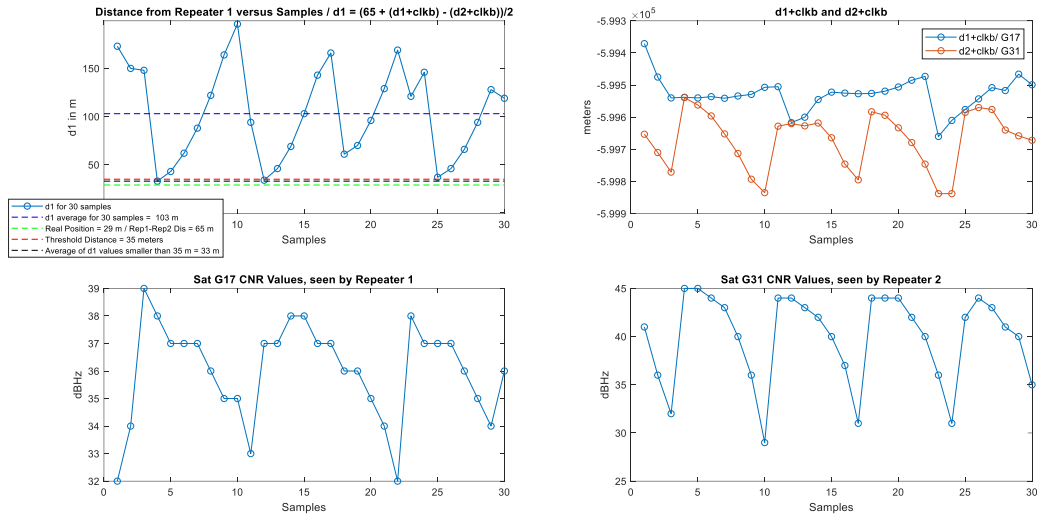


Figure 5.25  $d1$  distance,  $d1+clkb$  and  $d2+clkb$  and CNO ratios for G17 and G31

Figure 5.25 shows that the CNO ratio of the G31 signal retransmitted from repeater 2 varies between 45 dB and 29 dB while the variation is much less for the G17 signal retransmitted from repeater 1. Due to high variation, the  $d2+clkb$  term varies on a much larger scale than  $d1+clkb$  does. Therefore, the solution for  $d1$  and  $d2$  diverts from the exact values when such variation occurs.

It is shown that for the values where  $d1+clkb$  and  $d2+clkb$  are the closest, the solution to  $d1$  yields to 29 meters. The average of the samples producing a  $d1$  solution that is less than 35 meters away is 33 meters. It is also seen that  $d1+clkb$  and  $d2+clkb$  terms are closest when the CNO ratios are maximized.

Calculated distances with  $\pm 6$  meters accuracy to the actual distance value between repeaters and receiver are provided in Table 5.5. The listed samples in Table 5.5 have resulted in  $\pm 6$  meters to the actual values. These samples correspond to the cases where the carrier to noise ratio of the retransmitted signals from the selected satellites G17 and G31 are higher compared to the rest in the test 2.

Table 5.5 Calculated distances from receiver to repeaters 1 and 2 in test 2

Sample Number	Calculated Distance to Repeater 1 (d1)	Actual Distance to Repeater 1 (d1)	Calculated Distance to Repeater 2 (d2)	Actual Distance to Repeater 2 (d2)
4	33 m	29 m	32 m	36 m
12	34 m	29 m	31 m	36 m

In the test 3, satellites G4 and G31 are selected. When the selected satellites are G4 and G31, respectively, from repeater 1 and 2, the results for d1, d1+clkb and d2+clkb, and CNO ratios are depicted in Figure 5.26.

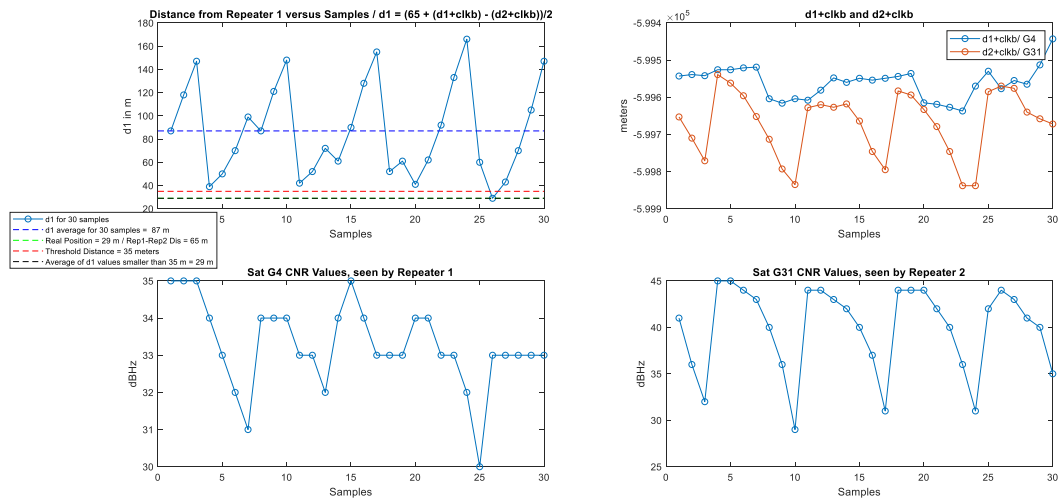


Figure 5.26 d1 distance, d1+clkb and d2+clkb and CNO ratios for G4 and G31

The CNO ratio of G31 retransmitted from repeater 2 varies between 45 dB and 29 dB while the variation is much less for the G4 signal from repeater 1. Due to high variation, the d2+clkb term varies on a much larger scale than d1+clkb does. Therefore, the solution for d1 and d2 diverts from the exact values when such variation occurs as explained previously.

It is shown that for the values where d1+clkb and d2+clkb are the closest, the solution to d1 yields to 29 meters. The average of the samples producing a d1 solution that is less

than 35 meters away from the repeater is 29 meters. It is also seen that  $d1+clk_b$  and  $d2+clk_b$  terms are closest when the CNO ratios are maximized.

Calculated distances with  $\pm 6$  meters accuracy to the actual distance value between repeaters and receiver are provided in Table 5.6. The listed samples in Table 5.6 have resulted in  $\pm 6$  meters to the actual values. These samples correspond to the cases where the carrier to noise ratio of the retransmitted signals from the selected satellites G4 and G31 are higher compared to the rest in the test 3.

Table 5.6 Calculated distances from receiver to repeaters 1 and 2 in test 3

<b>Sample Number</b>	<b>Calculated Distance to Repeater 1 (d1)</b>	<b>Actual Distance to Repeater 1 (d1)</b>	<b>Calculated Distance to Repeater 2 (d2)</b>	<b>Actual Distance to Repeater 2 (d2)</b>
26	29 m	29 m	36 m	36 m

## CHAPTER 6 CONCLUSION AND FUTURE WORK

A new system and method for indoor positioning using GPS signals are proposed and investigated in this work. The following conclusions are made based on the proposed method and system:

GPS signals may be retransmitted by repeaters after down-converting 1575.42 MHz GPS signals to 433 MHz ISM band to avoid restrictions on the use of GNSS signals and conventional repeaters. The down-conversion may help increasing coverage area due to higher allowable maximum output power in 433 MHz ISM band, less free space path loss, and higher penetration through walls with higher wavelength.

The down-conversion may be followed by an up-conversion as RF frontend of an off-the-shelf GNSS receiver. In such a case, the GPS signal integrity is preserved. By integrating the proposed receiver with an off-the-shelf GPS receiver, one may extract the raw data and navigation information out of the GPS message, process it in the proposed algorithm, and obtain the position.

The proposed receiver front end has a maximum overall gain of 41.3 dB excluding the 433 MHz receive antenna. The proposed repeaters have a maximum overall gain of 34.1 dB excluding the directional outdoor GPS antenna and 433 MHz indoor transmit antenna.

Both repeater and receiver front end circuit gains can be reduced by 31.5 dB with the attenuators deployed in both boards. Therefore, the gain of the repeater and receiver front end can be varied.

The designed and implemented directional outdoor GPS antenna have a gain of 34.45 dBi. The outdoor antenna is made more directive by constructing a reflective conic structure around an off-the-shelf GPS antenna. The conic structure implemented in this thesis has resulted in an increase in the gain of the outdoor GPS antenna by 4.45 dB according to the measurement results. The antenna directivity facilitates GPS satellite selection that can be used in the positioning algorithms.

The designed indoor 433 MHz antennas attain gain values between 1.53 dBi to 6.27 dBi. Moreover, a simpler dipole antenna is provided in the Appendix C that has a gain of 2.01 dBi according to the simulation results.

1D positioning tests provided in this thesis prove that satellite selection and carrier to noise ratio stability of the retransmitted signals are the key factors to determine the distances between receiver and repeaters. It is shown in test 1 that for the samples that the carrier to noise ratio is high relative to the rest of the samples, one can achieve results varying by  $\pm 6$  meters to the actual distance. If the variations in the carrier to noise ratio could be minimized, the indoor distance to the repeaters can be determined more closely.

In this study, it is explained that 1D positioning is possible using 2 repeaters. One may estimate the indoor position with relative distances to each repeater. Using cancellation of clock biases of the receiver and solving a system of two equations, distances between the repeaters and receiver are figured out in this study. Using a very similar idea with 3 repeaters, one may also achieve 2D indoor positioning.

The results obtained during the course of this thesis work indicate that the carrier to noise ratio of the down-converted and retransmitted signals must be stable for accuracy.

The idea of using the down-conversion and up-conversion scheme proposed in this study works for 1D indoor positioning. Moreover, 1D indoor positioning proposed in this thesis

work is a basis for 2D indoor positioning. To this end, indoor positioning using 3 repeaters can be carried on for 2D indoor positioning in the future. In order to remove the clock bias of the receiver in 2D positioning, the algorithm will be implemented using the LSNAV algorithm. The triangulation of 3 distances to 3 repeaters will be used for 2D indoor positioning.

## **APPENDIX A**

### **DESIGNING VOLTAGE REGULATOR BLOCK IN REPEATER HARDWARE USING THERMAL DESIGN BASICS**

The linear voltage regulating circuit elements that can operate under 9 V input voltage and generate 3.3V, 5V and 6V voltages are used in the design of this board. The main reason why switched circuit elements are not preferred is that the noise that switching regulators cause is higher than linear voltage regulators. Since the noise in this block may affect the overall RF performance, linear voltage regulators have been preferred although heating problems may arise due to these regulators. To overcome heating problems, the linear voltage regulators have been deployed and selected by considering the power dissipation expected from those elements, thermal resistances of each component, and other thermal design parameters. For this reason, basic thermal design principles have been taken into consideration in the selection of circuit elements and their successive placement.

Semiconductor circuit elements have a specific junction temperature under which they continue to operate normally. Thermal resistance defines the resistance that heat encounters while transferring from a heated integrated circuit element to the environment surrounding it. The thermal resistance is denoted with  $\Theta_{JA}$ . Its unit is  $^{\circ}\text{C}/\text{watt}$  ( $^{\circ}\text{C}/\text{W}$ ) [92]. The thermal resistance determines how much the difference is with the ambient temperature if 1 Watt of power (P) is dissipated. Therefore, the temperature change ( $\Delta T$ ) in Celcius degree ( $^{\circ}\text{C}$ ) is expressed as in Eq. A.0.1.

$$\Delta T = P \times \theta \quad (\text{A.0.1})$$

Additional thermal design equations and terms are presented in Figure A.1.

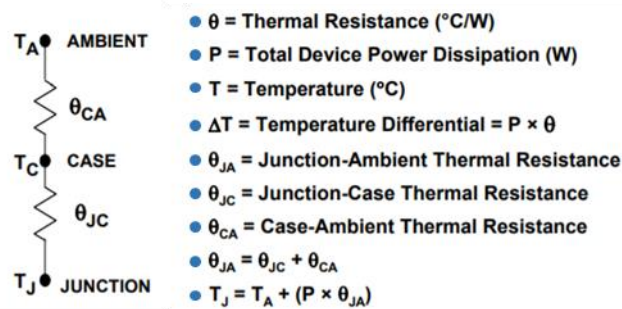


Figure A.1 Thermal design terms and equations [92]

Since the output voltage of the L7806 chip is 6V, it is possible to obtain the necessary input voltage for the ADRF6820-EVALZ from this chip. The output voltage of the UA78M05CDCYRG3 chip is 5V, therefore, it is possible to obtain the input voltages of the low noise amplifiers from this component. The output voltage of the UA78M33CDCYRG3 chip is 3.3 V, so it is possible to obtain the input voltages required for the bias tee and the attenuator from this component. The maximum temperature ( $T_{\text{max}}$ ) value that each chip can operate up to is  $125^{\circ}\text{C}$  and the ambient temperature is used as  $25^{\circ}\text{C}$  in the analysis.

The current value ( $I_{\text{out}}$ ) to be drawn from the L7806 chip by ADRF6820-EVALZ is 0.412 A. A total current of 0.286 A ( $I_{\text{out}}$ ) is drawn from UA78M05CDCYRG3 by 2 low noise amplifiers. 0.2 and 0.015 A current is drawn from UA78M33CDCYRG3 by attenuator

and bias tee, respectively. Two separate UA78M33CDCYRG3 chips are used in the voltage regulator block to provide 3.3 V to bias tee and attenuator.

Under the given circumstances,  $T_j$  values are calculated for each linear voltage regulator chip and it is found to be below  $T_{max}$  of  $125^{\circ}\text{C}$  for each chip. Therefore, the linear voltage regulator chips can operate safely in this design without encountering an overheating problem. The thermal design analysis of the linear voltage regulators used in the voltage regulator block is presented in Table A.1.

**Table A.6.1 Thermal analysis of the linear voltage regulators used for repeater**

Selected Regulator	Max. Current	Output Voltage	$T_{max}$ ( $^{\circ}\text{C}$ )	$I_{out}$ (A)	$V_{drop}$ (V)	$P_{out}$ (W)	$\Theta_{ca}$	$\Theta_{jc}$	$\Theta_{ja}$	$T_a$	$T_j$
STI L7806	1.5 A	6 V	125	0.412	3	1.236	45	5	50	25	86.8
TI UA78M05CDYRG3	0.5 A	5 V	125	0.286	4	1.144	2	17	19	26	47.73
TI UA78M33CDYR	0.5 A	3.3 V	125	0.2	5.7	1.2	2	17	19	25	46.66
TI UA78M33CDYR	0.5 A	3.3 V	125	0.015	5.7	0.09	2	17	19	25	26.62

The voltage regulator block design is realized by considering the thermal design principles as described above and the chips are chosen accordingly. The selected chips are assembled as in the circuit schematic in Figure A.2.

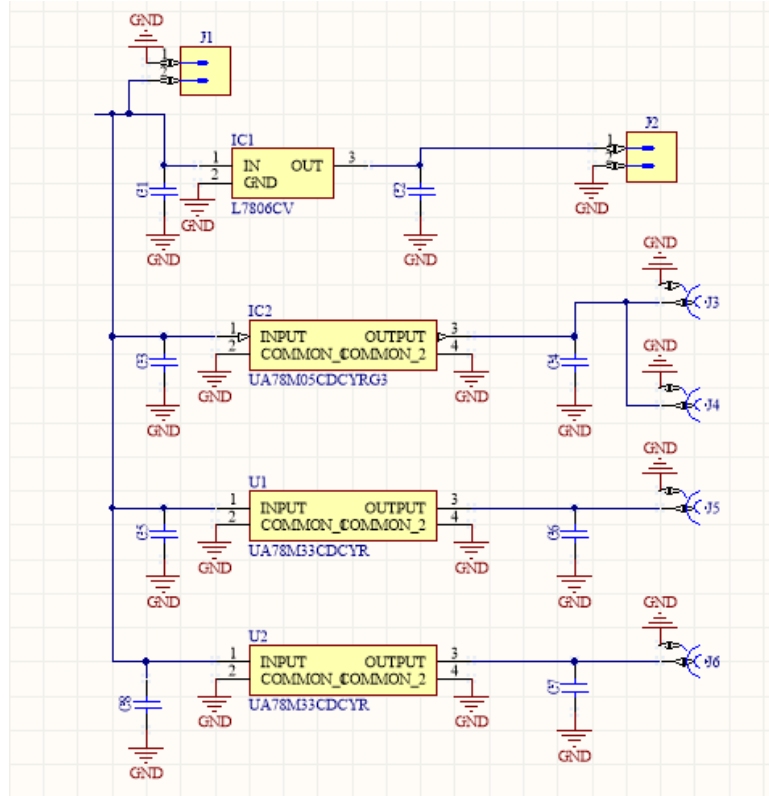


Figure A.2 The schematic of the repeater's voltage regulator block

The layout of the voltage regulator block is presented in Figure A.3. The board is fabricated according to the layout given.

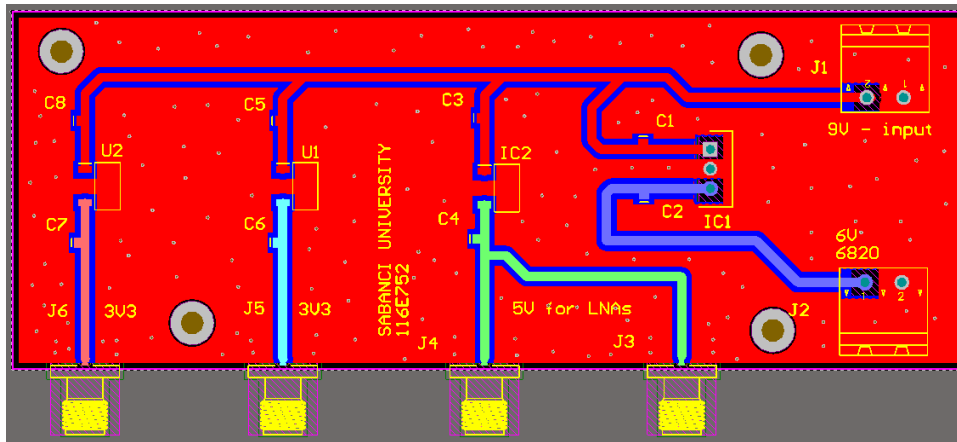


Figure A.3 The layout of the repeater's voltage regulator block

The output voltages are measured given that the input voltage is 9V for the board. The output voltages and drawn current values are adequate to supply modules in repeater hardware.

## **APPENDIX B**

### **DESIGNING VOLTAGE REGULATOR BLOCK IN RECEIVER HARDWARE USING THERMAL DESIGN BASICS**

Linear voltage regulators that operate under 9 V input voltage and generate 2.68V, 3.3V, and 5V voltages are used in the design of this board. Unlike the voltage regulator designed for the repeater circuit, this board has a 2.68V output. The board is designed by considering the heating problems of the linear voltage regulators as for the voltage regulator board in the repeater. For this reason, basic thermal design principles have been taken into consideration in the selection of circuit elements and their successive placement. Thermal design analysis of the voltage regulator block, designed to be 9V input voltage, output voltages 3.3V for ADRF6720-27-EVALZ board, 5V for low-noise amplifiers, 3.3V for power attenuator, 2.68V for T-supply circuit board, are presented in Table B.1.

Table B.6.2 Thermal analysis of the linear voltage regulators used for receiver

Selected Regulator	Max. Current	Output Voltage	Tmax (°C)	Iout(A)	Vdrop (V)	Pout (W)	$\Theta_{ca}$	$\Theta_{jc}$	$\Theta_{ja}$	T <sub>a</sub>	T <sub>j</sub>
STI L7806	1.5 A	6 V	125	0.369	3	1.236	45	5	50	25	84.4
STI LD1117AS33TR	1.0 A	3.3 V	125	0.369	2.7	0.99	45	5	50	25	78.46
TI UA78M05CDCYRG3	0.5 A	5 V	125	0.286	4	1.144	2	17	19	26	47.73
TI UA78M33CDYR	0.5 A	3.3 V	125	0.2	5.7	1.2	2	17	19	25	46.66
AMS1117ADJ	0.5 A	2.68 V	125	0.17(max)	6.5	1.105			90	25	124.45(max)

Since the output voltage of the L7806 chip is 6V, it is possible to obtain the necessary input voltage for the ADRF6720-27 EVALZ from the 3.3V output LD1117AS33TR chip, which is added in series to L7806 chip. Thus, while decreasing from 9 volts to 3.3 volts, the voltage decreases step by step and the overheating problem is prevented as shown in the analysis. Since the output voltage of the UA78M05CDCYRG3 chip is 5V, it is possible to obtain the input voltages of the low noise amplifiers from this chip. Since the output voltage of the UA78M33CDCYRG3 chip is 3.3 V, it is possible to obtain the input voltage required for the power attenuator to be used later from this chip. The required voltage at the RF inputs of the ADRF6720-27-EVALZ board can be obtained by adjusting the AMS 1117ADJ chip output with resistors.

The highest temperature (Tmax) value that each chip can operate is 125°C and ambient temperature is used as 25°C in calculations. The current value (Iout) to be drawn from the L7806 and LD1117AS33TR chips by ADRF6720-27 EVALZ is 0.396 A. 0.286 A current (Iout) is drawn from 2 low noise amplifiers from UA78M05CDCYRG3 chip. The power attenuator draws 0.2 A from the UA78M33CDCYRG3 chip. In this case, Tj values remain below 125 ° C for each chip as shown in Table B.1. Therefore, the chips can operate safely in this design without encountering an overheating problem.

The amount of current to be drawn from the AMS 1117ADJ chip has not been measured before, and the maximum current value that can be drawn is calculated for Tmax = 125°C and is found to be 0.17 A. It has been seen in the measurements that this chip does not

heat up and continues to work. The current value drawn for ADRF6720-27-EVALZ at RF inputs is much less than 0.17 A.

The voltage regulator block design is realized by considering the thermal design principles as described above and the chips are chosen accordingly. The selected chips are assembled as in the circuit schematic in Figure B.1.

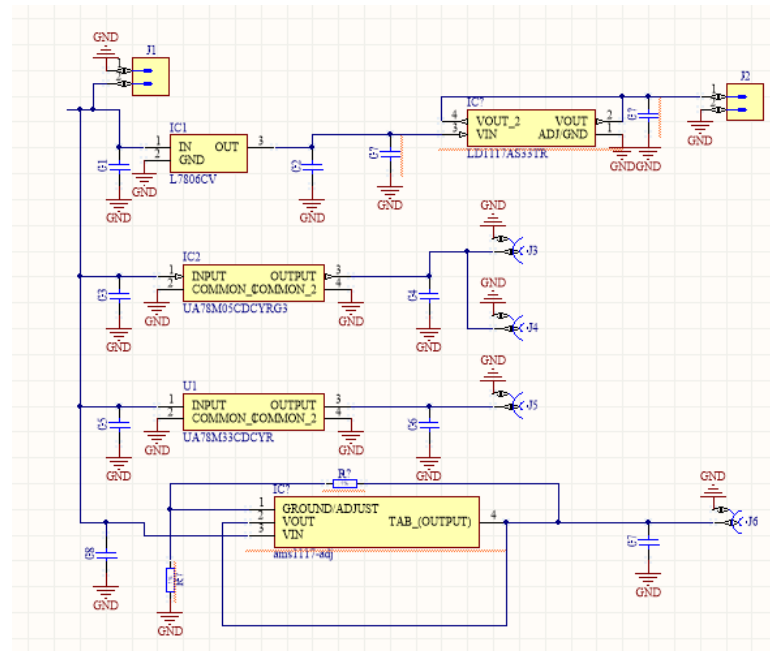


Figure B.1 The schematic of the receiver's voltage regulator block

The layout of the voltage regulator block is presented in Figure B.2. The board is fabricated according to the layout given.

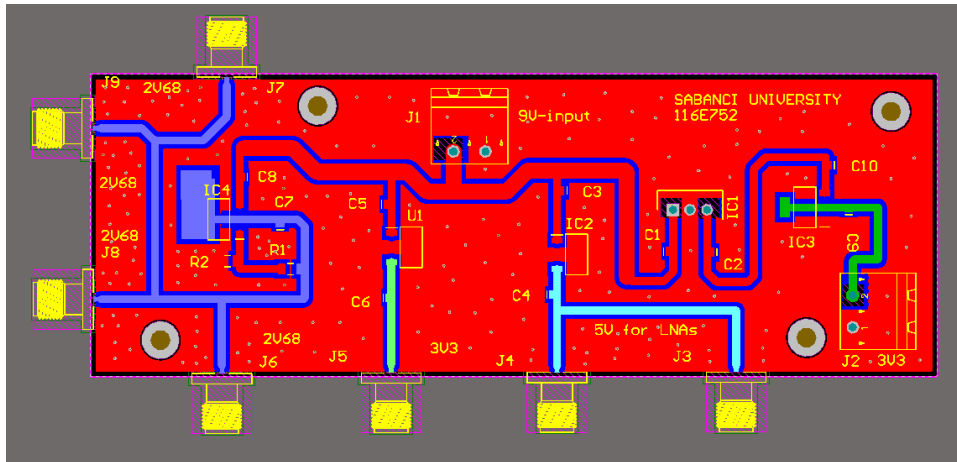


Figure B.2 The layout of the receiver's voltage regulator block

The output voltages are measured given that the input voltage is 9V for the board. The output voltages and drawn current values are adequate to supply modules in receiver hardware.

## APPENDIX C

### DESIGN OF 433 MHZ DIPOLE ANTENNA

433 MHz dipole antennas are designed and fabricated due to their simplicity in design and ease of use during the indoor positioning tests. The antennas are designed on a 1.6 mm thick FR4 substrate with relative permittivity of 4.6. The copper thickness is 35  $\mu\text{m}$  on both sides of the substrate.

The designed antenna and feed structure with the dimensions are shown in Figure C.1.

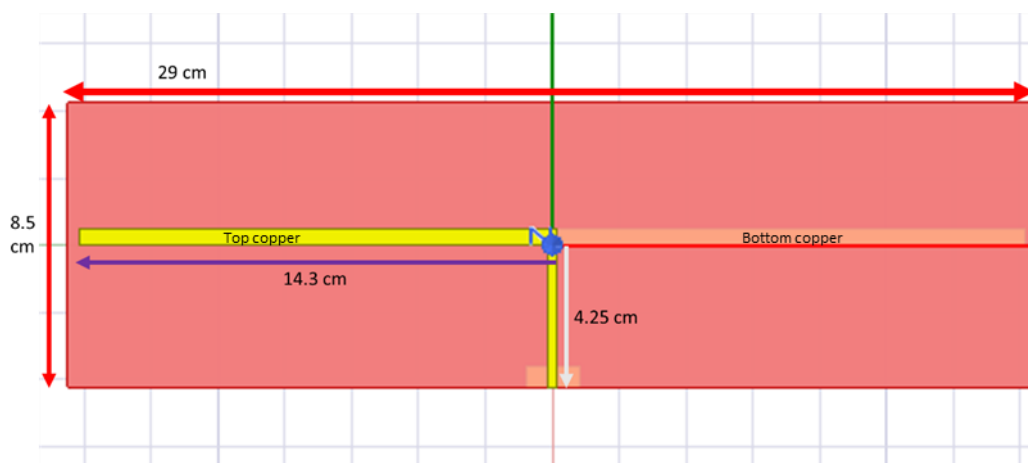


Figure C.1 433 MHz Dipole Antenna Dimensions

The S11 result of the simulation is provided in Figure C.2.

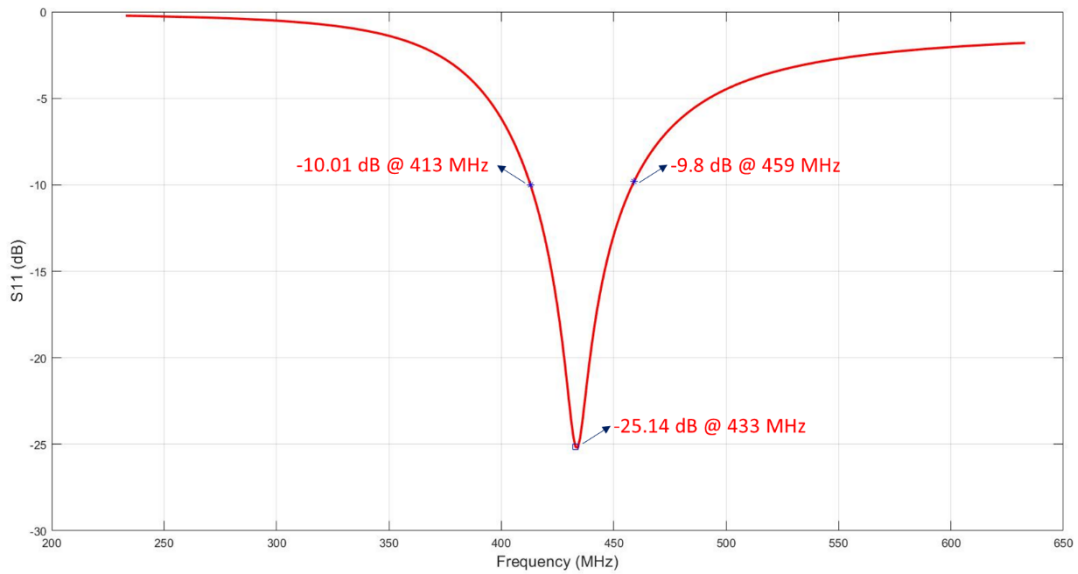


Figure C.2 Simulation Result for S11

According to the S11 simulation result, the 10 dB bandwidth of the designed antenna is 46 MHz. The minimum S11 is -25 dB and obtained at 433 MHz.

The realized maximum gain of the antenna is 2.1 dBi. The antenna radiates in both sides of the printed surfaces. The beamwidth of the antenna is 80° on both sides. Radiation patterns for maximum realized gain are provided in Figure C.3.

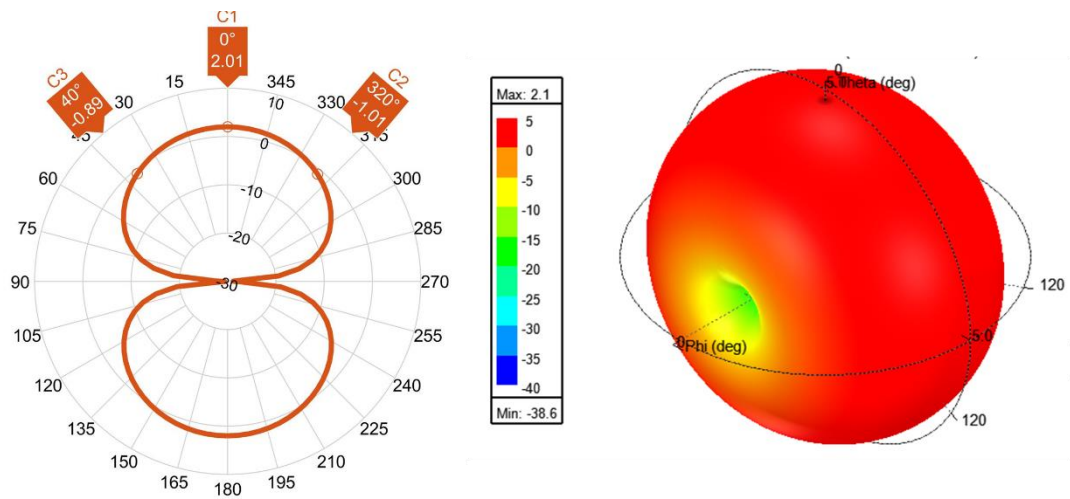


Figure C.3 2D and 3D simulated realized gain and radiation plots

## REFERENCES

- [1] U.S. Coast Guard Navigation Center, "NAVSTAR GPS Space Segment/Navigation User Segment Interfaces," 2019.
- [2] R. Mautz, "Overview Of Current Indoor Positioning Systems," *Geod. Cartogr.*, vol. 35, no. 1, pp. 18–22, 2009, doi: 10.3846/1392-1541.2009.35.18-22.
- [3] I. Tekin, B. Ayhan, and K. Ozsoy, "Indoor Positioning System Based On Gps Signals And Pseudolites With Outdoor Directional Antennas," US 2012286992 A1, 2012.
- [4] K. Ozsoy, A. Bozkurt, and I. Tekin, "Indoor Positioning Based On Global Positioning System Signals," *Microw. Opt. Technol. Lett.*, vol. 55, no. 5, pp. 1091–1097, 2013.
- [5] Markets and Markets, "Indoor Location Market - GLOBAL FORECAST TO 2022," 2017.
- [6] KBV Research, "Global Indoor Location Market," 2017.
- [7] F. Zafari, A. Gkelias, and K. K. Leung, "A Survey Of Indoor Localization Systems And Technologies," *EEE Commun. Surv. Tutorials*, vol. 21, no. 3, pp. 2568–2599, 2019, doi: 10.1109/COMST.2019.2911558.
- [8] G. M. Mendoza-Silva, J. Torres-Sospedra, and J. Huerta, "A Meta-Review Of Indoor Positioning Systems," *Sensors (Switzerland)*, vol. 19, no. 20, 2019, doi: 10.3390/s19204507.
- [9] P. Kumar, L. Reddy, and S. Varma, "Distance Measurement And Error Estimation Scheme For RSSI Based Localization In Wireless Sensor Networks," pp. 4–7, 2009.
- [10] Z. Yang, Z. Zhou, and Y. Liu, "From RSSI To CSI : Indoor Localization Via Channel Response," vol. 46, p. 32, 2013, doi: 10.1145/2543581.2543592.
- [11] R. Faragher and R. Harle, "Location Fingerprinting With Bluetooth Low Energy Beacons," vol. 33, no. 11, pp. 2418–2428, 2015.
- [12] H. Liu, H. Darabi, P. Banerjee, and J. Liu, "Survey Of Wireless Indoor Positioning Techniques And Systems," *IEEE Trans. Syst. MAN, Cybern. C Appl. Rev.*, vol. 37, no. 6, pp. 1067–1080, 2007.
- [13] H. Chen, T. Lin, H. T. Kung, C. Lin, and Y. Gwon, "Determining RF Angle Of Arrival

- Using COTS Antenna Arrays : A Field Evaluation,” in *Proc. of the MILCOM Conf., 2012.*, 2012.
- [14] S. Kumar, S. Gil, D. Katabi, and D. Rus, “Accurate Indoor Localization With Zero Start-Up Cost,” in *Proceedings of the 20th annual international conference on Mobile computing and networking*, pp. 483–494.
- [15] D. Waltenegus and C. Poellabaurer, *Fundamentals of Wireless Sensor Networks Theory and Practice*. John Wiley & Sons, 2010.
- [16] M. Scherhauf, M. Picheler, D. Müller, A. Ziroff, and A. Stelzer, “Phase-Of-Arrival-Based Localization Of Passive UHF RFID Tags,” *2013 IEEE MTT-S Int. Microw. Symp. Dig.*, 2013.
- [17] D. Vasisht *et al.*, “Decimeter-Level Localization With A Single Wifi Access Point,” in *the Proceedings of the Decimeter-Level Localization with a Single WiFi Access Point*, 2016.
- [18] M. Cypriani, F. Lassabe, P. Canalda, and F. Spies, “Open Wireless Positioning System : A Wi-Fi-Based Indoor Positioning System,” in *Vehicular Technology Conference Fall (VTC 2009-Fall)*, 2009, pp. 1– 5.
- [19] H. Zou, H. Jiang, X. Lu, and L. Xie, “An Online Sequential Extreme Learning Machine Approach To Wifi Based Indoor Positioning,” in *2014 IEEE World Forum on Internet of Things (WF-IoT) An*, 2014, pp. 111–116.
- [20] M. Ciurana and S. Cugno, “WLAN Indoor Positioning Based On TOA With Two Reference Points,” in *4th Workshop On Positioning, Navigation And Communication 2007 (WPNC’07)*, 2007, pp. 23–28.
- [21] M. K. Hoang and R. Haeb-Umbach, “Parameter Estimation And Classification Of Censored Gaussian Data With Application To Wifi Indoor Positioning,” in *38th International Conference on Acoustics, Speech, and Signal Processing (ICASSP 2013)*, 2013, pp. 3721–3725.
- [22] F. Faheem, “Ibeacon Based Proximity And Indoor Localization System,” Purdue University, 2016.
- [23] A. Madhavapeddy and A. Tse, “A Study of Bluetooth Propagation Using Accurate Indoor Location Mapping,” in *UbiComp 2005: Ubiquitous Computing*, 2005, pp. 105–122.
- [24] F. Zafari, I. Papapanagiotou, and K. Christidis, “Microlocation For Internet Of Things Equipped Smart Buildings,” *IEEE Internet Things J.*, vol. 3, no. 1, pp. 96–112, 2016.
- [25] M. Castillo-Cara, J. Lovón-Melgarejo, G. Bravo-Rocca, L. Orozco-Barbosa, and I. García-Varea, “An Analysis Of Multiple Criteria And Setups For Bluetooth Smartphone-Based Indoor Localization Mechanism,” *J. Sens.*, 2017, doi: 10.1155/2017/1928578.
- [26] P. Baronti, P. Pillai, V. W. C. Chook, S. Chessa, A. Gotta, and Y. F. Hu, “Wireless Sensor Networks : A Survey On The State Of The Art And The 802 . 15 . 4 And Zigbee Standards,” *Comput. Commun.*, vol. 30, no. 7, pp. 1655–1695, 2007, doi: 10.1016/j.comcom.2006.12.020.
- [27] M. Aykac, E. Ergun, and N. B. Aldin, “Zigbee-Based Indoor Localization System

- With The Personal Dynamic Positioning Method And Modified Particle Filter Estimation," *Analog. Integr. Circuits Signal Process*, pp. 263–279, 2017, doi: 10.1007/s10470-017-0969-4.
- [28] R. F. Brena, J. P. García-Vázquez, C. E. Galván-Tejada, D. Muñoz-Rodríguez, C. Vargas-Rosales, and J. Frangmeyer, "Evolution Of Indoor Positioning Technologies : A Survey," *J. Sensors*, vol. 2017, pp. 1–21, 2017.
- [29] L. M. Ni, Y. Liu, Y. C. Lau, and A. P. Patil, "LANDMARC : Indoor Location Sensing Using Active RFID," *Wirel. Networks*, vol. 10, no. 6, pp. 701–710, 2004.
- [30] U.S. Department Of Commerce National Telecommunications And Information Administration, "Manual Of Regulations And Procedures For Federal Radio Frequency Management," no. September. 2017.
- [31] R. Aiello and A. Batra, *Ultra Wideband Systems: Technologies and Applications*, 1st ed. Burlington, MA, USA: Newnes-Elsevier, 2006.
- [32] L. E. Miller, "Why UWB? A Review Of Ultrawideband Technology," Gaithersburg, MD, USA, 2003.
- [33] A. Alarifi *et al.*, "Ultra Wideband Indoor Positioning Technologies : Analysis And Recent Advances," *Sensors (Basel)*, vol. 16, 2016, doi: 10.3390/s16050707.
- [34] T. Komine and M. Nakagawa, "Fundamental Analysis For Visible-Light Communication System Using LED Lights," *IEEE Trans. Consum. Electron.*, vol. 50, no. 1, pp. 100–107, 2004.
- [35] Y.-S. Kuo, P. Pannuto, K.-J. Hsiao, and P. Dutta, "Luxapose: Indoor Positioning With Mobile Phones And Visible Light," in *Proceedings of the 20th annual international conference on Mobile computing and networking*, 2014, pp. 447–458.
- [36] K. Liu, X. Liu, and X. Li, "Guoguo : Enabling Fine-Grained Smartphone Localization Via Acoustic Anchors," *IEEE Trans. Mob. Comput.*, vol. 15, no. 5, pp. 1144–1156, 2016, doi: 10.1109/TMC.2015.2451628.
- [37] W. Huang *et al.*, "Swadloon: Direction Finding And Indoor Localization Using Acoustic Signal By Shaking Smartphones," *IEEE Trans. Mob. Comput.*, vol. 14, no. 10, pp. 2145–2157, 2015, doi: 10.1109/TMC.2014.2377717.
- [38] N. B. Priyantha, "The Cricket Indoor Location System," Massachusetts Institute Of Technology, 2005.
- [39] M. Hazas and A. Hopper, "Broadband Ultrasonic Location Systems For Improved Indoor Positioning," *IEEE Trans. Mob. Comput.*, vol. 5, no. 5, pp. 536–547, 2006, doi: 10.1109/TMC.2006.57.
- [40] D. A. Bohn, "Environmental Effects On The Speed Of Sound," *J. Audio Eng. Soc.*, vol. 36, no. 4, 1988.
- [41] X. N. Fernando, S. Krishnan, H. Sun, and K. Kazemi-Moud, "Adaptive Denoising At Infrared Wireless Receivers," *Infrared Technol. Appl. XXIX*, vol. 5074, pp. 199–207, 2003, doi: 10.1117/12.486354.
- [42] G. Lachapelle, "GNSS Indoor Location Technologies," *J. Glob. Position. Syst.*, vol. 3, no. 1–2, pp. 2–11, 2004, doi: 10.1007/978-1-4614-1377-6.
- [43] B. Peterson, D. Bruckner, and S. Heye, "Measuring GPS Signals Indoors," in *Proceedings of the 10th International Technical Meeting of the Satellite Division*

- of *The Institute of Navigation (ION GPS 1997)*, 1997, pp. 615–624.
- [44] M. Moeglein and N. Krasner, “An Introduction to SnapTrack Server-Aided GPS Technology,” in *Proceedings of the 11th International Technical Meeting of the Satellite Division of The Institute of Navigation (ION GPS 1998)*, 1998, pp. 333–342.
  - [45] L. J. Garin, M. Chansarkar, S. Miocinovic, C. Norman, and D. Hilgenberg, “Wireless Assisted GPS-SiRF Architecture And Field Test Results,” in *Proceedings of the 12th International Technical Meeting of the Satellite Division of The Institute of Navigation (ION GPS 1999)*, 1999, pp. 489–498.
  - [46] N. Samama, “Indoor Positioning with GNSS-Like Local Signal Transmitters,” in *Global Navigation Satellite Systems: Signal, Theory and Applications*, S. Jin, Ed. Rijeka, Croatia: InTech, 2012, pp. 299–338.
  - [47] M. Andrianarison, “New Methods And Architectures For High Sensitivity Hybrid GNSS Receivers In Challenging Environments,” University of Toulouse, 2018.
  - [48] M. Monnerat, R. Couty, N. Vincent, O. Huez, and E. Chatre, “The Assisted GNSS, Technology and Applications,” in *Proceedings of ION GNSS 2004*, 2004.
  - [49] N. Samama, *Global Positioning: Technologies and Performance*. Wiley-Interscience, 2008.
  - [50] S. Nirjon, J. Liu, G. Dejean, B. Priyantha, Y. Jin, and T. Hart, “COIN-GPS : Indoor Localization From Direct GPS Receiving,” in *Proceedings of the 12th annual international conference on Mobile systems, applications, and services.*, 2014.
  - [51] D. KLEIN and B. W. PARKINSON, “The Use Of Pseudo-Satellites For Improving GPS Performance,” *J. Institude Navig.*, vol. 31, no. 4, pp. 303–315, 1984, doi: 10.1002/j.2161-4296.1984.tb00881.x.
  - [52] J. Rapinski, S. Cellmer, and Z. Rzepecka, “Modified GPS/Pseudolite Navigation Message,” *J. Navig.*, vol. 65, pp. 711–716, 2012, doi: 10.1017/S0373463312000124.
  - [53] C. Rizos, G. Roberts, J. Barnes, and N. Gambale, “Experimental Results Of Locata: A High Accuracy Indoor Positioning System,” *2010 Int. Conf. Indoor Position. Indoor Navig. IPIN 2010 - Conf. Proc.*, no. October 2010, doi: 10.1109/IPIN.2010.5647717.
  - [54] C. Bartone and F. Van Graas, “Ranging Airport Pseudolite For Local Area Augmentation,” *IEEE Trans. Aerosp. Electron. Syst.*, vol. 36, no. 1, pp. 278–286, 2000, doi: 10.1109/7.826330.
  - [55] C. Sheng, X. Gan, B. Yu, and J. Zhang, “Precise Point Positioning Algorithm For Pseudolite Combined With GNSS In A Constrained Observation Environment,” *Sensors (Switzerland)*, vol. 20, no. 4, 2020, doi: 10.3390/s20041120.
  - [56] C. Kee, H. Jun, and D. Yun, “Indoor Navigation System Using Asynchronous Pseudolites,” *J. Navig.*, vol. 56, pp. 443–455, 2003, doi: 10.1017/S0373463303002467.
  - [57] X. Gan *et al.*, “A New Array Pseudolites Technology For High Precision Indoor Positioning,” *IEEE Access*, vol. 7, pp. 153269–153277, 2019, doi: 10.1109/ACCESS.2019.2948034.

- [58] A. Fluerasu, N. Jardak, A. Vervisch-picois, and N. Samama, "GNSS Repeater Based Approach for Indoor Positioning : Current Status," in *European Navigational Conference ENC-GNSS 2009*, 2009.
- [59] I. Petrovski *et al.*, "Indoor Code And Carrier Phase Positioning With Pseudolites And Multiple GPS Repeaters," in *Proceedings of the 16th International Technical Meeting of the Satellite Division of The Institute of Navigation (ION GPS/GNSS 2003)*, 2003, pp. 1135–1143.
- [60] A. Vervisch-Picois and N. Samama, "First Experimental Performances Of The Repealite Based Indoor Positioning System," in *Proceedings of the 2012 International Symposium on Wireless Communication Systems*, 2012, pp. 636–640.
- [61] I. Selmi, N. Samama, and A. Vervisch-Picois, "A New Approach For Decimeter Accurate GNSS Indoor Positioning Using Carrier Phase Measurements," in *Proceedings of the 2013 International Conference on Indoor Positioning and Indoor Navigation*, 2013.
- [62] R. Xu, W. Chen, Y. Xu, and S. Ji, "A New Indoor Positioning System Architecture Using Gps Signals," *Sensors (Switzerland)*, vol. 15, pp. 10074–10087, 2015, doi: 10.3390/s150510074.
- [63] C. Ma, J. Yang, J. Chen, and Y. Tang, "Indoor And Outdoor Positioning System Based On Navigation Signal Simulator And Pseudolites," *Adv. Sp. Res.*, 2018, doi: 10.1016/j.asr.2018.07.006.
- [64] D. Lymberopoulos, J. Liu, X. Yang, R. R. Choudhury, V. Handziski, and S. Sen, "A Realistic Evaluation And Comparison Of Indoor Location Technologies," *IPSN 2015 - Proc. 14th Int. Symp. Inf. Process. Sens. Networks (Part CPS Week)*, pp. 178–189, 2015, doi: 10.1145/2737095.2737726.
- [65] M. S. N. Hani Bani, B. A. Bernhardt, and A. Sheynman, "Method And System For Implementing A Dual-Mode Dual-Band GNSS/M-LMS Pseudolites Receiver," EP 2 878 974 A2, 2015.
- [66] C. Yong, Z. Yanping, D.-K. Park, W. Lilong, and F. Zhiqiang, "A Kind Of Indoor Locating System Based On Simulation GNSS Signal," CN 106767831, 2017.
- [67] A. Thiel, H. Mathis, and E. Favey, "Repeater System For Positioning Signals Emitted By Satellites," EP 1 720 032 B1, 2007.
- [68] "U.S. Government Information About The Global Positioning System (GPS) And Related Topics." [Online]. Available: <https://www.gps.gov/>.
- [69] R. R. Bate, D. D. Mueller, and J. E. White, *Fundamentals of Astrodynamics*. New York, 1971.
- [70] E. D. Kaplan and C. Hegarty, *Understanding GPS/GNSS: Principles and Applications*. Artech House, 2017.
- [71] C. Carter, "Principles Of GPS, A Brief Primer On The Operation Of The Global Positioning System." ALLEN OSBORNE ASSOCIATES, 1997.
- [72] A. El-Rabbany, *Introduction To GPS: The Global Positioning System*. Artech House, 2002.
- [73] R. B. Langley, "Dilution Of Precision," *GPS World*, vol. 10, no. 5, pp. 52–59, 1999.

- [74] S. S. van Leeuwen, "GPS Point Position Calculation," *GPS Solut.*, vol. 6, pp. 115–117, 2002, doi: 10.1007/s10291-002-0003-9.
- [75] K. Özsoy and I. Tekin, "Directional GPS Antenna For Indoor Positioning Applications," in *Progress in Electromagnetics Research Symposium (PIERS 2009 Moscow)*, 2009.
- [76] Electronic Communications Committee (ECC) Within The European Conference Of Postal And Telecommunications Administrations (CEPT), "Technical And Operational Provisions Required For The Use Of Gnss Repeaters," Dublin, 2009.
- [77] Electronic Communications Committee (ECC) Within The European Conference Of Postal And Telecommunications Administrations (CEPT), "Regulatory Framework For Global Navigation Satellite System (GNSS) Repeaters," St . Petersburg, 2010.
- [78] The European Telecommunications Standards Institute (ETSI), "Electromagnetic Compatibility And Radio Spectrum Matters (ERM); Short Range Devices; Global Navigation Satellite Systems (GNSS) Repeaters; Harmonized EN Covering The Essential Requirements Of Article 3.2 Of The R&TTE Directive," 2010.
- [79] Siretta Ltd, "Tango 20 GPS Puck Antenna Datasheet."
- [80] A.H. Systems, "SAS-571 Double Ridge Guide Horn Antenna 700 MHz – 18 GHz Datasheet."
- [81] Mini-Circuits, "TB-JEBT-4R2GW+ Evaluation Board And Circuit."
- [82] Analog Devices, "EVAL-ADRF6820 User Guide."
- [83] Analog Devices, "ADRF6820 Datasheet."
- [84] Analog Devices, "ADRF6720-27 Datasheet."
- [85] H. T. FRIIS, "Noise Figures Of Radio Receivers," *Proc. IRE*, vol. 32, no. 7, pp. 419–422, 1944, doi: 10.1109/JRPROC.1944.232049.
- [86] Mini-Circuits, "LHA-13LN+ Datasheet."
- [87] Mini-Circuits, "DAT-31R5A+ Series Datasheet," pp. 1–8.
- [88] Taoglas Limited, "DBP.433.T.A.30 Datasheet."
- [89] Mini-Circuits, "TB-DAT31R5A-SP+ Evaluation Board And Circuit."
- [90] J. S. Dahele and K. F. Lee, "Theory And Experiment On Microstrip Antennas With Airgaps," *IEE Proc. H Microwaves, Antennas Propag.*, vol. 132, no. 7, p. 455, 1985, doi: 10.1049/ip-h-2.1985.0081.
- [91] T. K. Lo, C.-O. Ho, Y. Hwang, E. K. Lam, and B. Lee, "Miniaturized Aperture-Coupled Microstrip Antennas," vol. 33, no. 1, pp. 9–10, 1997, doi: 10.1109/aps.2004.1332111.
- [92] Analog Devices, "Thermal Design Basics Tutorial MT-093." pp. 1–13.
- [93] Abracon LLC, "433 MHz External Antenna AEACAC053010-S433 Datasheet."
- [94] Mini-Circuits, "QBA-07 Power Splitter/Combiner Datasheet," *New York*, pp. 127604–127604.
- [95] Mini-Circuits, "SBTCJ-1W Power Splitter/Combiner Datasheet," *New York*, pp. 127604–127604.
- [96] Analog Devices, "ADRF6720-27-EVALZ User Guide."